The effect of microstructure design on the oxidation and reduction behaviour of iron electrodes

Improving the performance of iron-air batteries

Master Thesis

DELFT UNIVERSITY OF TECHNOLOGY

Faculty of Mechanical, Maritime and Materials Engineering

Department of Materials Science & Engineering

The effect of microstructure design on the oxidation and reduction behaviour of iron electrodes

Improving the performance of iron-air batteries

BY

HARRY JOHANNES KAMP

A Thesis submitted in partial fulfilment of the requirements for the degree of

MASTER OF SCIENCE

in

MATERIALS SCIENCE & ENGINEERING

Delft, the Netherlands
October, 2023

Author:

Harry J. Kamp,
4475372

Thesis committee:

Prof. Dr. Yaiza Gonzalez-Garcia Principal Supervisor	:	Associate Professor of Materials Science & Engineering at TU Delft, 3mE
Dr. Aytaç Yilmaz Daily Supervisor	:	Postdoctoral researcher of Materials Science & Engineering at TU Delft, 3mE
Prof. Dr. Maria J. Santofimia Navarro	:	Full Professor of Materials Science & Engineering at TU Delft, 3mE

Abstract

Pursuing sustainable and efficient energy storage technologies has led to advancements in iron-air batteries. Understanding the intricate relationship between the microstructural features of iron electrodes and their oxidation and reduction behaviour is crucial for optimizing battery performance and lifespan. This thesis aims to investigate the impact of microstructural characteristics, such as phases, grain size, and defect density, on the formation of stable iron oxide/hydroxide compounds and the evolution of hydrogen gas (HER), using cyclic voltammetry (CV) and electrochemical impedance spectroscopy (EIS) experiments in 6M KOH. The influence of an electrolyte additive, sodium stannate trihydrate, and an iron foam functioning as alternative electrode material are also examined.

Hot-rolled, pure iron samples were subjected to annealing heat treatments, resulting in different grain-sized specimens. A dual-phase steel, DP1000 steel composed of ferrite and martensite phases as well as hot-rolled and cold-rolled iron electrodes, completed the materials that formed this study's basis. Initial surface identification via optical microscopy (OM), scanning electron microscopy (SEM), electron backscatter diffraction (EBSD), atomic force microscopy (AFM) and X-ray diffraction (XRD) have been performed.

Results indicate a relatively lower formation of $FeOOH$ for a DP1000 steel anode compared to cold-rolled alpha iron over 12 cycles. A marginally larger decline in HER kinetics is observed for a hot-rolled small grained anode compared to a coarse grained anode, while a clear effect of grain size on the development of Fe_3O_4 and $FeOOH$ could not be established. An iron foam electrode showcases greatly enhanced anodic and cathodic current densities in comparison to solid sheet iron electrodes, due to its cellular structure. The effect of 0.01M sodium stannate added to the electrolyte illustrates a significant reduction in HER intensity for both foam and solid iron samples.

Acknowledgements

This master thesis was written from August 2022 until October 2023. Throughout this period, the guidance and help of multiple people have been of great value. I acknowledge that the current report would not have been achievable without the generous support of these individuals from the Delft University of Technology. Therefore, I would like to express my appreciation and gratitude to these persons.

Special thanks go to Prof. Dr. Yaiza Gonzalez-Garcia for her meaningful commitment and thoughtful approach during the project. The numerous insightful discussions, with useful suggestions and ideas, were invaluable. The constructive feedback on applied methods and obtained results encouraged me to think and analyse concepts deeply during the process.

Furthermore, I wish to express my gratitude to Dr. Aytaç Yilmaz for his friendly and pleasant assistance as the daily (lab) supervisor. Aside from the helpful advice given in many instances, I will keep fond memories of both project-related and personal conversations. Your involvement and interest along the way is much appreciated.

Lastly, I would like to thank Agnieszka Kooijman for her aid in the corrosion lab, Durga Mainali for his support in the sanding, polishing, and microscopy lab and all other persons who helped in any way during the course of this Thesis.

Content

Nomenclature

MAB	Metal-air battery
HER	Hydrogen evolution reaction
W	Specific energy [Wh/kg]
F	Faraday's constant = 96,485 [C/mol]
I	Current [A]
C	Coulomb, 1C = $6.24 \cdot 10^{18}$ electrons
A	Ampere [C/s]
Q	Battery capacity [Ah]
M	Molar mass [g/mol]
U_{cell}	Standard full cell voltage [V]
OCP	Open circuit potential
ORR	Oxygen reduction reaction
OER	Oxygen evolution reaction
η	Efficiency [%]
DoD	Depth of discharge
CIP	Carbonyl iron powder
G	Gibbs free energy [J/mol]
Redox	Reduction-oxidation
EIS	Electrochemical impedance spectroscopy
CV	Cyclic voltammetry
XPS	X-ray photoelectron spectroscopy
ε	Initial porosity
C_{max}	Maximum capacity [Ah/g]
SEM	Scanning electron microscopy
TEM	Transmission electron microscopy
AFM	Atomic force microscopy
XRD	X-ray diffraction
EDS	Energy-dispersive X-ray spectroscopy
IF	Interstitial free
RD	Rolling direction
ND	Normal direction

List of Figures

List of tables

1. Introduction

The scientific community widely recognizes climate change as one of the most pressing crises of the current time. Without swift action, Earth's temperature could rise by up to 2 degrees Celsius by the end of this century, leading to significant weather disruptions. These changes, including rising sea levels, increased droughts, and warmer oceans, would have severe consequences, such as floods, food scarcity, species extinction, and limited access to fresh water. Addressing the root cause, human-generated greenhouse gas emissions, mainly from burning fossil fuels like coal, oil, and natural gas, is essential. Transitioning to renewable energy sources and developing efficient energy storage technologies, such as batteries, are logical approaches to reducing CO_2 pollution. Batteries are currently capable of meeting short-term energy demands for electrical devices and contribute to a more sustainable energy future [1].

Iron-air batteries are seen as a promising, sustainable and reliable energy storage solution. Nonetheless, issues exist for the iron electrode component which need to be resolved in order to be useful for application. Improving the functionality of this specific battery component is the current report's main focus. A firm understanding of oxidation and reduction behaviour (of iron) is of the utmost importance in improving the overall iron-air battery performance. The possible effect of several microstructural characteristics (like grain size, phase fraction and defect density) for this material on the detrimental hydrogen evolution reaction (HER) and formation of an oxide layer occurring during operation of the iron-air battery are studied. The later-mentioned unwanted phenomena can greatly reduce the performance of the battery. Furthermore, the capabilities of a porous pure iron foam is probed to analyse the effect of increased available surface area during electrochemical tests. Lastly, the inclusion of a potentially performance-enhancing electrolyte additive, namely sodium stannate trihydrate, is investigated [1], [2].

The iron-air battery has more difficulties than the ones mentioned previously, for example, problems related to the bifunctional catalysts, self-discharge of the iron electrode and carbonation of the electrolyte. These topics are briefly discussed.

1.1. Motivation

Batteries have been investigated for over a century, and the lithium-ion battery is an ubiquitous item in society. This electrochemical energy storage unit is found in countless portable electronics such as: electric vehicles, cell phones, laptops and so on. The overall performance of these batteries is impressive, they possess a very high specific energy, projected to be around 350-450 Wh/kg on cell level and low self-discharge [3]. Nonetheless, this value range is rather an exception than the rule, as specific energy between 100-265 Wh/kg is commonly achieved in practice. There are, however, several shortcomings to the rechargeable lithium-ion battery which make them less attractive in the long term. The high molar mass and price of lithium host materials make it an unsatisfactory choice to fulfil the industrial needs entirely. Additionally, energy density of materials and recycling considerations play a major role as will be seen next.

Because of this, time and effort are also invested in developing alternative concepts for a battery which can accommodate longer operating times/range for electric cars for example and increase electrochemical storage capabilities for the surplus of renewable energy. A solid option is found in iron-air batteries which belong to the so-called Metal Air Batteries (MABs). Although the iron-air battery has it flaws, it appears to be promising alternative for Li-ion batteries in the near future.

Important battery characteristics are energy density and specific energy (gravimetric energy density) with units Wh/L and Wh/kg, respectively. MABs apply pure metals as material for the anode where the oxygen from the ambient air functions as the cathode reactant, excluding the use of a bulky cathode material inside the cell. So, the iron-air battery has an open cell structure. Consequently, the decrease of the overall battery energy content due to electrode balancing is prevented [5],[6]. The fundamental principles of the iron-air battery will be discussed later in this section. Using calculations based on Faraday's law (eq.1), one can conveniently compare different types of MAB anode materials and Li-ion battery cathode materials concerning specific energy. That is given by the following equation:

$$W = n \cdot F \cdot M^{-1} \cdot U_{cell} \qquad (1)$$

With "W", the specific energy of the material. "n" is the number of electrons transferred. "F" denotes the Faraday constant. The "M" represents the molar mass of the material and "U_{cell}" indicates the standard full-cell voltage. The results of the theoretically calculated volumetric and gravimetric energy per material can be seen in Figure 1.

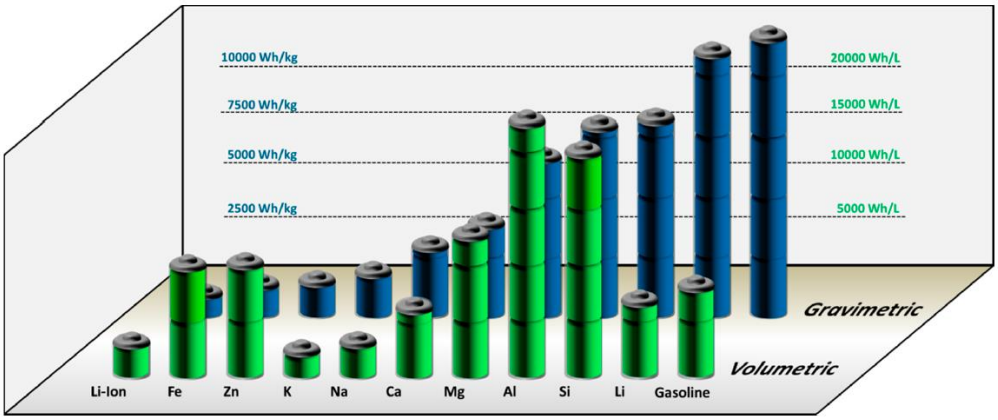

Fig. 1 Gravimetric and volumetric energy densities of several elements applied in Metal-Air Batteries systems compared to the Li-ion battery and gasoline. (excluding oxygen uptake) retrieved from [14]

The blue columns indicate the specific energies of 9 elements that could be applied in MAB systems. The following nine element, Li, Si, Al, Mg, Ca, Na, K, Zn and Fe all exceed the specific energy of present Lithium-ion battery cathode materials. Looking at the energy densities in the green columns, though, shows that the potential energy density of Li is small (6104 Wh/L) in comparison to most of the other elements. Si, Al, Mg, Zn and Fe now exhibit relatively large theoretical energy densities from 9653 Wh/L to 21837 Wh/L, making them very attractive from a battery volume viewpoint [7], [8].

In the context of the climate change problem, sustainability, which comprises the recycling of batteries and abundance of materials, is an essential topic to examine. A recent study has shown that most lithium-ion batteries are not recycled [117]. Less than 5% are recycled due to economic barriers, technical constraints and other factors. The most useful metals in the Li-ion battery components, such as cobalt and nickel, are currently economically worthwhile and feasible to recover. Yet, the batteries are valuable and up to 40% pricier than nickel-cadmium batteries [9]. A large-scale economical recycling path is still absent, while Li-ion batteries are already widely implemented in society. Li-ion batteries that are recycled undergo a very energy-intensive process, which includes high-temperature melting and extraction or smelting (pyro process recycling). Figure 2 shows the traditional methods that could be applied in recycling batteries. Direct recycling, where the battery pack is broken down manually, is likely the most efficient to obtain the valuable metals from the cells. This technique is nonetheless labour-intensive and requires automation because of the comprehensive volumes to process.
For the Iron-Air Battery, on the other hand, the situation is quite different. Iron, one of the most abundant elements on earth, is easily recyclable. With a well-established recycling process readily available, it is significantly cheaper and an environmentally friendly resource [10],[11].

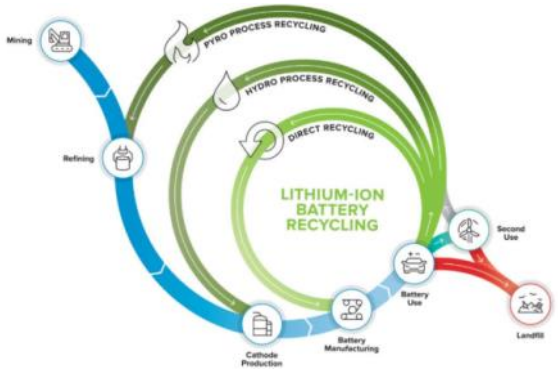

Fig. 2 The recycling routes for materials in batteries each process returns the materials to another step in the manufacturing process. Source: ReCell Center

A related meaningful subject to mention is resource efficiency. It can be described as using the limited resources on earth sustainably while minimizing the environmental impact. For an energy system to be genuinely sustainable, it has to be safe from material shortages and cannot depend on 'aggressive' extraction techniques for the materials of its main components. For iron, this is applicable, but for lithium-ion batteries, it is by no means the case. A good indication for rising technologies to be likely successful can be obtained by examining the resource availability versus the production capabilities in today's industrial facilities [12], [13]. The projected crustal abundance of a few elements is set out against the annual production of the corresponding elements in Figure 3 [14]. When taking a closer look at the plot, one can see that few elements occur at 10^4 ppm or more. Most notably are Si, Al and Fe. At the same time, it is also observable that iron really transcends in yearly production compared to all other elements. With an annual amount of circa 1.3 trillion kilograms, it is solely surpassed by carbon which is a result of the exploitation of fossil fuels. On the other hand, the element lithium is shown multiple orders of magnitudes lower and is accordingly found much lower along the trend line. Meaning that the utilisation of iron for battery systems looks far more auspicious than a lithium based battery [5],[14], [15].

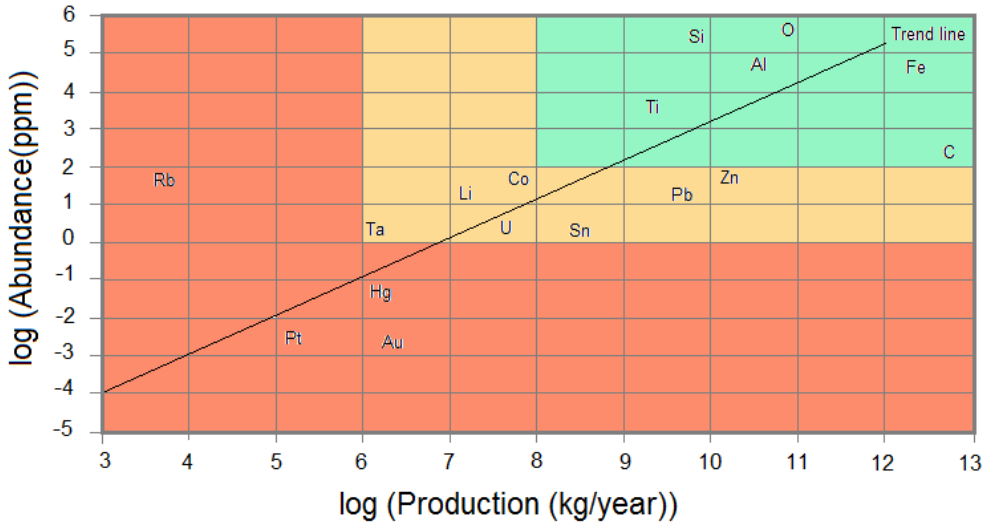

Fig. 3 Estimated abundance (parts per million) vs. annual production (kg/year). The green area indicates favourable elements since they are readily produced extensively and vastly abundant. (redrawn Figure, [4])

1.2. Principles of the iron-air battery

As earlier mentioned, iron-air batteries fall within the metal-air battery category. Metal-air electrochemical cells have in common that a pure metal anode is applied and an external air-breathing cathode (containing a catalyst), is exposed to an aprotic or aqueous solution electrolyte. In this section, the basic principles of the metal-air battery as well as the iron-air battery in particular, will be clarified during the charge and discharge process, including corresponding reactions.

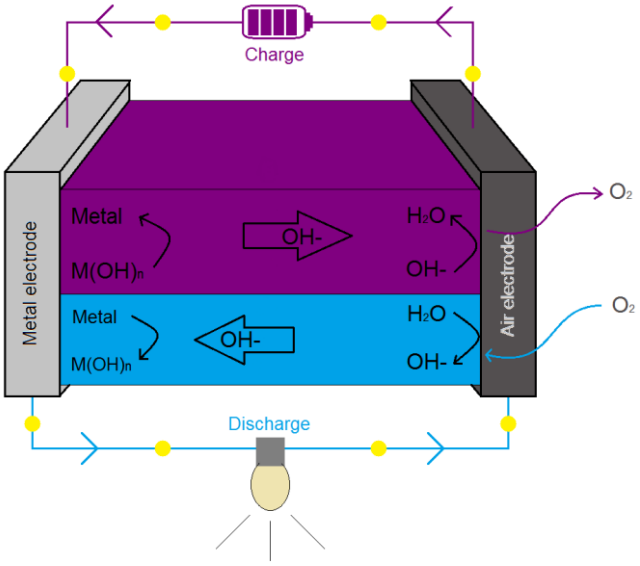

Fig. 4 Illustration of the Metal-Air battery working principle (redrawn Figure [7])

In Figure 4, the working principle of metal-air batteries in aqueous solution is illustrated. As the battery discharges, oxygen from the air is reduced to hydroxides (OH^-) and the hydroxide subsequently oxidizes the metal into primarily metal hydroxides and oxides. In this Figure, the "M" represents the metal (e.g., Al, Fe, or Zn) [20]. This metal releases electrons according to the following formula:

$$M + n \cdot OH^- \rightarrow M(OH)_n + n \cdot e^- \quad (2)$$

Where the valence of the metal ions is denoted by "n". Next, the electrons move through the external circuit toward the cathode, where the Oxygen Reduction Reaction (ORR) initiates [20]. Oxygen molecules from the ambient air are, together with water, reduced to hydroxide ions:

$$\frac{n}{2} H_2O + \frac{n}{4} O_2 + n \cdot e^- \rightarrow n \cdot OH^- \quad (3)$$

The hydroxide ions travel in the direction of the metal electrode, completing the process [20]. The overall cell reaction is obtained combining by the previous two reactions:

$$M + \frac{n}{2} H_2O + \frac{n}{4} O_2 \rightarrow M(OH)_n \quad (4)$$

The iron air battery consists of a (by definition) negative ferrous anode and a positive carbonaceous cathode which allows the import of ambient air. The electrolyte in which the electrodes are immersed is oftentimes strongly alkaline; 6M KOH, for example. This electrolyte ensures good ionic conductivity and is not too corrosive for the iron anode. Iron oxide products have a lower solubility in an alkaline solution than an acidic solution, which helps prevent the formation of unwanted dendrites [5], [21]. During operation, the major reactions of the rechargeable Fe-air battery are the following: Fe is oxidized to $Fe(OH)_2$ and the reduction of O_2 to OH^- occurs when the battery discharges. When recharging, the reactions are reversed [5], [21]. In the image below, Figure 5, a schematic representation of these reactions and relevant species is given.

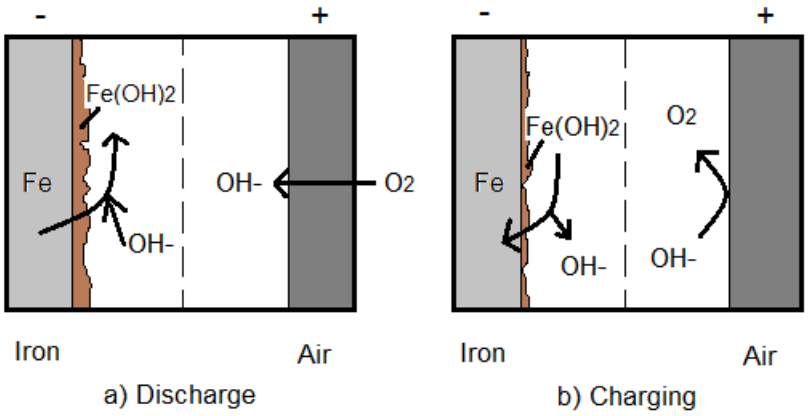

Fig. 5 Processes taking place during Discharging a) and Recharging b) in the Fe-air battery (redrawn Figure [8])

The total overall reaction for the cell is given in equation (5). The reactions appearing at the iron anode and air cathode are shown in equations (6) and (7), respectively. In addition, upon further discharge, $Fe(OH)_2$ can transform to FeOOH and into Fe_3O_4 (eq. (8) and (9)). Note, the arrows pointing towards the right indicate the discharge reactions, the left recharge [22],[23].

$2Fe + O_2 + 2H_2O \rightleftarrows 2Fe(OH)_2$	$U = 1.28\,V$	Overall cell	(5)
$Fe + 2OH^- \rightleftarrows Fe(OH)_2 + 2e^-$	$E^0 = -0.88\,V$ vs. SHE	Iron anode	(6)
$O_2 + 2H_2O + 4e^- \rightleftarrows 4OH^-$	$E^0 = 0.40\,V$ vs. SHE	Air cathode	(7)
$Fe(OH)_2 + OH^- \rightleftarrows FeOOH + H_2O + e^-$	$E^0 = -0.56\,V$ vs. SHE	Deep discharge	(8)
$3Fe(OH)_2 + 2OH^- \rightleftarrows Fe_3O_4 + 4H_2O + 2e^-$	$E^0 = -0.66\,V$ vs. SHE	Deep discharge	(9)

The open circuit cell potential of the Fe-air battery is found to be:
$U = E^0_{cell} = E^0_{cathode} - E^0_{anode} = (0.40) - (-0.88) = 1.28\,V.$

The deep discharge potentials show lower absolute electrode potentials than the initial reaction (6), making them less ideal. As the theoretical cell voltage is now lower, researchers tend to avoid deep discharge reactions as soon as the available iron is completely converted

to $Fe(OH)_2$. The FeOOH and Fe_3O_4 composed of Fe(III) ions are more stable and, are therefore, more prone to undergo incomplete reduction during charging [5], [24],[25].

1.3. Performance of the battery

In order to accurately characterise the performance of batteries, specific parameters are utilized. These defined parameters allow for a reliable comparison among batteries and help identify the appropriate battery application. This section discusses the most important and relevant performance specifications for metal-air batteries.

A fundamental parameter in the field of batteries, is battery capacity. The maximum quantity of energy which can be extracted from the battery under specific circumstances is measured by this attribute and is often expressed in ampere-hours (Ah). Though, the actual amount of current that can be withdrawn from the battery is limited and is known as the power capability. The power capability is measured by using the “C-rate” which indicates the speed at which a battery is fully charged or discharged. A C-rate of 1C is by definition the necessary current to reach full capacity in one hour [104], [105]. The relationship between C-rate and discharge/charge current is given by equation 10:

$$I = C_{rate} \cdot Q \tag{10}$$

Where “I” denotes the current and “Q” the battery capacity.

Relatively large C-rates are typically accompanied with a reduced capacity for the battery, since the necessary substances that react do not have enough time to move and reach each other to react. So, only a fraction of the reactants has been converted into the required products, which means a reduced amount of energy is available.
Another performance indicator is coulombic efficiency, which is the ratio of total charge extracted from the battery to the charge input (i.e. discharge capacity/charge capacity). Losses that are responsible for a reduced coulombic efficiency are primarily due to the rise of secondary reactions like electrolysis of water or other redox reactions, which consume electrons.
A very important parameter for rechargeable batteries is the lifespan (cycle life). These batteries are repeatedly subjected to charge/discharge cycles and are therefore ideally expected to be highly reversible. The most common way to define lifespan is the number of cycles completed until only 80% of the initial capacity remains. The gradual capacity deterioration can be ascribed to unavoidable unwanted reactions in the cell and/or dendrite formation at an electrode. These phenomena can reduce the volume of active chemicals in the battery and impair capacity over time. The aforementioned processes are affected by the depth of discharge (DoD), which can be described as the maximum percentage of the capacity consistently extracted from a charged battery. Generally speaking, a lower DOD results in a larger battery cycle life [103].

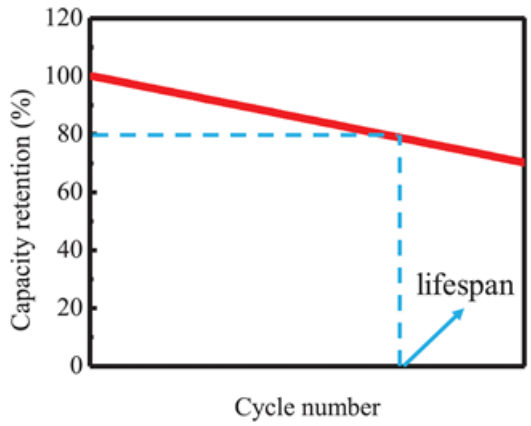

Fig. 6 Capacity retention vs. cycle number

A convenient method to compare MAB systems for specific energy vs. specific power is the so called Ragone plot. The specific energy is earlier discussed; the amount energy per unit mass (Wh/kg) that can be hold by a battery. While the specific power (W/kg) specifies at what rate the energy can be delivered. In Figure 7, Ragone plots containing the potential performances of metal-air batteries compared to li-ion and metal sulphur batteries are illustrated. Weinrich et al. [5] derived these plots in order to obtain a general overview to compare several battery systems. A helpful feature are the isolines which indicate the runtime at a certain point.

The performance values of different types of MABs (magnified on the right) should be interpreted as rough estimations which are based on reports of the individual best results for the MAB cathodes and anodes found in literature. It can be deduced from Figure 7 that MABs excels in terms of specific energy compared to the other battery systems. This is favourable since a considerable amount of energy can be stored per unit mass. On the other hand, the specific power is on the medium to low side, in comparison to metal-sulphur and li-ion batteries, respectively. Among the MABs (right), the Fe-air and Zn-air potentially possess the lowest specific energies, although for these batteries reversibility has already been shown on full-cell level [5].

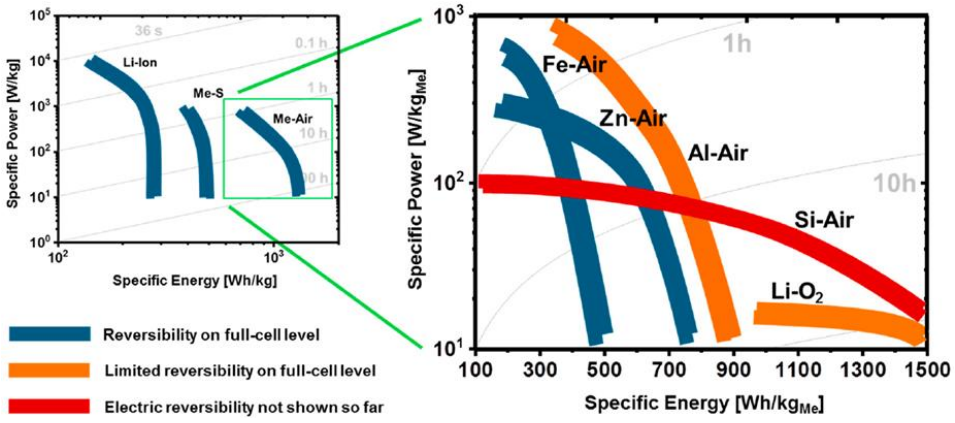

Fig. 7 Performance comparison among battery systems (left) and among MAB systems (right) [5]

Actual experimental results for some tested iron anodes which could be applied in Fe-air batteries are indicated in the table 1 below, to display the performances achieved. Several performance characteristics as well as the applied anode structure is present to provide a general overview. Performance enhancement is sought in the architecture of the iron anode, where present research mainly examines the application micro-and-nanoparticles, as can be seen in the table. In a later section will be further elaborated on (other) anode morphologies and the use of additives to increase the performance.

Iron anode structure	Capacity	Energy density	C-rate	Coulombic efficiency	Reversibility	Reference
Particulate (microscale)	400 mAh/g (Specific discharge)	-	C/5	80%	>180 cycles	[84]
Particulate (nanoscale)	854 mAh/g (Specific discharge)	453 Wh/kg	C/10	88%	>20 cycles	[27]
Particulate (nanoscale)	786 mAh/g (Specific discharge)	-	-	76%	30 cycles	[78]
Particulate (microscale)	300 mAh/g (specific discharge)	-	C/20	96%	>25 cycles	[24]
Particulate (microscale)	230 mAh/g	-	C/5	92%	>1200 cycles	[58]
Particulate (microparticle)	250 mAh/g	-	C/2	95%	750 cycles	[77]

Table 1) Performance characteristics of several iron anodes

In the work of Ito et al. [78], the use of Fe_3O_4 nanoparticles loaded on tubular carbon nanofibers (TCNFs) as active material for an iron anode, for the application in an iron-air battery, is investigated. Electrochemical measurements are performed using a three-electrode glass cell for evaluation of the charge/discharge characteristics. $8\ \mathrm{mol \cdot dm^{-3}}$ KOH electrolyte solutions with and without $0.01\ mol \cdot dm^{-3}$ K_2S additive is utilized. They showed a relatively large specific capacity of 786 mAh/g could be achieved and a cycling efficiency of 76% at the 30th cycle, with the inclusion of K_2S additive. The use of sulphide additives on the effect of cycle life for electrodes composed of carbonyl iron powder is investigated by Manohar et al. [58]. Their experimental setup consists of electrolyte containing 30 wt.% KOH solution and carbonyl iron electrodes with bismuth sulphide, iron (II) sulphide or bismuth oxide powder mixture additives applied in various concentrations. Electrochemical tests are done in a three electrode cell. After an initial formation process, the charging efficiency and discharge rate capability are measured. The results show no fade of capacity for carbonyl iron with bismuth oxide and iron (II) sulphide after 1200 cycles at 100% DoD.

Finally, the study of Mitra et al. [77] also attempts to understand the effect of sulphide additives on the performance of iron electrodes. Carbonyl iron electrodes with zinc sulphide, cuprous sulphide, iron (II) sulphide and iron (II) disulphide are prepared. Electrochemical measurements are carried out in three electrode polypropylene cell in a aqueous 30wt.% KOH solution. The electrode containing zinc sulphide additive demonstrated a coulombic efficiency of 95% for 750 cycles without significant decrease in capacity. These research papers indicate that good performance characteristics like capacity and reversibility are attainable in practice for iron anode electrodes. So their application in iron-air batteries looks well suited to operate in numerous electrical devices in the near future.

1.4. Challenges encountered with the iron anode

The iron-air battery turns out to be an interesting (resource-efficient) system to explore, compared to other MABs, as is discussed in the previous sections. However, adverse events are experienced within the Fe-air battery and predominantly at the iron anode component. This section profoundly examines the challenges encountered at the anode, which include the evolution of hydrogen gas and the formation of a oxide/hydroxide layer. As will be seen, the occurrence of these phenomena can greatly impact the efficiency and re-chargeability of the battery.

1.4.1. Hydrogen evolution reaction

The operation of the electrochemical Fe-air cell has been shown to produce the barely soluble $Fe(OH)_2$ from iron and hydroxide as primary product during discharging, which deposits on the surface of the iron electrode (eq.6). While when charging this reaction occurs in the opposite direction. Now the ferrous hydroxide is reduced back to iron and hydroxides but that is not the only reaction taking place as seen in practice. In fact, the formation of hydrogen gas is observed which is also known as the hydrogen evolution reaction (HER). According to equation 11, hydrogen gas is formed upon recharging at the iron electrode [21]:

$$2H_2O + 2e^- \rightleftarrows H_2 + 2OH^- \qquad E^0 = -0.83\,V \text{ vs. SHE} \qquad (11)$$

The HER can be described as a parasitic side reaction as two unwanted complications arise. Namely, pronounced hydrogen evolution leads to the decomposition of water in the aqueous electrolyte, resulting in a potentially dried out and subsequently dysfunctional battery. Besides that, electrons are diverted into the HER to develop instead of being applied usefully to reduce $Fe(OH)_2$ which is essentially the objective. So the columbic efficiency is drastically decreased correspondingly [5].

The origin for this reaction can be found in the thermodynamics of iron in aqueous media. Since the battery requires an external electric source to drive the redox reaction against spontaneous change ($\Delta G > 0$) when charging, it can be considered to be an electrolytic cell. In this case, the cell potential is higher than the expected theoretical determined potential (1.28 volt) according to the Nernst equation for the battery because of an overpotential required to force the electrons in the opposite direction through the circuit [21],[32].
On the contrary, during discharge of the iron-air battery behaves like a galvanic cell where a redox reaction makes the electrons flow. In this case, the practical working voltage of the iron-air battery is less than 1.28V because of internal losses in the cell due to ohmic, activation and concentration loss [5],[42]. The thermodynamically predicted cell potential is solely obtained under zero current conditions.

In Figure 8, the polarizations curves (current vs. electrode potential) for iron and oxygen are illustrated. For a strong alkaline environment around pH=13.5, the electrode potential of iron is -0.88V and 0.40V for oxygen. Arrows indicate deviation from the open circuit cell potential for increasing (absolute) currents for discharging and charging. The cyan area in the plot depicts the stability region of liquid water. For more negative potentials lying outside this stability region, water is unstable relative to hydrogen gas. This means water gets reduced to hydrogen gas in this situation. More positive potentials (to the right of the stability region of

water) in Figure 8, results in the evolution oxygen gas. Fe-air batteries commonly employ an alkaline solution as electrolyte like 6M KOH which helps to enable the use polarization graphs as well as Pourbaix diagrams to understand the origin of $H_2(g)$ development [32],[33].

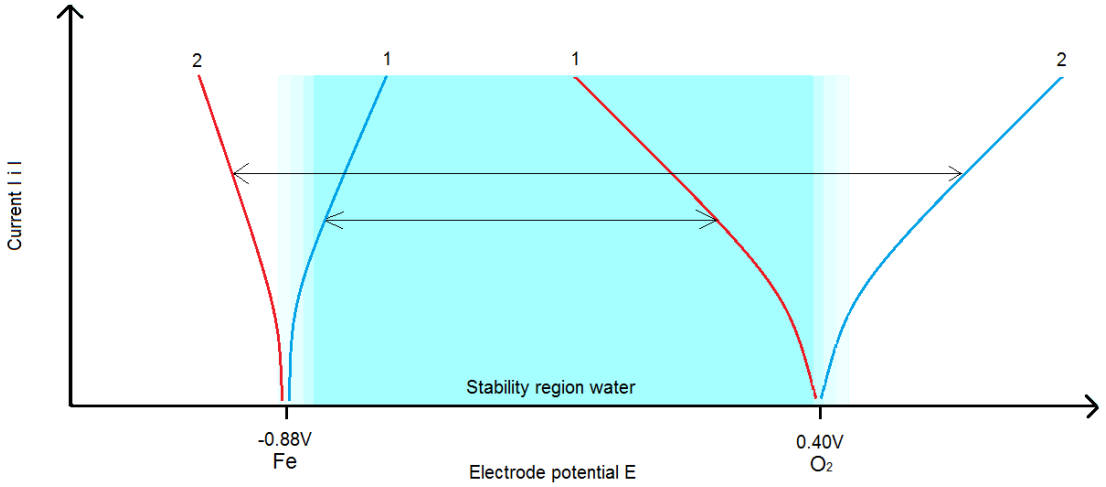

Fig. 8 Polarization curves potential vs. current of iron and oxygen. Cathodic currents are indicated with the red lines. The blue lines are the anodic currents. The discharging process plots belong to "1", recharging to "2".

The region of stability of H_2O can be deduced from the Pourbaix diagram of water. These Pourbaix diagrams are more or less equivalent to phase diagrams and indicates the most thermodynamically stable state for a material for a certain pH and potential. Besides, for metals it can be seen as an equilibrium diagram showing areas where it is protected or subjected to corrosion. Figure 9 shows the Pourbaix diagrams for water, with the "a" and "b" lines, specifying the dominant cathodic reactions concerning water, oxygen gas and hydrogen gas integrated in the iron E vs. pH diagram. The stability region as indicated in Figure 9 is given by the zone between dotted line "a" and "b".

For the polarization curves in Figure 8, a concentrated alkaline aqueous electrolyte ($pH \approx 13$) is considered. From the applying reactions one can now observe the hydrogen evolution reaction (Figure 12). When recharging the problem arises that the cathodic current at the iron electrode leaves the H_2O stability window, allowing the HER to take place. So the relatively large overpotential for charging causes the HER to compete with the reduction of $Fe(OH)_2$ [32], [34], [35]. Frequently, MMO reference electrodes are applied in iron-air battery studies. In strong alkaline solutions, the standard hydrogen electrode which is applied in Figures 8, 9 and 10 can be converted to the Hg/HgO electrode via:

$$E\ vs.Hg/HgO\ [V] = E\ vs.SHE - 0.098V$$

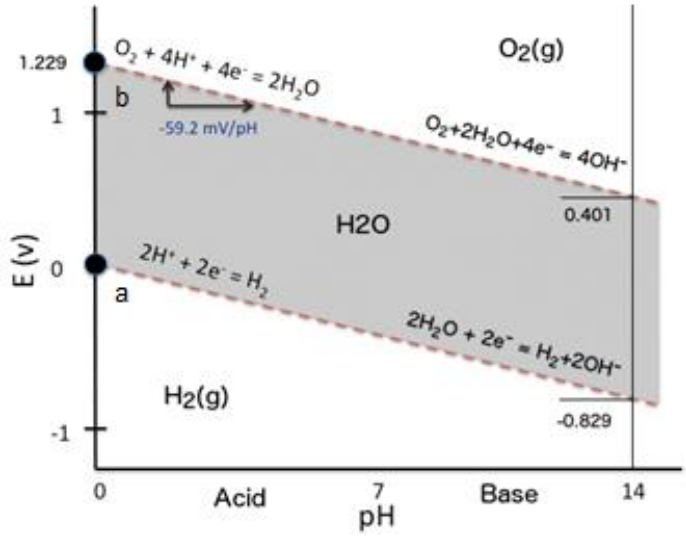

Fig. 9 Pourbaix diagram of water, displaying stability regions and reactions [23]

The Pourbaix diagram of iron is a helpful approach to grasp the thermodynamic principles of the Fe-air battery. Since the electrochemical stable phases of iron are divided in regions as a function of pH and potential. Although for specific information about the rate of reactions, continuation of reaction products and overpotentials, other techniques would be required. Three regimes can be identified regarding the reactivity of the iron species which are immunity, passivity and corrosion. Where pure iron is resistant to any chemical reaction in the immunity regime. In the passivation region, a protective oxide layer of $Fe(OH)_2$ (or other iron oxide/hydroxide compound, dependant on pH and potential) is instantaneous formed due to a reaction with the electrolyte and is deposited on the iron electrode preventing reactions with the bare iron beneath the oxide/hydroxide layer. Lastly, in the corrosive regime, iron corrodes until an eventual protective layer forms which inhibits further oxidation processes [32], [33], [35].

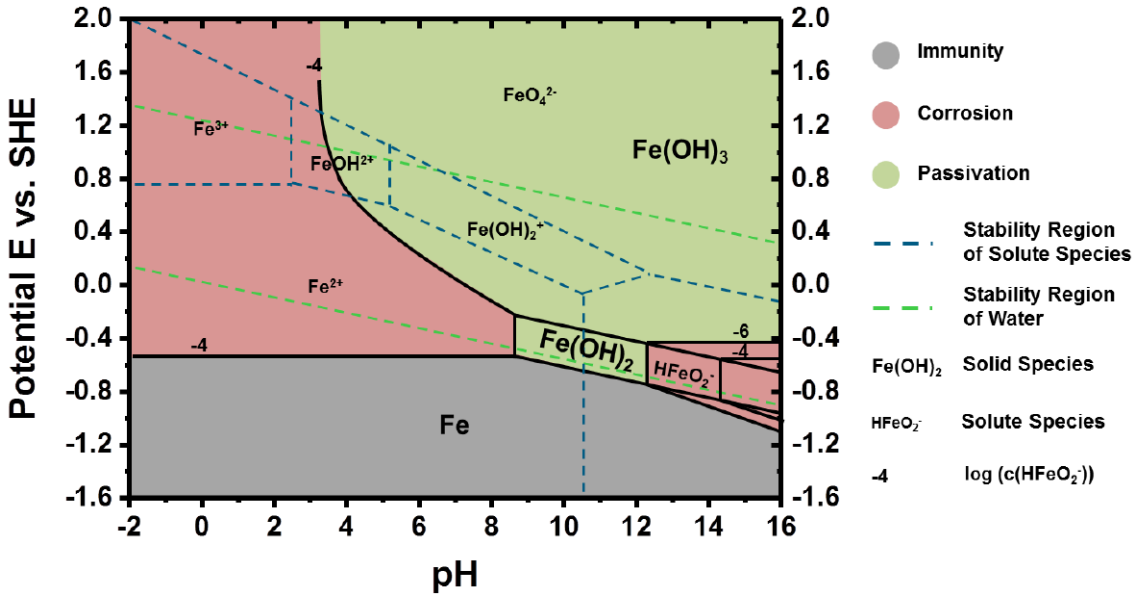

Fig. 10 Pourbaix diagram of iron. Grey area is the immunity region, red regime shows where corrosion takes place and the green region indicates passivation formation. Solid black lines indicates the points where two species exist in equilibrium. Relevant compounds $Fe(OH)_2$ and $Fe(OH)_3$ are given for the passivation regime [10].

When analysing Figure 10, a possible problem can be detected. At highly concentrated alkaline conditions and a concentration of $HFeO_2^- = 10^{-6}\,M$ for an electrode potential higher than -0.8V vs. SHE, iron is unstable. It becomes susceptible to corrosion with a decline in potential limit as the pH of the electrolyte rises. Now the situation emerges where the discharge reaction and the corrosion reaction can occur both yielding in $Fe(OH)_2$; equation 12 and 13:

Discharge: $Fe + 2OH^- \rightarrow Fe(OH)_2 + 2e^-$ $E^0 = -0.88\,V$ vs. SHE (12)

Corrosion: $Fe + 2H_2O \rightarrow Fe(OH)_2 + H_2$ spontaneous (13)

The reactions showcase that the difference is where the electrons are directed to. In the case of the discharge reaction, the electrons are released freely and are navigated through the external circuit for practical usage. While the corrosion reaction converts the electrons for the spontaneous evolution of hydrogen gas, which impairs the efficiency of the battery [32],[35].

1.4.2. Formation of iron oxide/hydroxides

In the previous sections, it has been seen that $Fe(OH)_2$ forms as oxidation product at the anode which is nearly insoluble in the electrolyte. This compound tends to precipitate and thereafter accumulate on the surface of the iron electrode, having a twofold effect. Since homogeneous oxidation behaviour is seen in iron-air batteries, dendrite formation is practically absent. On the other hand, in zinc-air batteries for example, dendrites are ubiquitous as inhomogeneous oxidation occurs upon the charging process. Dendrite growth adversely effects the coulombic efficiency and can cause a short circuit in the system. However, due to the fact that the surface layer get covered by an protective layer, the utilization of the anode material is limited. Because the created oxide/hydroxide film acts as insulation barrier for the involved species, it disallows the discharge reaction to continue, especially due to the irreversible component hematite in the oxide film [32], [36]. An oxide layer is developed on to a metal surface due to reactions with the corrosive species in the environment and the metal. The structure of the iron oxide layer reduces the oxidation rate by obstructing corrosive species to make contact with the metal. The formed protective film restraints oxidation reactions with the metal beneath the oxide layer and thereby reduces electron and/or ion transfer. Porosity, homogeneity as well as the electrochemical properties of the oxide layer influence the corrosion protection. An inhomogeneous and porous film layer structure provides easier access for corrosive species to the metal [106], [107].

The composition of the oxide/hydroxide layer also plays an important role in the corrosion resistance. For pure iron, the insulating layer exhibits n-type semiconductor properties. Consisting of a bi-layered structure with the inner layer being Fe_3O_4 (magnetite) and an outer layer of either α/γ-Fe_2O_3 or similar spinel structure. Despite its higher defect concentration, the Fe_2O_3 compound provides a larger electronic resistance in comparison to Fe_3O_4 [107]. In steels, the oxide layer is primarily composed of α/γ-Fe_2O_3, Fe_3O_4 and α/γ/δ-FeOOH mixture. Also in this case, the hematite is associated with the strongest barrier properties to corrosion [18].
The available surface area of the iron anode plays a key role in the performance improvement of the Fe-air battery. That's why, H.Weinrich et al. [36] did an in-depth research to elucidate the mechanisms involved for the formation of a redox-layer during charge and discharge cycles in their work. This work provides a more detailed description of the processes as well as the topography changes taking place under specified circumstances. The study conducted is comprised of the following: In-situ electrochemical Atomic force microscopy (EC-AFM) research for a plane iron surface applied as anode material to investigate the evolution of the surface in a strongly alkaline medium; 0.5M KOH (pH =13.7). Most notably, they proposed a model which would accurately describe the formation process of the redox-layer upon repeated charge and discharging that is in accordance with the obtained results from the experiments.

First of all, an electrochemically iron oxide layer is naturally ubiquitous present upon the iron anode surface. This happens after the electrode is exposed to a liquid electrolyte or atmospheric environment. Figure 11a. The native iron oxide film is abolished owing to the initial reduction which ensures the bare metallic iron is exhibited to the electrolyte. Aforementioned allows the uncovered iron to pursue electrochemical reactions in the following cycle. The process which puts the removal of the natural oxide layer into operation

appears to be the dissolution of Fe_3O_4 and/or Fe_2O_3 and subsequently the precipitation of $Fe(OH)_2$ particles on to the surface of the electrode. The particles formation seems to occur because of intermediate solute species which are unsoluble and preferential precipitation on specific preferred locations [36].

In the next anodic half cycle (11b), the initial particles and Fe become oxidized. It is considered that the dissolution iron and precipitation of $Fe(OH)_2$, along with the oxidation of ferrous hydroxide (and/or presumably non-stoichiometric particles of hydrated iron(II) oxide) to FeOOH, are the responsible reactions. As a result of the reactions, the following events appear: A thin homogeneous redox layer is developed all over the iron electrode which inhibits further reactions. Secondly, a significant growth of the initial hydrated iron(II) oxide particles. Lastly, extra particles spawn between the initial particles [36]. As a matter of fact, the process of the redox layer formation is mostly reversible by means of a reduction reaction. The depassivation is probably triggered by the dissolution of the redox layer and followed by the precipitation of $Fe(OH)_2$, similarly to the initial reduction reaction. Now, the metallic iron is yet again exposed to the alkaline liquid, granting electrochemical reactions to take place for the next cycle. Also, the superficial particles continuously expand in size. So, upon repeated cycling the particle size as well as the amount of precipitated material increases gradually. Nonetheless a dense layer of particles does not completely cover or forms a firm barrier over the surface of the iron electrode in the first 5 cycles of redox reactions [36].

Therefore, a distinct difference exist between on the one hand the passivation layer (which forms parallel to the oxidation of the initial particles and the oxidation of the bare Fe electrode material) and the particles laying on top of the electrode surface. Namely, the growth of particulate $Fe(OH)_2$ appear on preferential sites add to the total amount of available active material which enhances the capacity of the battery each successive cycle. While the homogenous iron oxide/hydroxide layer forming between the present particles inhibits the discharge capacity significantly of the iron anode and confines this to a specific surface area value [36].

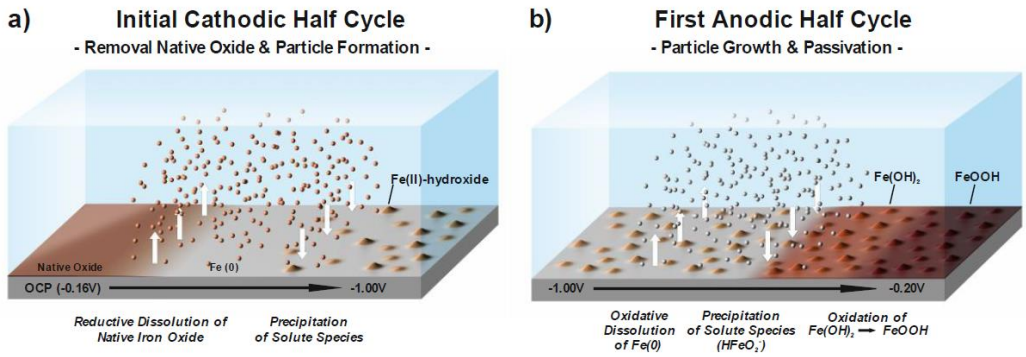

Fig. 11 Hydroxide layer process a) & b) repeated electrochemical cycling of iron showing the redox-layer evolution process in steps (schematically depicted). 11a) exhibits the initial reduction of the native iron oxide layer dissolving into the electrolyte and subsequent precipitation of ferrous hydroxide forming “piles” of particles on the surface. Next, image b) shows iron dissolution with precipitation of $\boldsymbol{HFeO_2^-}$ and consecutive oxidation of $\boldsymbol{Fe(OH)_2}$ towards $\boldsymbol{FeOOH}$ to form a $\boldsymbol{FeOOH}$ redox-layer.

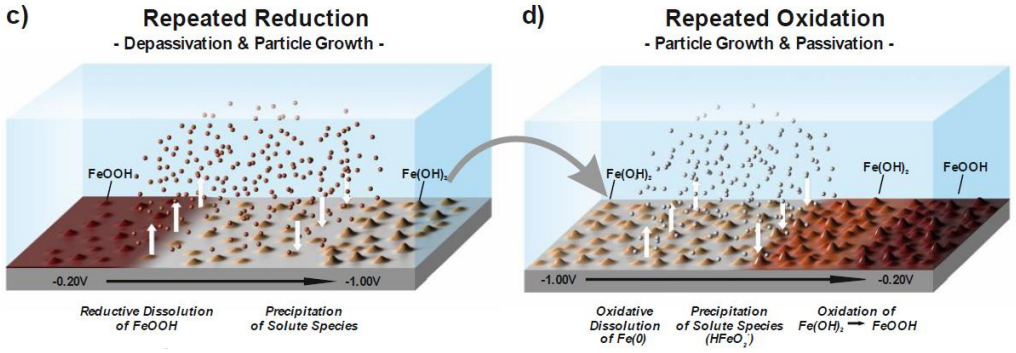

Fig. 11 Redox layer process c) & d), in images c) and d) displays similarly to a) and b) the on-going evolution and change in topography of the surface including continuous growth of the particles, increasing the surface roughness each cycle. A new cycle after situation d) continues again at c).

1.4.3. Secondary difficulties present in the iron-air battery

Other obstacles which are detected in the iron-air battery will be elaborated on in this section. The issues will be discussed with the help of experimental observations and results from literature studies. This section comprises the subjects of self-discharge of the iron anode, bifunctional catalysts and carbonation of the electrolyte.

1.4.3.1. Self-discharge

The self-discharge phenomenon is a process which reduces the performance of batteries during standby. Due to internal reactions, the stored charge is lowered while there is no applied external circuit or any connection between the anode and cathode. There are several self-discharge processes that could take place. First of all, cathodic and anodic reactions can occur simultaneously at the same electrode, where active material is converted due to a mixed potential. Another process is the redox shuttle reaction, in which charge is transferred from one electrode to another. Lastly, ohmic leakage currents facilitate discharging of the battery while no external current is applied [108].
The consequence is a decreased shelf life for the battery and subsequently to possess a reduced charge comparatively to being actually "fully charged" when being in functional operation (i.e. discharge capacity loss). Clearly, it is important for iron-air batteries to limit the issue of self-discharge as far as possible. Several factors are involved for self-discharge including: charge of current, battery type and state of charge. Besides since it is a chemical reaction, the self-discharge rate increases as the temperature rises [37].
In the study by H.W. Weinrich [32], the self-discharge problem is evaluated by means of polarization and OCP-transient measurements for a porous iron electrode. Since the OCP-transient measurements average the oxidation process within the battery over a longer period, it can be considered a more appropriate technique for battery research in this case. Some results of the OCP experiments will be briefly highlighted to illustrate the influence of self-discharge corrosion process on the discharge capacity.

To investigate the oxidation behaviour, a three electrode half-cell setup is used with a Hg/HgO reference electrode and Pt-mesh counter electrode. The anode (working electrode) is composed of 86.5 wt.% carbonyl iron powder, 8.5 wt.% bismuth sulphide and 5 wt.% polyethylene powder. Further conditions applied are a 6M KOH electrolyte solution, a charge time $t_{chr} = 37.5$min, cut-off potential $E_{cut-off} =$ -0.75 V vs. Hg/HgO, discharge current $I_{dis} = 20$ mA, and Q_{chr} = 125mAh/g_{Fe}. After the end of the first OCP-period, a full discharge step is done to determine the decrease in discharge capacity as a result of spontaneous corrosion. The results are shown in Figure 12. Following the formation period, the final five charge/discharge cycles are seen in Figure 12a. It becomes clear that the electrode potential as well as the discharge capacity remain entirely identical during these cycles. When an OCP-period is submitted amidst discharge and charge and vice versa though, the discharge behaviour of the iron anode changes noticeably (Figure 12b). Especially the appliance of an OCP period directly after full recharge allows time for the self-discharge to consume the active Fe material of the electrode, which reduces the discharge capacity gradually [32].

This can explicitly be observed in Figure 12c, where the discharge capacity has decreased from 115.8 mAh/g_{Fe} to 114.3 mAh/g_{Fe} after an OCP time of 60 minutes is inserted after 5

cycles. A stepwise increment of one hour of the OCP period duration causes a steady decline in discharge capacity. So larger a large OCP time in between charge and discharge is detrimental for the battery's available discharge capacity. The induced discontinues rise of OCP periods (in terms of amount of cycles before time increment) employed during the 70 cycles match the staircase-like decrease in discharge capacity accordingly, confirming the self-discharge to occur. At an OCP period time of 8 hours, the discharge capacity has become 93.2 mAh/g_{Fe} compared to 115.8 mAh/g_{Fe} initially. A substantial loss of 22.6 mAh/g_{Fe} (19.5%) has emerged under the aforementioned circumstance [32].

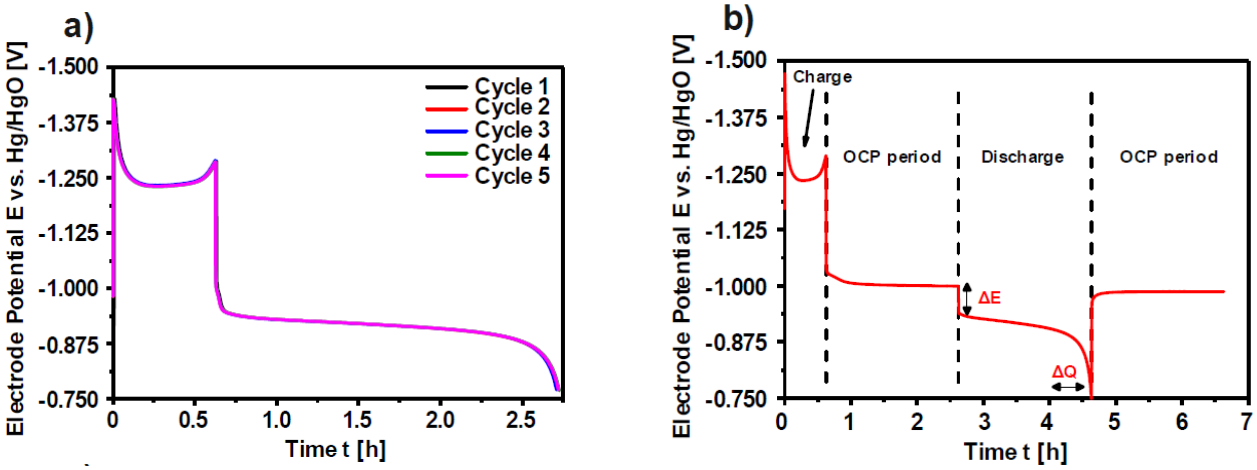

Fig. 12 Formation a) & b), in image a) The last five consecutive charge-/discharge cycles at the end of the formation period showcase a stable behaviour of the curves. Now introducing an OCP-period as seen in (b) shows a drop in potential $\boldsymbol{\Delta E}$, implying a decrease in discharge capacity. Both conducted at ambient temperature.

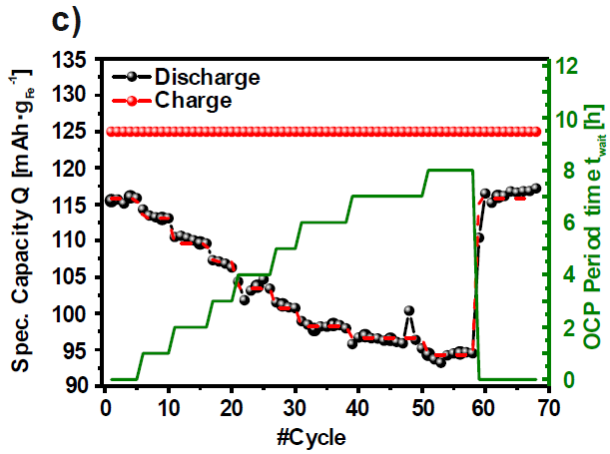

Fig. 12 Formation c), discharge capacity as a function of OCP time between charge and discharge over a total of 70 cycles.

Remarkably, as soon as the OCP period is completely set to zero again, the discharge capacity recovers to its initial value within only 2 charge and discharge cycles. The reason therefore is because the corrosion product of self-discharge is the same as the discharge product of iron and thus also rechargeable [32].

1.4.3.2. Bifunctional catalysts

Focussing now on the cathodic side of secondary iron batteries, the challenge arises to acquire efficient bifunctional air-breathing electrodes. As discussed in the fundamental principles section, the conversion reaction (eq.7) of dissolved oxygen in the electrolyte to OH^- (or H_2O) happens at the air electrode during discharging. While the reverse reaction of OH^- (or H_2O) in the solution into O_2 occurs upon recharging [5],[21].

$$O_2 + 2H_2O + 4e^- \rightleftarrows 4OH^- \qquad E^0 = 0.40\,V \text{ vs. SHE} \qquad (7)$$

So the air electrode has to be able to catalyse the oxygen evolution reaction as well as the oxygen reduction reaction, hence bifunctional. Moreover, a gas diffusion layer has to be integrated to permit oxygen exchange at the electrocatalyst/electrolyte interface. Also, ideally a large electrode surface area is applied to increase the catalytic activity and highly corrosion resistant material for a concentrated alkaline environment. Catalysts that have low overpotentials for both the OER and ORR are uncommon and often consists of expensive precious metals like Pd, Pt and Ru. In reality however, non-precious metals as well as two electrocatalysts as separation for the reduction reaction and evolution reactions, respectively, are mostly utilized by researchers working with bifunctional electrodes. The oxygen reduction turns out to be a sluggish reaction that can progress following a different reaction course in the alkaline electrolyte. The formation of the intermediate species peroxide effectuates the alternative reactions path according to equations [5], [21], [38]:

$$H_2O + O_2 + 2e^- \rightarrow OH^- + HO_2^- \qquad E^0 = -0.076\,V \text{ vs. SHE} \qquad (14)$$

$$H_2O + HO_2^- + 2e^- \rightarrow 3OH^- \qquad E^0 = 0.878\,V \text{ vs. SHE} \qquad (15)$$

For a few reasons the direct oxygen reduction involving four electrons as in equation 7) occurs instead of the steps of 2 electrons per reaction in equations 14) and 15). Namely, the direct reaction takes place at a more positive standard electrode potential and delivers a higher overall cell voltage. Next to this, the intermediate peroxide compound is reactive, enhances the corrosion process and deterioration of the cell components. Metal oxides materials like perovskites, pyrochlores and spinels as well as platinum group metals are usually convenient choices to incorporate for the four-electron reduction reaction (as seen in table 2. For equations 14) and 15) usage of transitional metal oxides, gold and carbon materials is often implemented. Upon recharging the evolution of oxygen which concerns

the release of oxygen atoms onto the metallic surface of the electrode, via the direct four electrons process. The most active catalysts; RuO_2 and IrO_2, are quite costly. That's why many other metal oxides and mixtures are currently under investigation as they show favourable catalytic activity for both the OER and OER. Displayed in table 2 are some of these bifunctional catalysts (which are rarely reported in literature) and a summary with their electrochemical properties [21], [39], [40].

Table 2) Recently developed catalyst and their properties

Properties of recently developed bifunctional air electrodes. E_{ORR}: onset potential of oxygen reduction reaction, E_{OER}: onset potential of oxygen evolution reaction, j_{max} ORR: maximum current density for oxygen reduction at −0.2 V versus Hg/HgO using the catalyst.

Catalyst	Supporting material	E_{ORR} vs. Hg/HgO [V]	E_{OER} vs. Hg/HgO [V]	j_{max} ORR at −0.2 V vs. Hg/HgO [mA cm^{-2}]	Lifetime (number of cycles)
Transition metals/simple oxides:					
Ag	sintered Ni powder	–	–	−80	500
Ag–MnO_2 nanorods	graphite powder, carbon black	0.03	0.61	−0.25	270
MnO_2 + RuO_2	Ketjen black	0.03	0.53	−0.20	50
Ag nanoparticles	glassy carbon	−0.09	0.61	−13	–
Spinels:					
Sr^{2+}- or Ca^{2+}-doped La_2NiO_4	Ketjen black and Super-P carbon	−0.08	0.29	–	20
$LaMnO_3$	carbon black	−0.09	0.60	−10	150
$LaMnO_3$	acetylene black	−0.10	0.40	−51	–
Perovskites:					
$La_{0.6}Sr_{0.4}Co_{0.2}Fe_{0.8}O_3$ (LSCF)	Ketjen black	−0.08	0.29	−200	100
$LaSr_3Fe_3O_{10}$ (LSFO)	glassy carbon	0.28	0.29	–	–
$La_{0.6}Ca_{0.4}CoO_3$ (LCCO)	Vulcan carbon	−0.05	0.50	−100	100
Others:					
MnO_2 + Ni–Fe layered double hydroxide	Vulcan carbon	−0.05	0.5	−10	50
$NiCo_2S_4$	glassy carbon	−0.05	0.38	–	–
$Pb_2Ru_2O_{6.5}$ (pyrochlore)	commercial carbon GDL	0.1	0.4	−20	6

Reproduced from [21]. Literature references of the catalysts from the top down: [44]-[56]

1.4.3.3. Carbonation

Another related problem with the air-breathing cathode, is the undesired influx of gasses other than oxygen. In particular carbon dioxide is addressed to be detrimental for the battery's performance. As the reaction between carbon dioxide and hydroxide could form carbonate precipitates in the solution which clog the electrodes pores and consequently the electrolyte channels. This is called carbonation of the electrolyte and occurs in many metal-air batteries during discharge in alkaline media via the following reaction [42]:

$$CO_2 + 2OH^- \rightarrow CO_3^{2-} + H_2O \qquad (16)$$

In addition, hydroxyl ions are converted into water and carbonate species which lowers the OH^- concentration in the electrolyte, thereby decreasing the cell capacity. Possible solutions to the CO_2 sensitivity problem are to apply a membrane exclusively permeable to oxygen or supply purified air into the cathode. Furthermore, letting the electrolyte circulate through the cell appears to be advantageous since carbonate saturation develops later in the solution compared to keeping the electrolyte stationary. Nowadays these promising concepts are studied thoroughly but further improvements are still demanded [42],[43].

1.5. Effect of microstructure on the performance and efficiency of anodes

The iron anode in the iron-air battery could potentially benefit from an advantageous microstructure in order to enhance the overall performance. More specifically, hydrogen evolution and oxide formation are controlled and suppressed to realize a higher coulumbic efficiency, larger battery capacity and longer lifespan. The limited amount of battery studies published where the effect of a certain (single) microstructural feature is investigated for an iron anode in combination with comparable conditions/setup (strong alkaline pH, low carbon steel/pure iron etc.) makes it difficult to establish the exact effect of microstructural characteristics. Therefore, knowledge currently available in the field corrosion and passivation of iron are used.

Firstly, grain refinement looks promising in order increase corrosion processes by weakening the barrier properties of the passivation layer [96]. Next, a relative large dislocation density in low-alloyed steel is linked to higher corrosion rates [116]. Moreover, a pearlitic phase in steel could be favourable because of inferior passive film properties [112]. Next to this, a steel consisting of a single phase (ferrite or pearlite) seems more advantageous in comparison to dual phase steels as this gives rise to large anodic and cathodic areas. The anodic regions allow for dissolution of the material and could results in a (more) non-uniform corrosion distribution compared to a single phase steel. Finally, the chemical composition is ideally nearly pure iron (active material) while the addition of elements such as Ca, Mn and Mg is prevent as these could form unwanted sulphide inclusions [111]. Experiments could be performed in order to verify these presumptions and to better understand the effect of microstructure under similar circumstances for the iron-air battery.

1.5.1. Grain size

A relevant research regarding composition of the iron passive layer is conducted by Yilmaz et al. [96]. Their goal was to elucidate the role of grain size on the passive layer properties of pure iron (>99% Fe) in aerated 0.1M NaOH solution.

Their experimental results using electrochemical impedance and potentiostatic polarisation tests imply a degradation of the barrier properties of the passive layer for grain refinement. At grain boundaries typically the accommodation of large amounts of lattice defects occurs. It is hypothesized that these lattice defects also induces more formation of defects at the passivation layer's grain boundaries. Thus, higher grain boundary area (grain refinement) causes a more defective passive layer.

Moreover, The lowest fraction of γ-Fe_2O_3, which accounts for the most barrier properties of the passive layer (in comparison to FeO(OH) and Fe_3O_4), is seen in sample S (Figure 13). So, the deterioration of the passive film is enhanced with grain refinement. The effect of donor density is the following: the higher the donor density in the passive layer, the higher the deterioration of the passive layer. Defects in the passive layer are related to the conductivity due to changes in ionic and electronic resistance. Because of defects, a larger conductivity in the passive film is generated which is caused by a decreased ionic and electronic resistance [96].

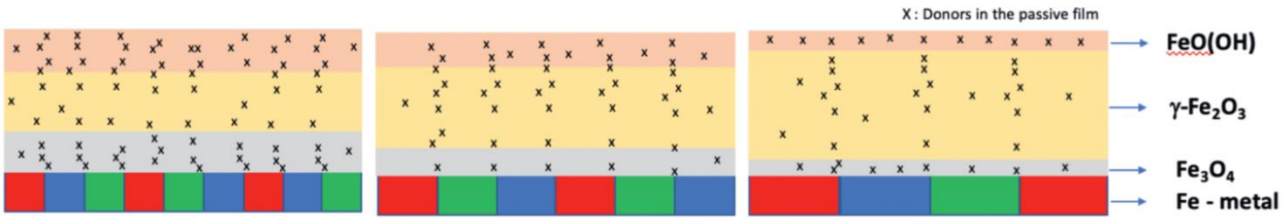

Fig. 13 Schematic illustration of passive films for relatively small, medium and large grained samples, with according structure changes [96].

1.5.2. Defect density

Extensive research on the effect of plastic deformation on corrosion behaviour is performed. It is generally known that dislocation density increases if a metal (alloy) experiences plastic strain. However, there is not an unified consensus of the influence of dislocation density on the corrosion rate of materials. Therefore an attempt is made is understand the effect of dislocation density for a low alloy steel, in the paper of Samusawa et al. [116]. Immersion tests in an acidic solution (pH≈3.1) were carried out with three steel samples being pre-strained at 0%, 4% and 8%. Electrochemical characteristics were analysed including the amount of weight loss as a result of corrosion. The applied steel is identified to possess a ferrite-pearlite microstructure.

The results show that a positive correlation was found between the dislocation density and corrosion weight loss, as seen in Figure 14. The sample exposed to 8% pre-strain has a 25% higher corrosion rate compared to sample without pre-strain. Polarization curves display a larger anodic current for the 8% strained specimen compared to the 0% pre-strained sample near the corrosion potential. Thus promotion of the anodic dissolution reaction is seen. This phenomenon is probably best explained by the terrace-ledge-kink model (Figure 15). Since more lattice defects are introduced at the steel surface, iron atoms at these defect sites have now a small number of nearest neighbour atoms. This is an unstable state and causes higher solubility of iron atoms [116].

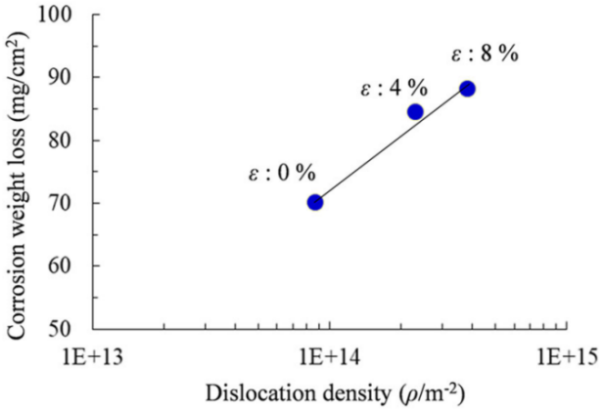

Fig. 14 Recorded corrosion weight loss as a function of dislocation density in the material [116].

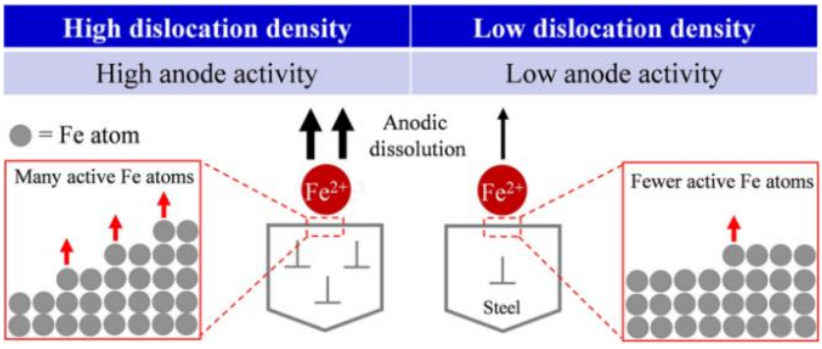

Fig. 15 Proposed mechanism for enhanced anodic dissolution for metal with a high dislocation density [116].

1.5.3. Texture

In a study conducted by He et al. [113], interstitial free (IF) steel samples in 3.5 wt.% NaCl solution with various textures and grain sizes were produced by cold-rolling and, subsequently an annealing process. Their investigation aimed to clarify the influence of crystallographic orientation, grain size and stored energy on the corrosion resistance of IF steel.

Upon analysis, it is found that the microstructure of the as-rolled sample displays a structure of bands with a thickness of a few micrometers, elongated along the rolling direction (RD). The developed texture components formed are the γ-fiber (⟨111⟩//ND), α-fiber (⟨110⟩//RD) and the {100} ⟨110⟩ component. Expanding the annealing times further revealed that the microstructure continued to coarsen, where grain size increased as well as the volume fraction of recrystallized grains. Examination of the crystallographic orientations of the samples indicated that recrystallized grains increasingly exhibit the γ-fiber component. Meanwhile, the volume fraction of α-fiber component gradually decreased for longer annealing times [113].

Based on their experimental results, the authors argued that corrosion tendency and corrosion rates decline for increasing annealing time in cold-rolled, IF steel. The texture component γ-fiber is observed to increase for long annealing times while α-fiber intensity decreases. The stored energy gradually reduces for relatively long annealing times due to the reduction in dislocation density.

Other studies indicate that crystallographic orientation has an effect on corrosion behaviour of pure metals, including iron. Fushimi et. al [107]. found for pure iron in sulphuric acid solution (pH=1) a decrease in corrosion activity for the crystallographic planes {100}, {111} and {101} in that order. This result was attributed to the behaviour of d-orbital electrons. On the other hand, the results of Schreiber et. al [120]. showed the largest preferential dissolution of iron was seen for the {111} orientation (laterally most dense packed plane). An easier formation of an oxide layer was observed for samples possessing the {100} plane. These experimental results, which were conducted in acetate buffer solution (pH 6.0), are explained by the larger distance between atomic layers leading to a weaker binding of atoms.

1.5.4. Phases

The effect of phase fractions present in a steel can significantly influence the corrosion behaviour of steel. However, literature papers on the corrosion behaviour of steels do not provide a unanimous consensus or comprehensive understanding regarding the specific impact of phase constituents on corrosion behaviour in all cases.

For example, the passivity of a carbon steel (S45C) composed of pearlite and primary ferrite is investigated in pH 8.4 boric acid-borate buffer by Fushimi et al. [112]. Micro-electrochemical measurements are carried out using a micro-capillary cell in order to clarify the effect of phases on the passive oxide film. It is found that the oxide film of pearlite is both thicker and inferior to that of the pure ferrite passive layer. The ionic/electronic conductivity of the pearlite oxide layer is larger. A higher conductivity is seen because of carbon in the oxide film, through the presence of cementite, and the resulting finer grain microstructure. The development of $FeCO_3$ in the oxide, due to the cementite substrate underneath, reduces charge transfer resistance.

Moreover, the uneven distribution of alloying elements like manganese in the pearlite substrate is probably the main cause of the pearlite-ferrite boundary's high activity. The structure becomes more active overall due to mismatches and extra energy states at the grain boundaries. Because of this, the passive layer structure of the pearlite phase is worse than that of pure ferrite [112].

However, some similar studies contradict the effect of phases on corrosion in low-carbon steels. For example, a study by Yilmaz et al. [96] found that a dual-phase ferrite-martensite microstructure shows lower barrier properties of the passive film in 0.1M NaOH solution during potentiostatic polarisation and EIS experiments compared to a ferrite-pearlite microstructure. This is attributed to a higher donor density in the passive layer of ferrite-martensite specimens. On the other hand, electrochemical tests (in 3.5 wt.% NaCl) of Bhagavathi et al. [119] indicate increased corrosion rates for a ferrite-pearlite structure in comparison to dual-phase martensite and ferrite. The galvanic couple between pearlite and ferrite is mentioned to be stronger than the martensite and ferrite couple. Since martensite is structurally, and compositionally homogeneous, and closer to the matrix ferrite phase.

The coupled galvanic corrosion of a steel composed of a certain ferrite and martensite phase volume fraction is extensively reported in literature [32], [121]-[123]. The corrosion behaviour is illustrated in Figure 16 below, which shows the polarization curves of a high purity dual phase steel consisting of varying proportion of ferrite and martensite. The following behaviour is generally observed; these two phases form a galvanic couple in steel where the martensite acts as a cathode and ferrite as the anode. This is due to the difference in potential between the phases. In this case the martensite is protected. However, when a single phase is present, the martensite showcases a higher corrosion rate compared to a completely ferrite based material.

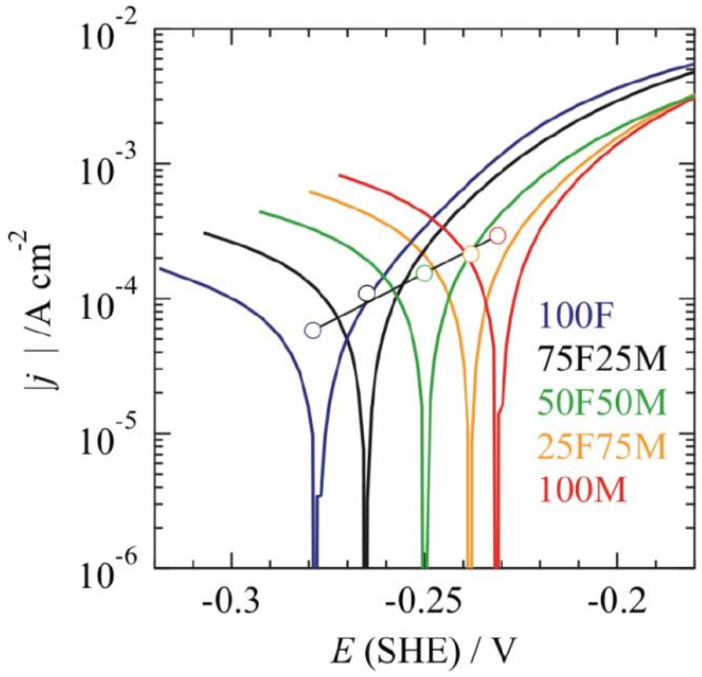

Fig. 16 Polarization curves for ferrite-martensite dual phase steel with several fractions in 0.1M sulphuric acid. Tafel extrapolation has been applied to determine corrosion current and potential (white circles) [121].

1.6. Additives for the iron-air battery

Another tool to enhance the performance characteristics is achieved by means of applying additives. Specifically the rechargeable anode which relies mostly on impeding the intensity of the HER and the reversibility of the oxide/hydroxide species during charging are of considerable importance. Many additives have been investigated in order to improve cycle capacity and several proved to be suitable in doing so. According to experimental observations and data in various literature studies [5],[108], sulphide additives are associated to affect the behaviour of alkaline iron anodes in multiple ways. For example, these additives could increase the bulk electrical conductivity of the electrodes and raise the overpotential for the hydrogen evolution (reaction 11). For those reasons, sulphide additives are extensively examined, as will be seen in a moment.

A division can be made depending on the individual chemical composition and location of application of the additive, namely: electrode and electrolyte additives. At the end, an overview (table 3) is provided to summarize the performance of several recent research experiments conducted and a recommendation for potentially promising results for the future will be suggested.

1.6.1. Additives applied for the iron anode

A large amount of additives have been identified over the past years, that improved the performance of the iron anode and in particular sulphides compounds receive a lot of attention. PbS, FeS and Bi_2S_3 have been employed for porous iron electrode additives in alkaline solution by Shukla et al. [57] to elucidate the effects on the charge/discharge reactions. The outcome of their experiments demonstrate a suppression of the HER for the sulphide additives applied. This is accomplished by affecting the kinetics of the HER at recharging while simultaneously impede the passivation of the anode during discharge. Especially bismuth sulphide looks like an encouraging additive to enhance the battery performance hitherto.
Although, the precise mechanism for the suppression of the HER by the Bi_2S_3 additive is not yet fully understood, it is presumed that bismuth sulphide is reduced to bismuth (eq.17) when the battery charges. The elemental bismuth raises the HER overpotential because of the inferior energetics which is present for the electrosorption of the surface bonded hydrogen intermediates. On top of that, the iron sulphide which is formed according to equation 18) hinders the passivation layer formation, resulting in better rate capability.

$$Bi_2S_3 + 6e^- \rightleftarrows 2Bi + 3S^{2-} \quad (17)$$

$$S^{2-} + Fe(OH)_2 \rightleftarrows FeS + 2OH^- \quad (18)$$

1.6.2. Additives applied in the electrolyte

Another species for effectively reducing the HER are organosulfur compounds. These electrolyte additives are regarded efficient, environment friendly and cheap for the iron anode. Self-assembled monolayers made up of alkanethiols onto the iron electrode can restrain the HER effectively, as demonstrated by Narayanan et al. [60]. A clear effect of the chain length of the alkanethiol on the impeding effect, where the addition of alkanethiol with a carbon number $n \geq 6$ leads to reduction of over 90% for the HER rate. Also is found that various structures of the organosulfur compound were able to form a firmly absorbed layer on the iron electrode, illustrated in Figure 17. The HER rate is now dependant on the coverage surface and the organosulfur compound structure. Coatings of 1,2-ethanedithiol and 3,6-dioxa-1,8-ocatanedithiol deposited on carbonyl iron anode showed both a charging efficiency of 90-92% at a charge rate of C/2 and discharge rate of C/20.

The organosulfur species also played a role in the depassivation process at the iron anode. Cyclic voltammetry (CV) curves did demonstrate a new peak at -0.75 V when the organosulfur coating is applied and an increased reaction current. The formed conductive iron sulphide is responsible for this new peak, according to equation (19). Thus rate capability is improved using organosulfur compounds for the iron anode [60],[61].

$$RS^- + OH^- + Fe \rightleftarrows FeS + ROH + 2e^- \quad (19)$$

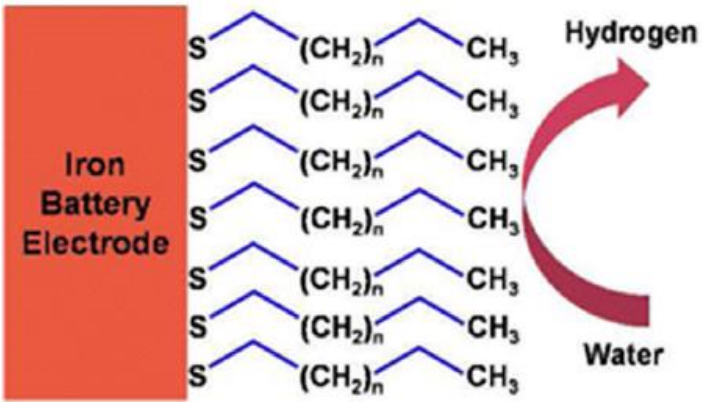

Fig. 17 Modification of the carbonyl iron anode surface with incorporation of organosulfur compounds [60].

1.6.3. Overview additives reported in literature

In table 3, the application of additives of many papers of the last years are given including the conditions present and important performance results obtained.

Active material	Additive (Electrode)	Electrolyte (KOH + electrolyte additive)	Discharge rate	Stable capacity (mAh/g)	Final capacity (mAh/g)	Charge efficiency	Reversibility	Ref.
Nano Fe/Fe_3C/Cu	5% Bi_2S_3	6 M KOH	100 mA/g	350	345	80%	100 cycles	[70]
Sintered Carbonyl Fe	FeS	30 w/v% KOH	1C	190	≈180	97%	3500 cycles	[31]
Iron powder	10.3% FeS+7.5% Bi_2S_3	5.1 M KOH+0.1 M LiOH+0.1 M K_2S	C/5	290	≈290	58%	40 cycles	[71]
Iron powder	80% FeS	5.1 M KOH+0.44 M K_2S+0.3 M LiOH	C/5	220	≈220	96%	50 cycles	[72]
Carbonyl Fe	10% Bi_2O_3+5% FeS	30 w/v% KOH	C/2 charge C/5 discharge	230	≈230	92%	1200 cycles	[58]
Iron powder	4% Bi_2S_3	28.5 w/v% KOH	-	325	320	44.5%	40 cycles	[59]
Iron powder	4% Bi_2S_3	5 M KOH+0.44 M K_2S+0.3M LiOH	C/5	350	≈350	64%	50 cycles	[67]
Carbonyl Fe	-	1 M KOH +3,6-dioxa-1,8-octanedithiol	C/2 charge C/20 discharge	230	≈230	90-92%	12 cycles	[73]
Carbonyl Fe	-	1 M KOH+1,2-ethanedithiol	C/2 charge C/20 discharge	280	≈280	90-92%	12 cycles	[73]
Carbon-grafted Fe/Fe_3O	1 wt% Bi_2S_3	6 M KOH+1 w/v% LiOH	100 mA/g	400	356	80%	100 cycles	[74]
Carbonyl Fe	10% Bi_2O_3+5% FeS	30 w/v% KOH	3C	200	-	92%	-	[75]
Carbonyl Fe	5% Bi_2S_3	30 w/v% KOH	C/2 charge C/20 discharge	300	-	96 ± 1%	25 cycles	[24]
Iron-carbon paste Fe_2O_3/MWCNT	5% Bi_2S_3	6 M KOH	-	350	-	82%	-	[76]
carbonyl iron	5% zinc sulphide	30 w/v% KOH	C/2	250	240	95%	750 cycles	[77]

Table 3) Specifications of several experiments including the effect of additives

1.7. Electrode concepts for the iron anode

In the search for alleviating measurements to enhance the iron battery's performance, another branch that is studied is the morphology of the iron electrode. Altering the structure of the anode has been observed to bring benefits on several fronts compared to the 'usual' electrode plate (sheet) concept. Although not one single concept is perfect in every aspect, it will be seen that certain structures might help significantly in overcoming troublesome phenomena. In the coming section, five electrode designs with their capabilities, pros and cons are reviewed and compared. The probed iron anode concepts include: the plane sheet electrode, pressed plate microparticles electrode, sintered electrode, nanoparticle structured electrode and finally the iron foam electrode. Next to the structure itself, attention is paid to the possibilities in terms of the processing procedure and the composition. At the end, an overview (table 4) is provided to summarize the performance of several recent concepts applied in experiments.

1.7.1. Plane sheet electrode

Perhaps the most applied and standard concept is the sheet concept for the electrode. Since it has a very robust and simple shape to manufacture, it's convenient for fundamental research purposes. However in practice, the applicability of such a sheet electrode is not suitable as the surface area exposed to the electrolyte is relatively limited compared to other morphologies. The electrochemistry of the iron anode is confined to surface reactions, where a large surface area of the electrode allows for more species to react in a given timeframe (due to faster diffusion of molecules across a concentration gradient), resulting in a higher current flow.

1.7.2. Microparticles

One of the first reports of the application of microparticles for iron anodes was done by Manohar et al. [24] and later by various other researchers. In an attempt to reduce the HER and obtain a high discharge rate capability for the iron-air battery, led them to fabricate a pressed plate microparticle electrode. In their work, an iron electrode is provided with carbonyl iron powder which are spherical iron particles with a 3-5 µm diameter, as seen in

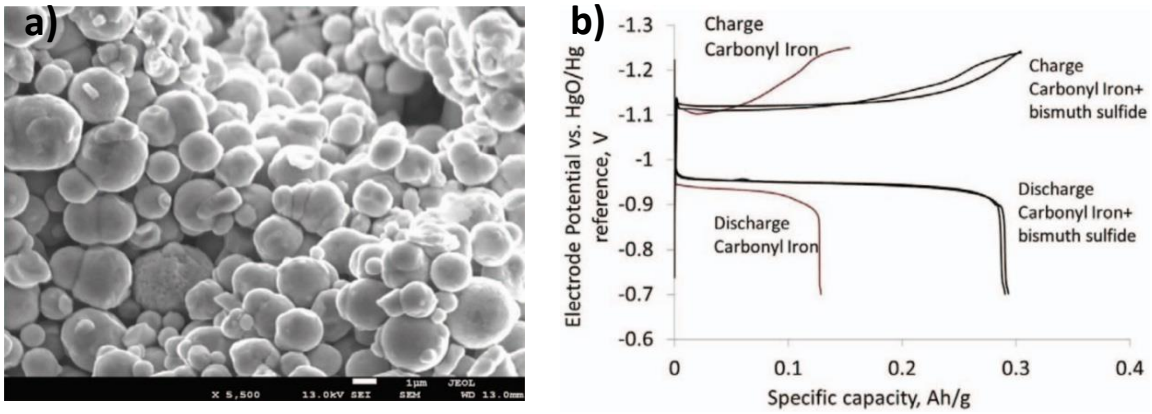

Fig. 18 Image of the morphology of the carbonyl microparticles on the electrode (a). Charge and discharge profiles for the carbonyl iron without and with bismuth sulphide additive. Bismuth sulphide further enhances the specific capacity (b) [24].

Figure 18. The carbonyl powder, consisting of high purity α-iron effectuates the inhibition of the HER and a high discharge rate. The pressed plate electrode are produced using the combination of iron as well as polyethylene binder material followed by a heat treatment. It is described as low cost manufacturing procedure which is an important aspect to consider for potential large scale production for energy storage purposes. A tenfold reduction in relative hydrogen evolution rate is claimed for a carbonyl iron electrode with bismuth sulphide additive, compared to commercial electrodes, which is composed of magnetite ore and graphite. Consequently, a staggering 96% versus 60% charging efficiency was observed, respectively. This is attributed to the high overpotential for the HER of the carbonyl iron combined with bismuth sulphide. A relatively good discharge capacity of 300 mAh/g is reported as well [5], [24].

1.7.3. Sintered electrode

In the extent of the iron electrodes composed of microparticles are the sintered electrodes. These concepts resemble each other except for the extra sintering heat treatment applied afterwards. This process fuses small particles using heat or pressure to form new solid shape. The difference on microscale can be seen in Figure 19a. By doing so, the porosity of the material will decrease but in return the strength and electrical conductivity (among other things) will be enhanced. Research done Yang et al. [31] studied the effect on the performance for CIP electrodes prepared by sintering. More specifically, the relationship between pore size and porosity on the utilization of the iron active material is elucidated. The heat treatment for the samples consisted of applying a temperature of 850°C for the duration of 15 minutes with the provision of argon gas. However, the incorporation of the HER suppressing additive bismuth sulphide was not feasible for the iron electrode, since the temperature of the sintering process exceeded the melting points of bismuth sulphide and bismuth oxide. Despite the absence of bismuth sulphide, a charging efficiency of 96% was still achieved [5],[31].

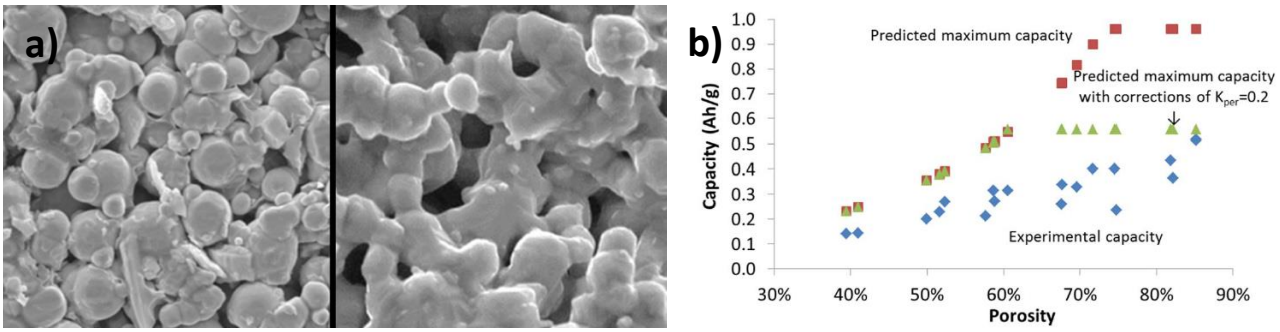

Fig. 19 a) Comparison of microparticles to a sintered electrode. Sintered particles now form an enhanced connected structure. b) Various discharge capacities found for varying porosity percentages. Red points and green points indicate values calculated with the proposed model and adjusted model, respectively [31].

To predict the effect of the initial porosity quantity on discharge capacity, a model is applied besides the results from the experiments as can be seen in Figure 19b. This model assumes the maximum specific capacity can be obtained when the pore volume is filled with discharge product and accessible for the discharge reaction to take place [31]. The maximum capacity is given by:

$$C_{max} = \frac{\varepsilon}{1-\varepsilon} \cdot K \qquad (20)$$

with K being a constant based on material properties of the iron anode. The initial porosity is indicated by ε. Theoretically, the maximum capacity is $C_{max} = 0.962\ Ah/g$ and can be achieved at an initial porosity of 73%.

However a correction value for K, K_{per}(=0.2) in the model is implemented to ensure all iron particles are electronically interconnected, as rechargeability of the species would be compromised (i.e. percolation threshold should be met). As a consequence, an initial porosity value of 61% is obtained. The discharge capacity increases with porosity but there exists a discrepancy between the (adjusted) model(s) and the results of the experiment regarding the maximum attainable capacity, as displayed in Figure 19b. The reason was discovered while inspecting the scanning electrons micrographs, as the pore volume for the inner part of the electrode seemed not to be tightly packed with discharge product. A rather significant amount of pore volume appears to be still available and was not completely filled. So the measured discharge capacity is, because of this, lower than the model predicted. Schematically illustrated in Figure 20 can be seen that the overgrow of discharge product on the outer parts obstructs the access to interior parts [31].

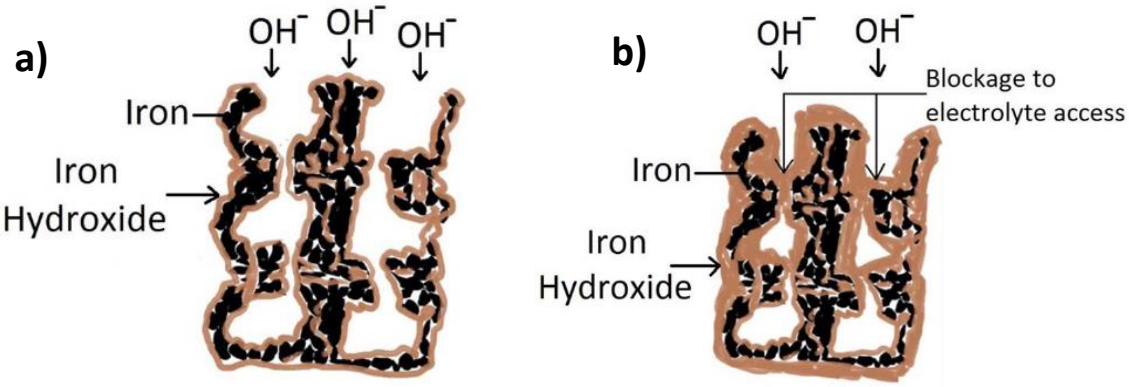

Fig. 20 Cross-section of a sintered electrode structure showing the unused pore volume at the end of discharging b), compared to the initial stage of discharge, a) [31].

The electrodes for the experiments with higher porosity had a larger thickness, which means that the unused inner part would be even worse utilized. So as far as the porosity concerning the porosity and thickness for the sintered electrode should be optimized to obtain the highest discharge capacity. The authors Yang et al. report a capacity of 0.5 Ah/g for their iron electrode at 85% porosity [31].

By means of adding pore formers particles, the effect of pore size was also examined as seen in Figure 21. Larger pores (90-105 µm) ensures better accessibility for the electrolyte but cannot provide a large amount of internal surface area compared to smaller pores (20-25 µm). The experiments conducted now showed a 21% increase in utilization for the electrode with smaller pore size compare to the larger pore size electrode (while having the same porosity %). This can be explained by the higher active surface being available.

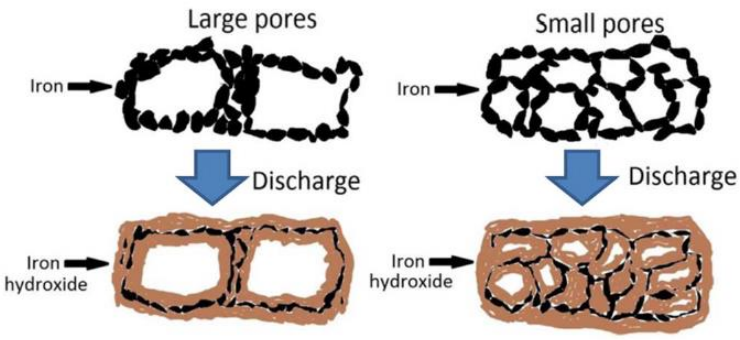

Fig. 21 Cross-section of sintered iron structure with large and smaller pores before and after discharge. Indicating that smaller pores provide a larger surface of the active material for discharging [31].

1.7.4. Nanoparticle structured electrode

In the last 20 years the incorporation of nanoparticles to gain a highly efficient iron electrode received much attention because of the surface area dependant performance. An obstacle which arises is the formation of iron oxide due to the increased reactivity of the nanoparticles during preparation. This substance is a poor electrical conductor and therefore hinders optimal functioning of the battery. Several tactics have been employed by scientists to overcome this problem, for example by the use of conductive materials. Nickel powder, a nickel foam and carbon black are considered as electrical conductive additives. Also, a more complex approach is possible as some researchers have created iron-carbon materials which should enhance electrical conductivity effectively. Figueredo-Rodriguez et al. [27] manufactured an iron-air battery and utilized iron nanocomposites electrodes in order to tackle the described issue.

1.7.5. Iron foam electrode

An unusual electrode concept is using iron foam as the anode material. Micro-and-nano porous foams display a high strength-to-weight ratio and large surface area per unit volume (and weight) while also being a good electrical conductor. These aspects provoke the interest in application as anode material for iron-based batteries. Four types of porous foams can be distinguished, as seen in Figure 22, which are applicable for the iron-air battery namely: open/closed cell structure and stochastic/non-stochastic cell structure. All come with their individual manufacturing processes and characteristics. For non-metallic foams, often additive manufacturing methods are involved. The production of metal foams is mostly performed with either metal powders in combination with a blowing agent, which undergoes a sintering process or via a metal in molten state where a gas source is used for creating porosity. In particular the stochastic cell structures are good obtainable for metals.

As the name implies, the open cell foam has an open structure that allows for the flow of gasses and/or fluids through the material. So, these porous cellular structures are interconnected and typically show a 70-98% porosity range. Because of the open pore structure, a relatively large specific surface area is present for reactions to occur compared to closed pore electrodes. Furthermore, the total density of open cellular foams is lower than for closed cell structures, which can be considered an advantage for battery usage [81], [120].

On the other hand, closed cell metal foams exhibit in general a lower porosity 10-70% and lower surface area but are in return mechanically stronger. Although these cells do provide a larger surface area compared to a flat solid metal, their usage is typically found in the field of structural and impact-absorbing materials due to their excellent combination of stiffness and lightweight. Therefore, if one would like to make optimal use of the beneficial properties foams supply (relevant for batteries), it is strongly suggested to search in the direction foams with an open cellular design.

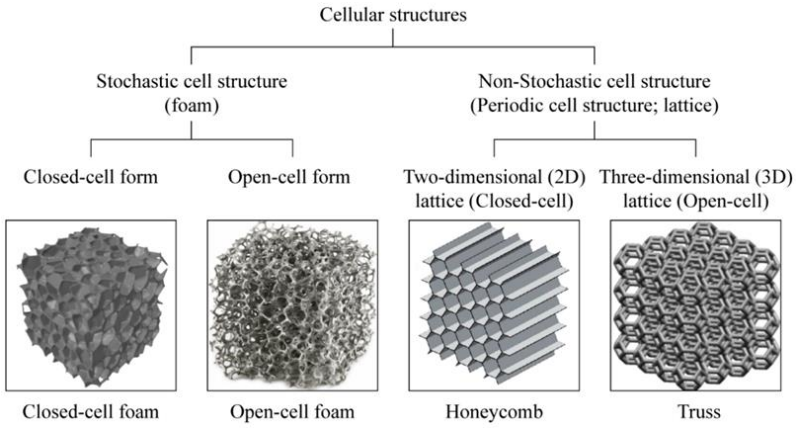

Fig. 22 Division of 3D cellular structures [144].

1.7.6. Overview electrode concepts reported in literature

Concept	Material	Preparation	Additive	Formation	Discharge & charge capacity	Reversibility	Ref.
Sheet	Fe	Polishing	-	Yes	6.8 µAh/cm^2 & 200 µAh/cm^2	>8 cycles (full cell)	[36]
Microparticles	3-5µm, Fe	Die pressing	8.5% Bi_2S_3; 5% PE	Yes	220 mAh/g_{Fe} & 300 mAh/g_{Fe}	>350 cycles	[83]
Microparticles	3-5µm, Fe	Pressed at 140°C	10% Bi_2O_3; 5% FeS; 10% PE; 10% K_2CO_3	Yes	240 mAh/g_{Fe} & 500 mAh/g_{Fe}	>1200 cycles	[58]
Microparticles	3-5µm, Fe	Coating of current collector & short sintering	10% graphite; 1% Bi_2S_3; 6% PTFE; 0.5% $NiSO_4 \cdot 7H_2O$	Yes	400 mAh/g_{Fe} & 500 mAh/g_{Fe}	>200 cycles	[84]
Microparticles	<10µm, Fe	Coating of current collector	11% FeS; 6% PTFE; LiOH; K_2S	Yes	230 mAh/g_{Fe} & 550 mAh/g_{Fe}	>50 cycles	[85]
Microparticles	1-10µm, α-Fe_2O_3	(modified) polyol method incl. NaBH4	10% PTFE	Yes	120 mAh/g & -	>35 cycles	[86]
Microparticles	3-5µm, Fe	Pressed at 140°C	8.5% Bi_2S_3; 6% PE	Yes	188.2 mAh/g_{Fe} & 200 mAh/g_{Fe}	>450 cycles	[87]
Sintered	3-5µm, Fe	Sintering in Ar at 850°C	NH_4HCO_3; Na_2S	Yes	192 mAh/g_{Fe} & 200 mAh/g_{Fe}	>3500 cycles	[31]
Nanoparticles	Fe/Fe_3O_4	Combustion of precur. & coating of current collector	10% carbon; 1% Bi_2S_3; 6% PTFE; 0.5% $NiSO_4 \cdot 7H_2O$	No	400 mAh/g & 500 mAh/g	>100 cycles	[88]
Nanoparticles	15-50nm, Fe_2O_3	Hot pressed at 200°C	10% carbon; 4% Bi_2S_3; 5% PTFE	No	400 mAh/g & 900 mAh/g	>20 cycles (full cell)	[27]
Nanoparticles	<50nm, Fe_2O_3	Loaded nickel foam	Carbon; 10% binder	Yes	<700 mAh/g & 1007 mAh/g	>100 cycles	[89]
Nanoparticles on carbon structure	<50nm, Fe_2O_3	Rolling of Fe_2O_3–filled CNT	10% PTFE	No	<500 mAh/g & 962 mAh/g	>30 cycles	[90]
Nanoparticles on carbon structure	<100nm, Fe_2O_3	Precipitation during hydrothermal method	Carbon; 10% PTFE	No	350 mAh/g & 1007 mAh/g	>29 cycles	[91]
Nanoparticles on carbon structure	<20nm, Fe_2O_3	Rolling of Fe_2O_3–filled CNF	10% PTFE; 2% Bi_2S_3	No	<550 mAh/g & 1007 mAh/g	>50 cycles	[92]
Nanoparticles on carbon structure	<100nm, FeO_x/graphene	Loaded nickel foam	Glucose; PTFE	No	<377 mAh/g & -	>300 cycles	[93]
Nanoparticles on carbon structure	<100nm, FeS/graphene oxide	Co-precipitation	10% PTFE; 10% carbon black; 3% Bi_2S_3; 0.5% $NiSO_4 \cdot 7H_2O$	No	<325 mAh/g & 400 mAh/g	>300 cycles	[26]
Foams	Fe	Corrosion, PTFE coating and erosion	Bi_2S_3 carbon	No	2.83 mAh/cm^2 & -	>25000 cycles	[94]

Table 4) Specifications of several experiments including the effect of the electrode structure

Table 4 on the previous page shows the capabilities of electrode concepts utilized in several research papers of the last years. It is however impossible to make a fair, direct one-to-one comparison between concepts since all experiments are conducted under specific circumstances. With four alternative electrode structures for the ordinary sheet electrode and a wide variety of preparation techniques in each study to incorporate additives, ranging from hot pressing and coating of current collectors to rolling of CNF with iron oxide particles. Moreover, mostly unique compositions of additive "mixtures" are employed at varying concentrations.

1.8. Research questions and hypotheses

The primary objective of this thesis is to explore how the microstructure of iron electrodes influences their susceptibility to particular redox reactions and their tendency to form oxides/hydroxides compounds. Furthermore, the effect of an iron foam material are probed next to the application of sodium stannate (Na_2SnO_3) as additive to the solution. Through comprehensive experimental investigations and analyses, the purpose is to elucidate the complex interplay between microstructure and oxidation/reduction behaviour in iron anodes, with the ultimate goal of enhancing the efficiency and lifetime of iron-air batteries.

The current work concentrates on the following main research question and sub questions:

- ***What is the influence of grain size, dislocation density and phases on the formation of iron oxide/hydroxide compounds and hydrogen evolution at iron electrodes in a strong alkaline solution?***

    - *How does an iron foam anode, exposed to a strong alkaline solution, influence the formation of iron oxide/hydroxide compounds and hydrogen evolution, compared to a solid iron anode?*

    - *What is the influence of sodium stannate added to a strong alkaline solution on the formation of iron oxide/hydroxide compounds and hydrogen evolution at iron electrodes?*

Based on the existing literature and the understanding of microstructural influences on electrochemical behaviour, the following hypotheses are proposed:

- **Grain Size:** It is hypothesized that the grain size of iron will affect the formation of a layer composed of oxide/hydroxide compounds. Grain refinement may facilitate the formation of a relative lower fraction of protective iron oxides and increasing donor density in the protective layer, leading to worsening of the barrier properties of the film. Moreover, grain refinement may increase oxidation rate due to a higher grain boundary density, which is more prone to dissolution.

- **Dislocation Density:** The dislocation density is expected to be influential to the electrochemical reactivity of iron electrodes. The dissolution rate increases due to the accumulation of dislocations, which increase the amount of active sites like kinks and steps at the surface. The presence of dislocations (line defects) at the substrate can be considered as an edge of point defect at the substrate/film interface. This could induce a oxide/hydroxide layer which exhibits a higher density of donors.

- **Phase constituents:** The effect of an additional secondary phase (martensite) in a steel in compared to a single (ferrite) phase is anticipated to decrease oxidation resistance because of the more disordered structure caused by the martensitic phase. Possibly, a more defective barrier is present with less formation of iron oxides/hydroxides species.

- **Sodium Stannate Trihydrate:** The addition of sodium stannate trihydrate to the electrolyte will (to a certain extent) suppress the evolution of hydrogen gas. Since the formation of a thin deposition layer consisting of Tin is expected to raise the overpotential for the HER.

- **Open-cell foam:** It is expected that the porous iron foam will showcase large faradaic currents during functional operation as enhanced electrochemical active surface area is present (in comparison to flat solid iron).

2. Experimental methodology and procedures

In the pursuit of enhancing the electrochemical performance of iron-air batteries, understanding the influence of microstructural parameters on the oxidation and reduction behaviour of materials becomes of paramount importance. However, to draw reliable conclusions from experiments, a systematic and careful approach to preparing the tests is required. In this chapter, methods and procedures are discussed that have been applied for each microstructural feature (and foam) specifically and in general. Moreover, two key electrochemical techniques which have been in this research are introduced and explained. These techniques are cyclic voltammetry and electrochemical impedance spectroscopy.

2.1. Anode materials

Several materials have been applied during the current research, all of which are mostly ferrous. To elucidate the effects of microstructure and topology characteristics, (nearly) pure iron, a dual phase steel and an porous iron foam are employed. The specifications of these materials are clarified in this section.

2.1.1. Rolled iron

As-received hot-rolled and cold-rolled iron samples from Armco® (AK Steel, The Netherlands) are applied. Both materials are of high purity iron with composition as seen in table 5, which is provided:

	Fe	Mn	Cr	Ni	Cu	N	S	P	Si	Sn	C
Wt.%	99.912	0.04	0.014	0.012	0.007	0.003	0.003	0.003	0.003	0.002	0.001

Table 5) Chemical composition cold and hot-rolled iron

The thickness of the hot-rolled and cold-rolled specimens are 3 mm and 2.5 mm, respectively. As observed with the naked eye, the hot-rolled iron is characterized by a scaly/rough surface while the cold-rolled material has a smooth surface finish.

2.1.2. Dual phase steel

A supplied dual phase steel grade; DP1000 (M2i NWO) is utilized to reveal the effect of a secondary phase (martensite) in the microstructure during electrochemical experiments. The chemical composition is provided and confirmed via XRF analysis and a LECO test, seen in table 6.

	Fe	C	Si	Mn	P	S	Al	Cr	Cu	Mo	Ni	Sn	Ti	Ca	V
Wt.%	96.92	0.141	0.051	2.149	0.013	0.014	0.041	0.576	0.012	0.004	0.021	0.001	0.032	0.022	0.007

Table 6) Chemical composition DP1000

The thickness of the DP1000 material is 1 mm and has priorly been cold-rolled, resulting in a smooth surface finish.

2.1.3. Iron foam

A supplied open-porous iron foam is applied to show the effect of the topology of the iron electrode during electrochemical tests. The XRF test which was conducted showcases high iron content along with some important impurities (Si and Mn) and (likely) a surface contamination of Na. The chemical composition in its entirety is seen in table 7 below.

Compound	Fe	Si	Na	Mn	Al	Ca	Mg	P	S	K	Cl
Conc.(wt%)	98,549	0,391	0,343	0,339	0,096	0,093	0,092	0,039	0,033	0,013	0,012

Table 7) Chemical composition of the iron foam

The as-received foam shows signs of rust at specific locations, as observed with the unaided eye and superficial pores are visible. The thickness of the porous iron material is 1 mm while being easily bendable.

2.2. Microstructure design

The effect of grain size, dislocation density and phase constituents are of interest in current thesis. The methods which have been used to get differences at these features are explained in this section

To assess the effect of grain size, the previously described hot-rolled iron samples are subjected to distinct heat treatments to produce three relatively different grain sizes: small, medium, and large. An electrical heated laboratory furnace is used for the treatments. Pre-set annealing temperatures of 800, 1000 and 1200°C are applied. The appropriate sample size is made using a metal sheet press cutting machine (Cidan) to the dimension: 33 x 33 mm^2 (also all other sheet iron samples are cut by this machine). The samples are cleaned with isopropanol and air dried before being putting them in the oven. The iron specimens are placed in the oven and heated for 30 minutes under argon gas atmosphere. Afterwards, the samples are quenched by submerging them in a large water bath of room temperature (Figure 23).

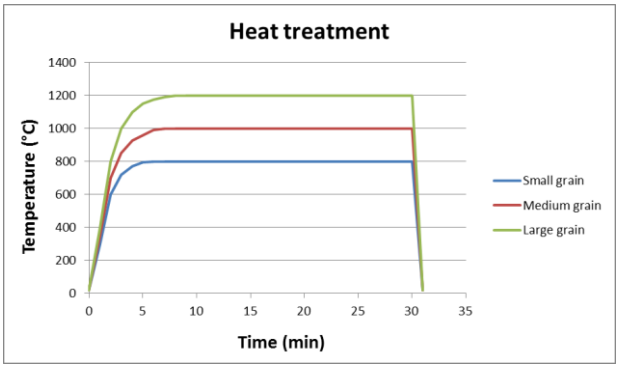

Fig. 23 Course of heat treatment for three hot-rolled iron samples. The graph is purely illustrative and does not contain actual measured temperature profiles

Based on literature and general understanding of rolling processes on the microstructure, it is assumed that the supplied cold and hot-rolled iron materials do already differ in dislocation density (and possibly also texture). Therefore, treatments in which the microstructures could be altered are not applied. Surface identification via EBSD is performed to reveal these differences. In order to elucidate the effect of the dual phase material composed of ferrite and martensite, it is chosen to compare this material to pure cold-rolled iron. Since the latter is solely composed of α-Fe (ferrite) at atmospheric pressures and ambient temperature, while also having been exposed to a cold working process. The electrochemical behaviour of the iron foam with porous structure is compared to the solid iron samples. Given the inherently different macrostructure of the foam compared to the solid iron samples, performing additional (heat) treatments was redundant.

2.3. Surface preparation

Prior to electrochemical tests, the specimens benefit from surface preparation in order to accurately determine the effect of microstructural features. The as-received materials can be affected by surface contaminations and irregularities which is unwanted. The sample preparation of the iron sheet specimens consisted of the following steps. First, the samples are sanded with SiC sanding papers (Struers) with 80 up to 2000 grit size, whereby isopropanol is applied as fluid to expel debris during grinding. Next, the samples are polished with liquid diamond slurry with 3 µm, 1 µm and finally OP-S. Afterwards, the samples were cleansed in an ultrasonic bath for 10 minutes while being immersed in ethanol. Lastly, the samples were blown dry with compressed air.

Due to the unusual structure of the foam, an alternative treatment is applied. Herein, the specimens are cut with a scissor to the dimension of approximately 33x33 mm^2 and are submerged in a two component solution which was composed of concentrated HCl with 50g/L $SnCl_2$ and 20g/L $SbCl_3$. The foam sample was stirred for 30 sec in this solution, subsequently rinsed with deionized water and immediately afterwards dried with a cloth and hot-air for 10 min.

2.4. Surface characterization

The hot-rolled iron samples which have been subjected to the previously described heat treatments, are prepared as mentioned in section 2.3. After that, etching with Nital 2% solution is utilized to expose the grain boundaries for further microscopy observations. Digital microscopy analysis for grain size verification is conducted. Inspection with optical microscopy (OM) (Keyence) allows for identification of grain characteristics. The grain size was determined by a technique which involves drawing multiple straight (horizontal and vertical) lines on the micrographs, where the intercepts with the grain boundaries are counted. The average grain size was calculated by dividing the counted intersections by the actual line length.

Regarding the as-received hot and cold-rolled samples, EBSD analysis was applied to examine differences in grain structure, the density of Geometrically Necessary dislocations (ρ_{GND}) and (preferred) crystallographic orientations. The samples surfaces are prepared as

described in the previous section whereby an additional polishing with a Vibro Automatic polishing machine was necessary for around 24 hours. EBSD measurements were conducted where a step size of 0.2 µm and working distance of 13 mm are applied. An area of 500x500 μm^2 is probed for the hot-rolled and cold-rolled sample. The obtained data is further processed in OIM analysis software and Image J as an additional tool. A quick inverse pole Figure was selected to get a stereographic projection of grain orientations, where the appropriate cubic structure (BCC) was chosen. Image J is used to further quantify the crystallographic orientations along with the grain size. A GND map is calculated from the local misorientation according to the method of [124]. A maximum misorientation angle of 5°C is used along with the third nearest neighbours for the misorientation calculations. Using a method which includes some coding and excel, the average ρ_{GND} is calculated.

The exact phases and phase fractions present in the DP1000 steel are analysed using the Scanning Electron Microscope (SEM) and clarified in combination with research papers which have investigated DP1000. Identification with SEM consisted primarily of taking images of the surface at certain magnifications to display the dual phase structure. Additionally, Image J is employed to determine more accurately the phase fractions which are present in the material.

Optical microscopy, SEM, Archimedes immersion test and Atomic Force Microscopy (AFM) analyses were performed in order to learn more about the cellular structure, porosity, density and micro-roughness. OM and SEM inspection were used to discover the porous network and some microstructural aspects of the iron foam by taking images at several magnifications. An immersion experiment allowed to accurately determine the volume and density of the sample. Subsequently, the porosity could be calculated and be validated via the method of simply measuring a fixed dimension of a piece of foam and weighing. The AFM is applied to investigate the topography on micro-scale of the foam as well as to acquire images on sub-micro scale. For this, a tapping mode was applied on several surfaces of the foam struts. The preparation for most of these techniques consisted solely of blowing the foam samples with compressed air.

2.5. Electrochemical characterization

For all applied materials, it's aimed to keep the experimentation parameters as similar as possible for optimal comparison purposes. For the solid sheet iron materials this was feasible. For the iron foam, slight adjustments of some settings were required as issues arose, which will be discussed in the results and discussion chapter.

The solid iron samples intended to study the effect of microstructures, were evaluated according to the following electrochemical methods. Chronoamperometery (CA), Cyclic voltammetry (CV) and electrochemical impedance spectroscopy (EIS) were carried out to analyse the oxidation and reduction kinetics and impedance (resistance) of the system. The electrolyte is composed of 6M KOH and 0.01M $Na_2SnO_3 \cdot 3H_2O$ dissolved in distilled water at ambient conditions. The experiments were held in three-electrode system consisting of a Hg/HgO reference electrode, a platinum wire counter electrode and the iron samples acting as working electrode. Initially, chronoamperometry was applied for 120 seconds, in which the iron was cathodically polarized at -1.3V (vs. Hg/HgO) and a stable current density reached. CV measurements follow, starting at -1.3V (vs. Hg/HgO) towards -0,1V and back. This repeated until 12 cycles are completed while a linear scan rate of ν = 5 mV/s is implemented. Then, one extra half cycle is executed towards -0.1V. Subsequently, CA was applied to polarize the samples at -0.1V for 300 seconds. Finally, EIS spectra are collected of the samples. A frequency range of 100 kHz to 10 mHz is used with a sinusoidal amplitude of 10 mV. The obtained EIS data is further examined using the "Zfit" function, available in the EC-lab software. As opposed to the non-porous iron specimens, the initial CA settings for the iron foam are set to -1,0 (vs. Hg/HgO) for 300 seconds. The remaining parameters are kept the same.

2.6. Electrochemical techniques

2.6.1. Cyclic voltammetry

In battery research, several electrochemical tests and techniques are commonly used to characterize and evaluate the performance of batteries. The choice of test depends on the specific objectives of the research, the type of battery being studied, and the information researchers seek to obtain. Cyclic voltammetry (CV) is an electrochemical technique used in analytical chemistry and materials science to study the reduction and oxidation properties of chemical compounds and materials due to electron transfer processes. It provides valuable information about the electrochemical behaviour, kinetics, and thermodynamics of redox reactions. In CV, a potentiostat supplies a triangular potential waveform to an electrochemical system (e.g. three electrode setup). This is performed by ramping the potential at the working electrode linearly versus time from an initial potential to a switching potential and subsequently to a final potential. The rate at which this happens is referred to as the scan/sweep rate "υ". The resulting current response is measured, which comprises both faradaic and non-faradaic current and is set out against the potential. A characteristic shape which is seen in Figure 24. is typically obtained for a simple reversible redox couple of an analyte in solution [137].

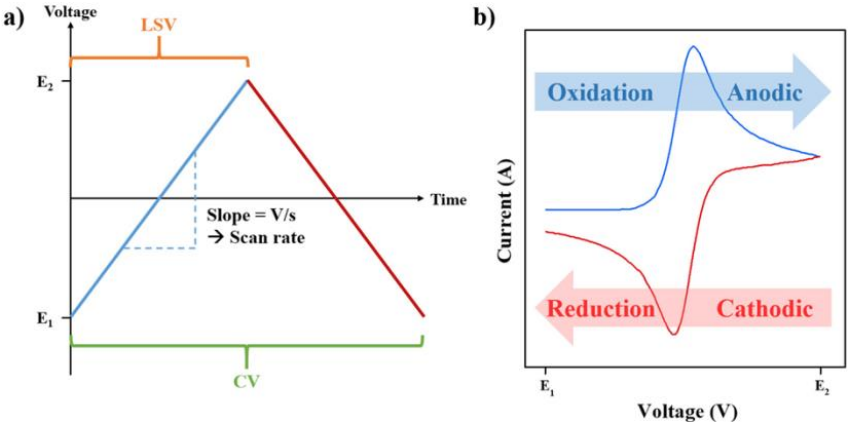

Fig. 24 a) Triangular, linear voltage sweep as a function of time. b) Direction convention oxidation and reduction scan for a reversible redox reaction

The forward scan (in blue Figure 24) is related to the oxidation of a species at the working electrode. At the initial stages of the voltammogram (horizontal segment), only a capacitive current is present. At a certain potential between E1 and E2, a kinetic region is reached where oxidation starts to take place and the current rises. The current "i" [A] at this instance can be described by the Tafel equation according to equation 21, which is derived from the extended Butler-Volmer equation:

$$i = nkFC \exp(\pm \alpha F \frac{\eta}{RT}) \qquad (21)$$

Herein, "n" is the amount of electrons exchanged, "k" the reaction rate constant [s^{-1}], "F" the Faraday constant, "C" is the concentration of reactive species at the surface of the electrode [mol/m^2], "R" the universal gas constant, η is the overpotential in [V], "T" the absolute temperature and "α" the charge transfer coefficient. The plus/minus sign in the exponent is applied for the anodic/cathodic reaction, respectively. It indicates that the current is proportional to the voltage and the process is under electron transfer limitation.

Next, the current rises rapidly until a peak appears which is often denoted as i_{pa} at a potential E_{pa}. Similar notation is used for the cathodic peak, observed during reduction. Species are now getting oxidized and the process is under mass transport control (or diffusion control). The peak develops due to the depletion of available molecules near the electrode surface to oxidize. The peak current can be considered as the fastest rate of oxidation (i.e. the maximum number of a specific species getting oxidized per second). When the conversion of most species has taken place, unoxidized molecules in the bulk solution need more diffusion time to the electrode surface. As a result, the current decays at a given moment due to a lower rate of oxidation [137].

The scan rate is an important parameter in CV, since large scan rates lead to decrease in diffusion layer and thus to higher currents. For the peak current this can be described by the Randles-Sevcik equation which shows a proportional relationship between the current and the square root of the scan rate [137]:

$$i_p = 0.446nFAC^0\left(\frac{nF\upsilon D_o}{RT}\right)^{1/2} \qquad (22)$$

Where, "n" is the amount of electrons exchanged during the redox reaction, "A" is the surface area of the electrode [cm^2], "F" the Faraday constant, "C^0" is the bulk concentration of the analyte [mol/cm^3], "R" the universal gas constant, "T" the absolute temperature, "υ" is the scan rate [V/s] and "D_o" is the diffusion coefficient of the oxidized analyte. The equation is valid for an electrochemically reversible electron transfer process which involves freely diffusing redox molecules. Any deviation from linearity in i_p vs. $\upsilon^{1/2}$ could suggest electrochemical quasi-reversibility. This would be expressed by observing peak-to-peak separation shifts with scan rate.

Moreover, Randles-Sevcik formula could indicate whether an analyte is freely diffusing in solution or be an adsorbed species to the electrode surface. As for the latter case, the current response is described by [137]:

$$i_p = \frac{n^2F^2}{4RT}\upsilon A\Gamma^* \qquad (23)$$

Where Γ^* is the surface coverage of the adsorbed species [mol/cm^2]. Now, the current response is expected to vary linearly with the scan rate.

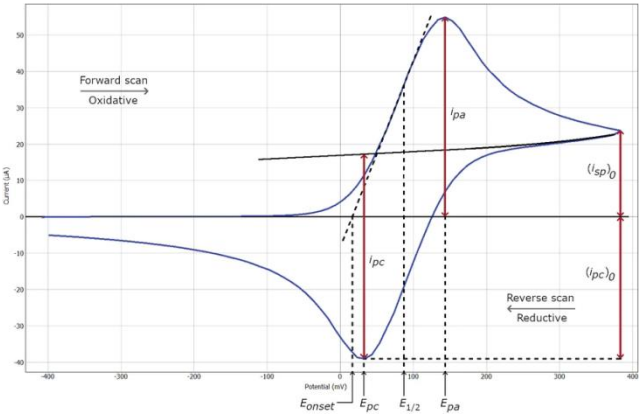

Fig. 25 Peak potential (E_{pa}, E_{pc}) and peak current (i_{pa}, i_{pc}) location [138].

2.6.2. Electrochemical impedance spectroscopy

Electrochemical impedance spectroscopy (EIS) is powerful technique used to analyse the electrical impedance of an electrochemical system over a range of frequencies. It finds extensive use in various fields such as battery research, fuel cell characterization and corrosion analysis. EIS offers valuable understandings into the intricate phenomena taking place at the interface of the electrode and the electrolyte. In potentiostatic EIS, a potentiostat applies a small sinusoidal potential to a electrochemical system (typically a perturbation an electrode surface) where a corresponding sinusoidal current (alternating current, AC) output is measured. The electrochemical response provides information about oxidation mechanisms and reaction kinetics. The input sinusoidal signal can be represented by [125]:

$$E(t) = E_0 \sin(\omega t) \tag{24}$$

Herein, the potential E is a function of time [t] where E_0 represents the magnitude of the applied potential [V] (amplitude) and ω angular frequency [rad/s]. Similarly, the corresponding output current has the same attributes and is given by:

$$i(t) = i_0 \sin(\omega t - \phi) \tag{25}$$

However the output response might display a phase shift (offset) relative to the input potential signal which is indicated by ϕ [rad]. So, an EIS experiment is centred around a potential set point (E_0) where a wide range of frequencies (e.g. 10^{-2} to 10^5 Hz) is examined and the output current signal is registered over the same frequency spectrum. Next, a Fourier transform is performed of both signals to convert the data from the time domain to the frequency domain. This is done in order to calculated the impedance (Z) which can be seen as a complex resistance in a circuit for an alternating current.

Furthermore, electrochemical cells can be modelled as a network of electrical circuit elements to construct an equivalent circuit. Bode and Nyquist plots can have supporting role in the (manual) modelling procedure, although such a circuit is usually created with specialized software with fitting tools. The response of an equivalent circuit can be computed and compared with the real EIS response of the electrochemical system. The most common electrical elements include: a resistor, capacitor and inductor. Using Eulers equation, the impedance can be expressed as follows [125]:

$$Z(\omega) = \frac{E(\omega,t)}{I(\omega,t)} = |Z| \cdot (\cos(\phi) + j \sin(\phi)) \tag{26}$$

Processing the impedance data is useful since the data can conveniently be illustrated via Bode plots, Nyquist plots and electrical equivalent circuits which allow for easier interpretation of the results. The Bode plot shows the magnitude of the impedance (and often also phase angle) set out to the applied frequency range on the x-axis. Another mathematical method to represent the same information is via the Nyquist plot. Herein the magnitude of the impedance is separated into a real and (negative) imaginary part, after converting the polar coordinates of equation (z) to Cartesian coordinates. These representations help to distinguish different electrochemical phenomena that take place at different characteristic frequencies.

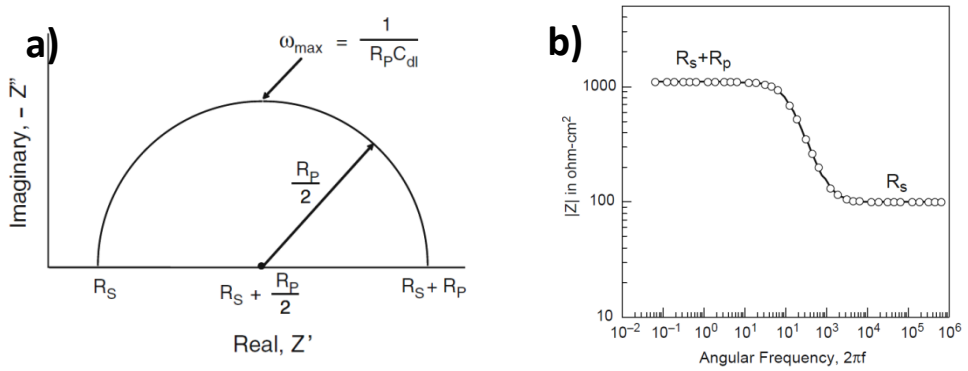

Fig. 26 a) Representation of a Nyquist plot. b) Representation of a Bode plot.

Furthermore, electrochemical cells can be modelled as a network of electrical circuit elements to construct an equivalent circuit. Bode and Nyquist plots can have supporting role in the (manual) modelling procedure, although such a circuit is usually created with specialized software with fitting tools. The response of an equivalent circuit can be computed and compared with the real EIS response of the electrochemical system. The most common electrical elements include: a resistor, capacitor and inductor. For a relatively simple situation, namely a metal/solution interface the equivalent circuit configuration is shown.

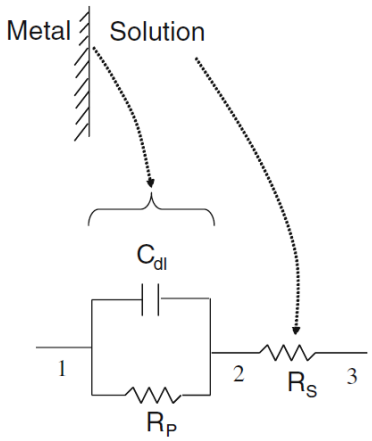

Fig. 27 Equivalent circuit for a metal/solution interface

In the circuit in Figure 27, a capacitor Cdl is applied to simulate the capacitance behaviour of the edl with in parallel a resistor Rp for the polarization resistance (charge transfer resistance) and in series connected component Rs to represent the solution resistance between the double layer and the reference electrode [125].

2.7. General procedures and cell design

During all experiments in this report, the same cell design is applied for electrochemical testing. The custom made cell is used as a three-electrode system, consisting of a working electrode, reference electrode and counter electrode. In Figure 28a. all components of the cell are exposed, which shows bolts, washers and nuts used to tighten the plates. These plates are transparent acrylic panels, forming the casing of the cell. One panel (Figure 28b) has a large circular opening in the which functions as the reservoir for a solution and allows for the placement of the three electrodes in close vicinity. A cylindrical hole is drilled at the top side to incorporate a mercury/mercury oxide (Hg/HgO or MMO) reference electrode. Two silicon gaskets (blue outline) surround the platinum wire, the counter electrode, to prevent leakage of fluids. The sheet iron material which functions as the working electrode has copper tape pasted to the (unpolished) backside. This conductive tape facilitates a connection between working electrode and the working electrode connector wire of the biologic station (Biologic Sp-200 potentiostat). A black rubber ring avoids leakage on the side of the iron sample. If a foam was applied as electrode material, a thick silicon gasket was inserted as well since it was more prone to leakage due to its porous structure. Tests in which leaking electrolyte was observed at any moment of the experiment were rejected.

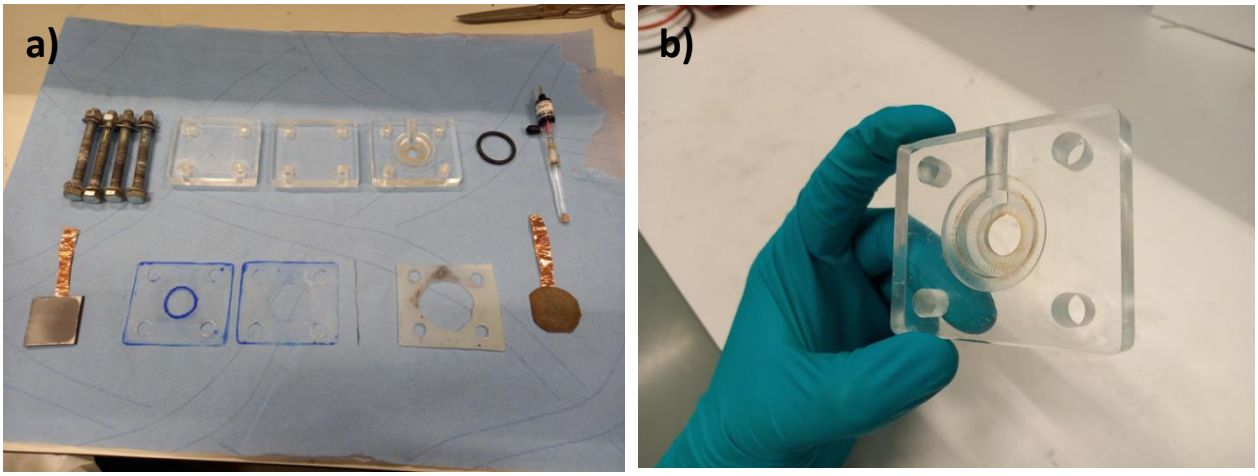

Fig. 28 All parts and components for the cell assembly displayed, a). Accidental contact of the electrolyte during disassembly and leakage issues caused the bolts to slightly corrode over time. b), a close-up of the middle acrylic plate.

In Figure 29. the assembly is shown in consecutive steps:

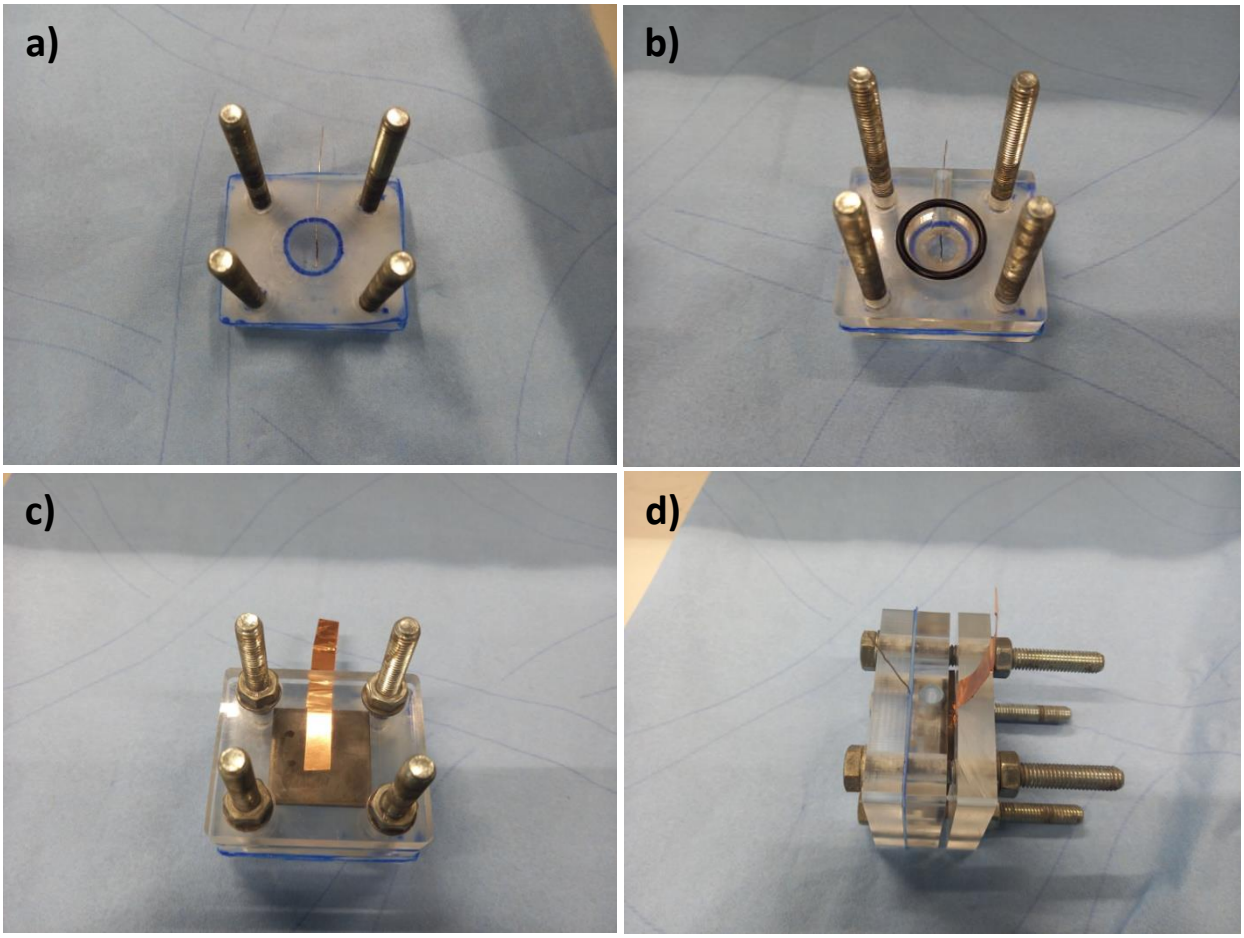

Fig. 29 Step by step construction of the cell. First, bolts are put through the four holes of an acrylic plate and on top, the platinum wire is placed in-between two silicon slabs, a). Next, the middle panel is positioned with a rubber ring to seal on the sample side, b). Then, the sample is placed with the polished side inwards, on the black ring and the nuts are fixed tightly, c) and d).

During assembling, special attention was paid to positioning the platinum wire flat and in the middle of the opening. Also, the square iron sample was carefully placed as the corners were in close proximity of the bolts. A connection between the iron sample and the steel bolts could affect measurements. After the cell has been assembled, a syringe was used to fill the inner compartment with a solution of 6M KOH and 0.01M Na_2SnO_3. The solution was injected in the opening for the reference electrode. A volume of approximately 5ml of solution could be inserted. Next, the Hg/HgO electrode was placed in this hole, where the tip was did not make contact with the bottom.

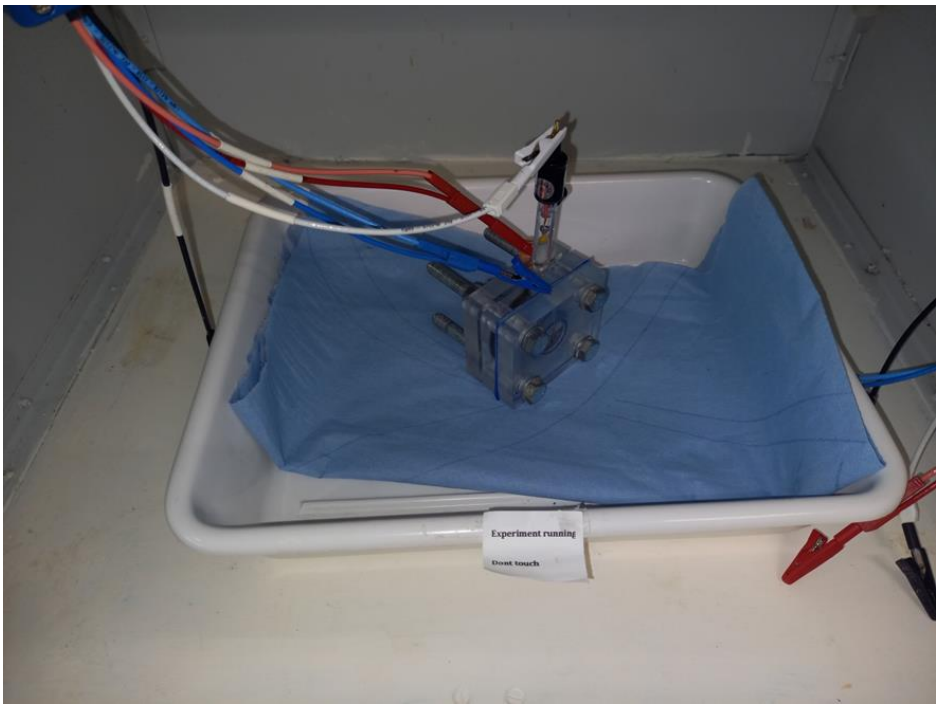

Fig. 30 The cell connected to the potentiostat. The red wire is connected to the copper tape of the iron electrode (working electrode), the white cable is clamped to the Hg/HgO reference electrode and the blue cable to the platinum wire (counter electrode).

Finally, the set-up is put inside a metal enclosure which acts as a Faraday cage to restrict external electromagnetic fields to interfere with processes occurring in the cell during experiments. The reference MMO electrode which was connected to the white wire of the potentiostat had such a tight fit that additional mounting of this component to keep it steady was practically redundant. All experimentation is performed while keeping conditions and parameters as constant as possible. In the context of reliability of the experiments, all tests are repeated (at least) two times to the ensure repeatability and acquire meaningful results to draw conclusions from. Furthermore, tests have also been conducted in an electrolyte consisting of solely 6M KOH. All experiments in which 0.01M Na_2SnO_3 is not added to the alkaline solution have the same procedures as the ones in which sodium stannate is used.

3. Results and discussion

The results of the identification and electrochemical experiments are covered in this chapter. Each individual microstructural aspects is dealt with in a separate sections in to present results in an organized manner. After that, the results of the foam is displayed and discussed. At last, tests results are shown where sodium stannate has not been added to the solution.

However, due to the striking resemblances in CV curves in general, for the solid samples, an initial section is dedicated to describe the behaviour which is seen for all these specimens. The following sections will go to in detail clarifying the effect grain size, phase constituent and dislocation density. Throughout these sections, the most representative CV curves of the repeated tests per sample will be shown.

3.1. characterisation of the anode materials

3.1.1. Annealed hot-rolled samples

Figure 31 shows the micrographs of the heat treated hot-rolled samples after etching with 2% Nital. Relatively small and equal sized grains are observed for the sample heated up to 800°C. Quite larger grains are seen for the specimen heated to 1000°C and a large variation in grain size is present. For the sample heated at 1200°C, the largest grains are realized (on average), where a relatively large grain size spread is seen. By means of the line intercept method with grain boundaries, the following average grain sizes are obtained (95% CI):

Sample	***Grain size (µm)***
Small (800°C)	38 ± 5
Medium (1000°C)	236 ± 97
Large (1200°C)	344 ± 129

Table 8) Calculated average grain sizes

The grain size distribution looks heterogeneous for the medium and large grain samples across the total surface area, making it challenging to accurately determine the average grain size. Therefore, rather large confidence intervals are obtained. Observing the micrographs, it can be faintly observed that medium and large-grain iron samples have stripes across their surface. Likely sub-optimal polishing could be the reason for this. In hindsight, shorter annealing times (and lower annealing temperatures) could have been applied to obtain more homogeneous and slightly smaller grain sizes for the relatively larger-grained samples. On the other hand, the differences in grain size between small and large, are in the current report immense and consequently very clear.

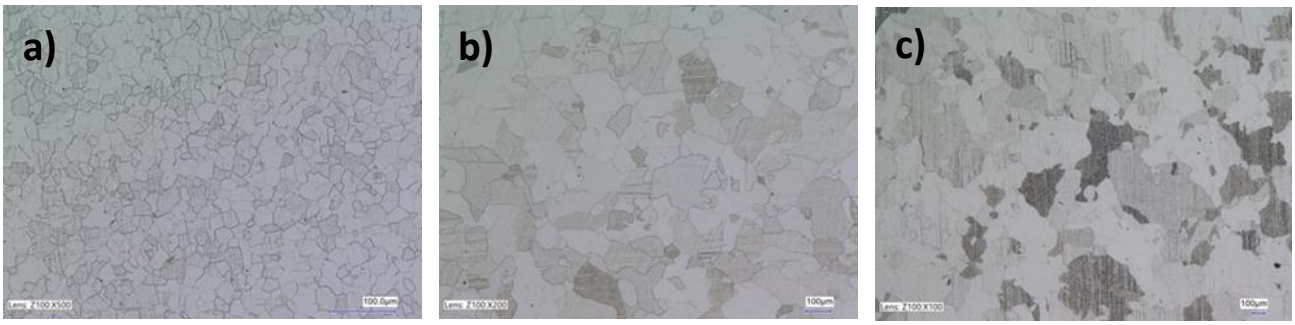

Fig. 31 Micrographs of hot-rolled iron heat treated at a) 800°C, b) 1000°C and c) 1200°C obtained with the optical microscope.

3.1.2. Hot-rolled and cold-rolled iron

Due to the additional rolling process the cold-rolled iron has undergone (with respect to the hot-rolled material), the defect density in this material is supposedly higher. More specifically, differences are expected in the density of geometrically necessary dislocations (ρ_g) and possibly crystallographic orientations. Therefore, EBSD analysis of the materials has been performed to reveal differences present between hot-rolled and cold-rolled. The specifications for the EBSD includes a step size of 0.2 µm and working distance of 13 mm. An area of 500x500 µm is probed in each case. The result is seen in Figure 32.

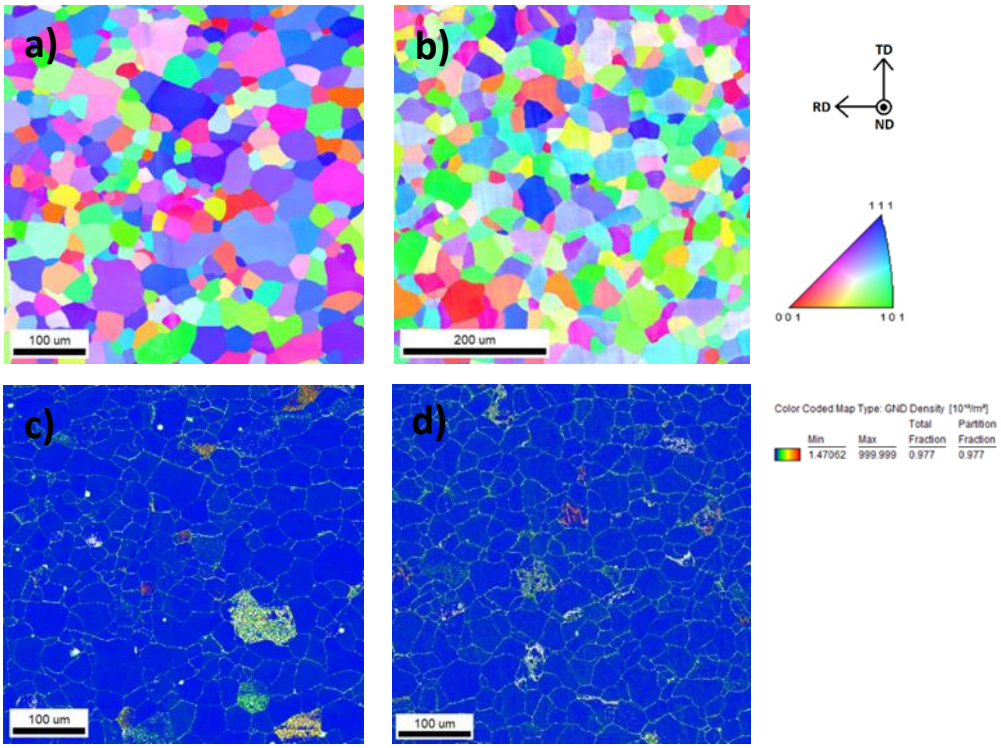

Fig. 32 EBSD results. IPF figures cold and hot rolled; a) and b), respectively. GND map cold and hot-rolled; c) and d), respectively

The inverse pole Figures (IPF) are shown in Figure 32. along the normal direction (ND). It is found that both samples consists solely of a BCC crystal structure and therefore possess a completely ferritic microstructure. Furthermore, equiaxed grains are observed and traces of inclusions are not detected within the resolution limits of the measurements, which is understandable given the high purity.

The spatially resolved crystallographic orientations are seen in the IPF maps and illustrate that both samples do not exhibit a strong texture. The cold-rolled material is seen to be (slightly) inclined towards the <111> // ND crystallographic orientation, while the hot-rolled specimen shows a weak preference for the component <101> // ND . Both of these observation are confirmed via ImageJ, which allows to distinct the colours (RGB) and determine their relative intensity. The procedure is described in appendix D.

Dislocations in crystalline materials are composed of geometrically (GND) necessary dislocations as well as statistically stored dislocations (SSD). SSDs are a type of dislocation in a crystalline materials that accumulate due to random trapping processes during plastic deformation. This accumulation can be caused through a process of multiplication (originating from a Frank-Read source for example), where dislocations coincidentally encounter each other. Dislocations that result from such occurrences are referred to as statistically stored dislocations. The corresponding density of these dislocation is often denoted as ρ_s [127].

On the other hand, some dislocations are formed due to the necessity of accommodating plastic deformation in regions where the crystal lattice cannot smoothly deform without the presence of additional dislocations. These dislocations (GNDs) are required from a geometric perspective to enable the crystal lattice to adjust to the applied strain or deformation. Unlike statistically stored dislocations, which arise randomly during deformation, GNDs have a non-random distribution and are strategically located in regions where they are needed to enable plastic deformation. The total dislocation density for a material is given by the sum of GND and SSD densities (i.e. $\rho_g + \rho_s$) [128].

In Figure 32. the corresponding GND density maps are displayed which show similarities in GND density. A method is applied which involves extracting a fraction of the more than 7 million GND density values in total (per map) and taking the average of these points. This is performed in such a manner that values are evenly selected across the total area of the maps (no random selection). The GND densities are calculated to be $\rho_g = 48 \pm 13 \cdot 10^{12}$ m^{-2} and $\rho_g = 56 \pm 11 \cdot 10^{12}$ m^{-2} for cold-rolled and hot-rolled, respectively. Thus surprisingly indicating that clear differences are not present in terms of ρ_g.

The expectation was that elongated grains in the rolling direction would be visible, as well as an larger GND density for the cold-rolled iron. Determination of the grain size indicate a nearly identical values: 28 ± 5 µm and 29 ± 4 µm, for “cold” and hot rolled iron, respectively. For convenience, some comparisons are made with the annealed hot-rolled iron anodes in the CV and EIS results section, to detect possible differences. An important note is that the hot and cold rolled samples described in this section are not subjected to any additional (heat) treatment.

3.1.3. Phase constituents

The cold-rolled DP1000 steel is examined under the Optical microscope and SEM after being etched with 2% Nital. The micrographs showcase a quite homogenous distribution of two phases across the surface. These phases can be identified as ferrite and martensite [129]. A ferritic matrix with regions of martensite can be observed with an islands-like appearance. Image J software allowed for phase fractions determination (appendix A) which resulted in 38% ferrite and 62% martensite, using the SEM image in Figure 33b. For the electrochemical tests results, it is decided to apply the earlier used cold-rolled pure iron for comparison purposes with respect to the DP1000 material, as the former was revealed to be fully ferrite phase.

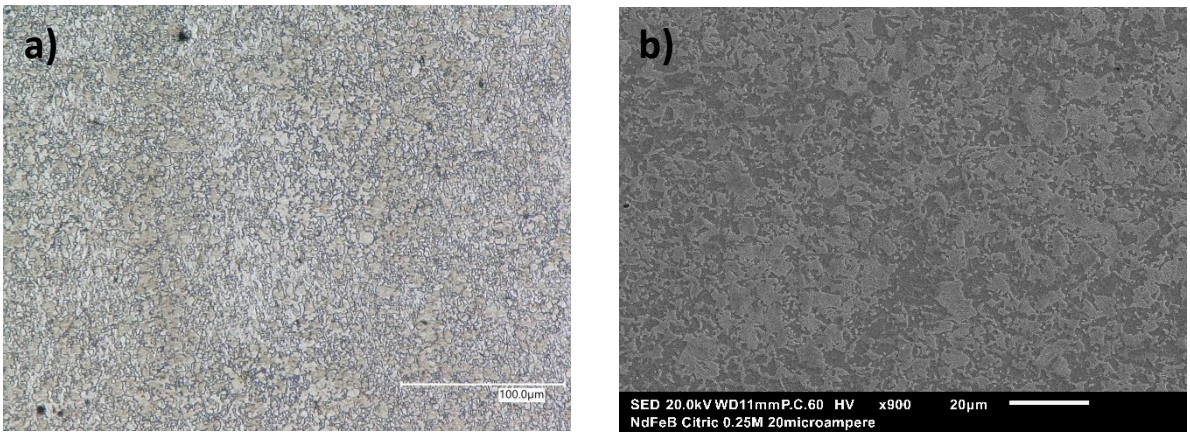

Fig. 33 a) optical microscope image showing global microstructure. b) SEM image displaying more detailed phase constituents

3.1.4. Topology – Iron foam

In the SEM Figure 34, the cellular structure of the iron foam is revealed. The stochastic structure of the porous network contributes to a system which consists of pores with different sizes. Based on estimations of SEM images, the pore size ranges from 50-500 µm while the strut (rod-like connections) thickness is typically 50-100 µm. The porosity is determined to be 69.5% using Archimedes principle of water displacement in combination with measuring and weighing a fixed dimension of a (large) piece of foam.

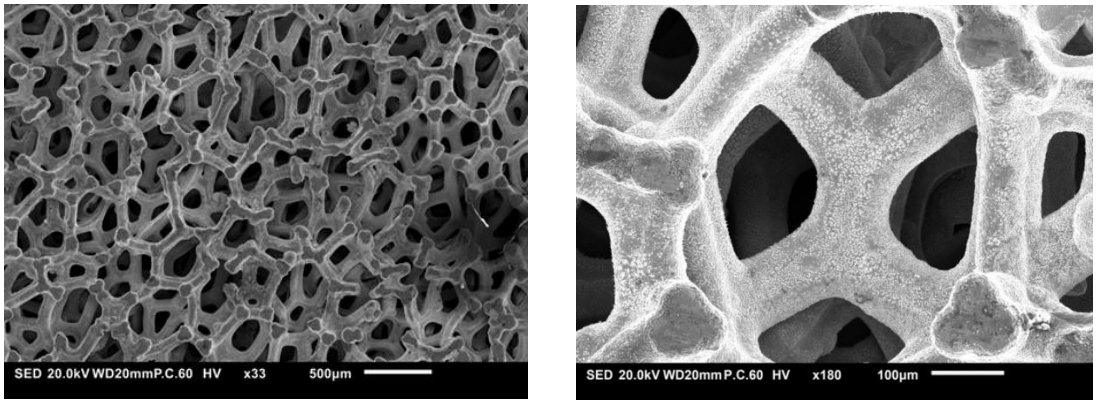

Fig. 34 SEM photos reveal the cellular structure of the iron foam

The AFM allowed for characterizing another property like the (micro)-roughness of the material and higher magnified images of the foams microstructure. A higher magnification on the top level surface (Figure 35a), indicates that the porous iron is composed of small micro particles in the range of ±2µm. This observation leads to think that a sintering process has been employed with fine powdered iron to produce this porous network. Likely, small iron particles have been mixed with so called sacrificial space filler material, which create a spaces of void in the foam. During or after sintering, these fillers dissolve or thermally degrade upon. What remains is an open-cell foam where iron particles have fused while (ideally) all residual pore forming powder is gone. This process is more thoroughly described by Kennedy et al. [130].

On top of that, AFM identification also seems confirm the presence of the microparticles. Additionally, the micro-roughness of the foam has been determined by scanning a surface along the struts direction (not the top level as in Figure 35a) which resulted in a roughness of 350 nm (RMS).

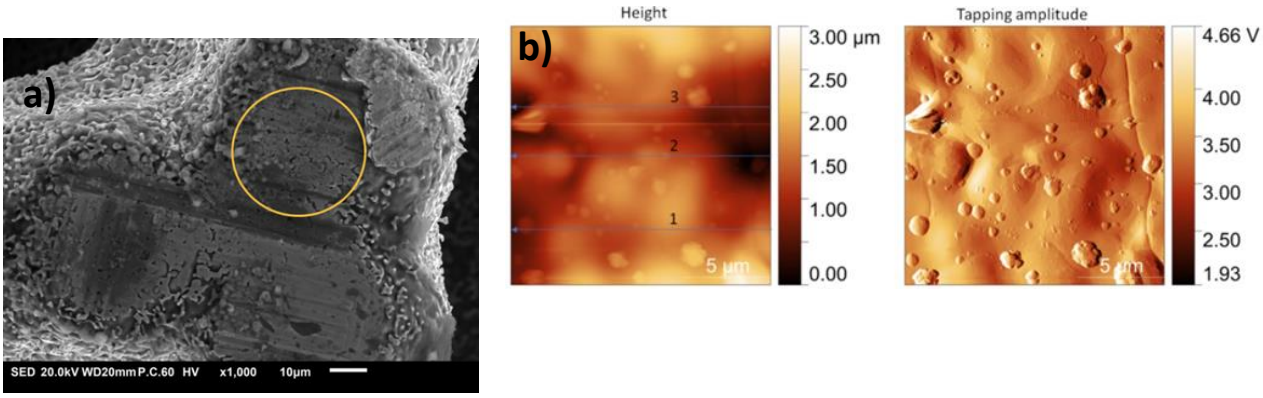

Fig. 35 a) Highly magnified SEM image with a yellow circle indicating the presence of iron micro particles. b) AFM data of the height profile to indicate roughness, using tapping mode

3.2. CV behaviour observed during experiments

3.2.1. General CV course

Half-cell tests are performed where iron anodes act as working electrode, a platinum wire as counter electrode and Hg/HgO electrode (MMO) functioning as reference electrode. Electrochemical tests are performed by means of cyclic voltammetry (CV) and potentiostatic electrochemical impedance spectroscopy (PEIS) in order to identify the conversion reactions taking place and the charge transfer processes (resistance) of the involved species for the tested specimens.

Among repeated tests of flat, non-porous samples, the CV graphs are globally similar in shape. Below in Figure 36. the CV curve for a small grain sample test is shown to illustrate the typically course.

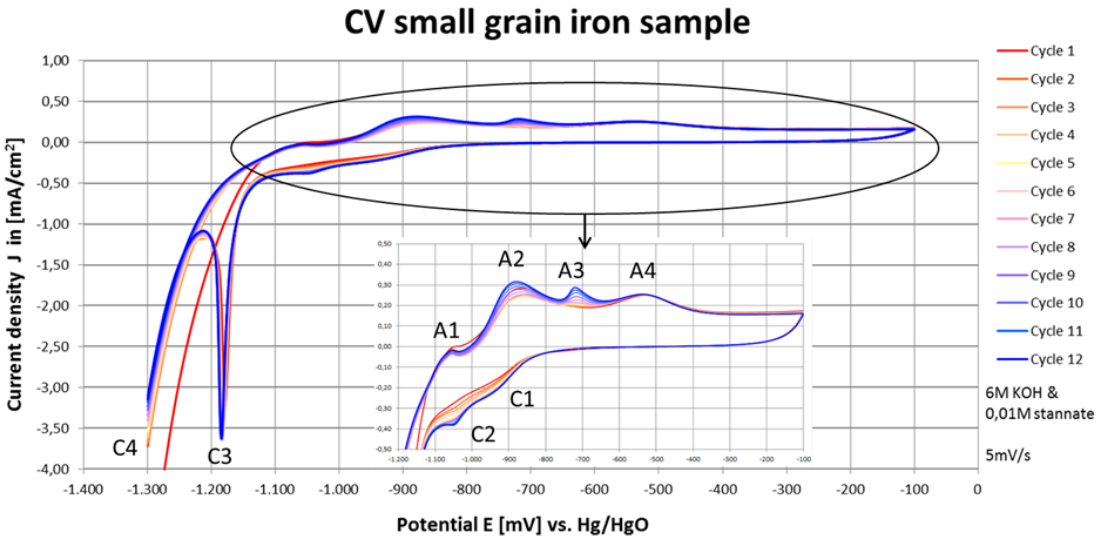

Fig. 36 Cyclic voltammogram response for a tested small grained sample. Serving as an example for the general behaviour which has been observed for all flat specimens. A close-up of more subtle peaks is provided

The peaks observed during cyclic voltammetry tests can be associated to reactions taking place at the iron electrode. Supported by related literature reports and the potential locations (vs. Hg/HgO) of the peaks a link can be made to the most probable redox reaction. The operation range for the electrode potential is always kept between -1,3V to -0,1V vs. Hg/HgO.

In general, mainly two oxidation reactions can be distinguished during CV experiments as described by papers which apply iron electrodes in (strong) alkaline media. These discharge reactions include the oxidation of metallic iron to ferrous hydroxide and the subsequent oxidation of this iron hydroxide to iron oxide and/or oxyhydroxide species. Furthermore, upon charging, the reduction of the formed oxide/hydroxide products takes place as well as the reduction reaction of water to form hydrogen gas. From a “theoretical” point of view, these reactions seem to occur at or close to the following potentials (e.g. see Pourbaix diagram of iron) [5], [21], [26], [32]:

$$Fe + 2OH^- \rightleftarrows Fe(OH)_2 + 2e^- \quad (27) \quad \text{-0,98 V vs. Hg/HgO}$$

$$3Fe(OH)_2 + 2OH^- \rightleftarrows Fe_3O_4 + 4H_2O + 2e^- \quad (28) \quad \text{-0,76 V vs. Hg/HgO}$$

$$Fe(OH)_2 + OH^- \rightleftarrows FeOOH + H_2O + e^- \quad (29) \quad \text{-0,66 V vs. Hg/HgO}$$

$$2H_2O + 2e^- \rightarrow H_2 + 2OH^- \quad (30) \quad \text{-0,93 V vs. Hg/HgO}$$

The first anodic peak experimentally encountered during the forward scan is labelled “A1” and is located around -1,04 V. Besides, a second peak A2 is always seen near -0,87 V. These oxidation peaks are very likely ascribed to the two-step conjunction process, in which OH^- ions are adsorbed by iron. The partial adsorption occurs via the following reaction (A1):

$$Fe + OH^- \rightarrow FeOH_{ads} + e^- \quad (A1) \quad \text{-1,05 V vs. Hg/HgO}$$

Next, the iron hydroxide is formed according to equation (A2):

$$Fe(OH)_{ads} + OH^- \rightarrow Fe(OH)_2 + e^- \qquad \text{(A2)} \quad \text{-0,87 V vs. Hg/HgO}$$

The formation of $Fe(OH)_2$ on its turn, is thought to proceed via the development of intermediate soluble species $HFeO_2^-$ after reaction (A1). The concentration of this species is highly temperature dependant, and the in-between process proceeds through the following path:

$$FeOH_{ads} + 2OH^- \rightleftarrows HFeO_2^- + H_2O + e^- \qquad (31)$$

And

$$HFeO_2^- + H_2O \rightleftarrows Fe(OH)_2 + OH^- \qquad (32)$$

Taking papers with nearly identical conditions in consideration reporting similar peak locations [32] as well as the given electrode potential of equation (27), the first two anodic (A1 and A2) peak reactions observed during CV tests seems to be justified.

The next anodic peak A3 observed at -0,70 V involves the further oxidation of iron hydroxide. The compound which is formed, is an iron oxide namely Fe_3O_4 (magnetite). The corresponding reaction is:

$$3Fe(OH)_2 + 2OH^- \rightarrow Fe_3O_4 + 4H_2O + 2e^- \qquad \text{(A3)} \quad \text{-0,71 V vs. Hg/HgO}$$

Lastly, a peak is consecutively found which can be coupled with a high degree of certainty to the formation of ferric oxyhydroxide:

$$Fe(OH)_2 + OH^- \rightarrow FeOOH + H_2O + e^- \qquad \text{(A4)} \quad \text{-0,52 V vs. Hg/HgO}$$

Often, the A3 and A4 reactions appear to be difficult to differentiate for CV experiments in literature studies. Since often only a singular peak is seen after the oxidation peak of iron. It is assumed that one of these or both reactions occur while only one (large) peak in the CV curve is present. A reason for this (among others) could be the applied scan rate, as the reaction kinetics are affected by this parameter. In this report, a scan rate of $\upsilon = 5$mV/s is employed. During initial trial tests with a 0.5 mV/s sweep rate, A3 and A4 would also not be visible as separate peaks, but rather a single peak.

The clear individual peaks A3 and A4 indicate that these are separate reactions taking place which are most likely due to the formation of Fe_3O_4 and $FeOOH$ as previously described. As these reactions are often mentioned in literature [32], [90]. Figure 37 below shows differences between theoretically expected (dashed line) and experimentally observed (solid line) peak potentials. Due to resistances present in the system the actual potentials where the reactions occur is higher (overpotential).

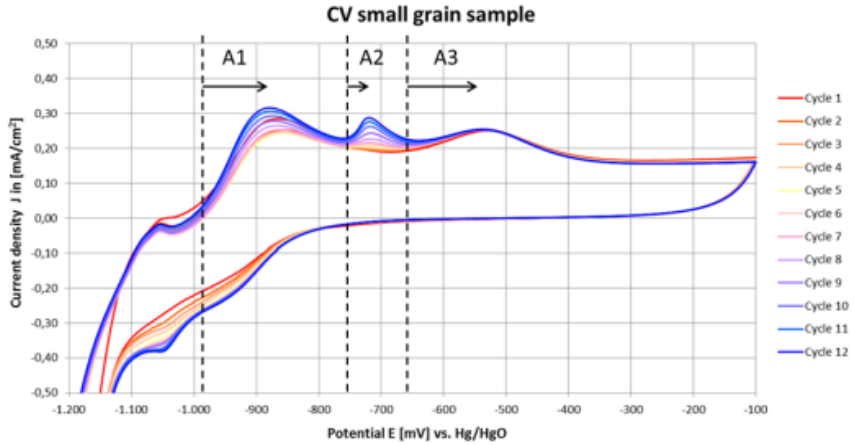

Fig. 37 Cyclic voltammogram response for a tested small grained sample. Dashed lines indicate the expected potential for peaks to occur (in strong alkaline solution; “theoretically”). Arrows indicate the potential at which the supposed reaction is observed during experiments

After the reversion of the CV curve at -0,1V vs. Hg/HgO, reduction processes start to occur. In total, 4 cathodic “peaks” can be recognized. Some of these are not always (very well) defined and can therefore not strictly be called a peak. The observed “deviations” in the graph can be better described as a bump or inclination in the curve. However, during the course of this report, the terms bump and peak will be used interchangeably for convenience’s sake. The cathodic peaks are associated to the reduction reactions of the formed oxide/hydroxide products during the anodic part of the cycle and the evolution of hydrogen gas.

The first cathodic peak C1, that seems to occur is a bump located at approximately -0,92V vs. Hg/HgO in the tests. The most straight forward reaction, which is responsible for this, would be the reduction of $FeOOH$. Since this species was last oxidized, it is reasonable to assume that this is the earliest product to be reduced.

$$FeOOH + H_2O + e^- \rightarrow Fe(OH)_2 + OH^- \qquad \text{(C1)} \quad \text{-0,91V vs. Hg/HgO}$$

Similarly, the next peak C2 refers to the opposite reaction of peak A3, which means the reduction of Fe_3O_4:

$$Fe_3O_4 + 4H_2O + 2e^- \rightarrow 3Fe(OH)_2 + 2OH^- \qquad \text{(C2)} \quad \text{-1,02V vs. Hg/HgO}$$

The C3 peak can be observed in Figure (36), as it is orders of magnitude larger compared to C2 and C1. This can be clarified as follows; the reduction of $Fe(OH)_2$ to iron appears to happen in singular single reaction, as opposed to the two oxidations A1 and A2. On top of that, the HER has already set in when this C3 reaction takes place. Thus, the C3 reaction is partially concealed by the HER and lies at much lower current density. It is however difficult to pinpoint the exact moment where the HER has initiated. Based on the CV graphs, it looks like it happened just before the reduction of iron hydroxide at approximately -1,10V vs. Hg/HgO. The reaction corresponding to C3 is:

$$Fe(OH)_2 + 2e^- \rightarrow Fe + 2OH^- \qquad \text{(C3)} \quad \text{-1,16V vs. Hg/HgO}$$

As said, the HER has started and continues to take place as the potential becomes more negative. The increase in (negative) current density progresses until the maximum value is reached at the point -1,3V vs. Hg/HgO (see Figure (36)). So for this process a true peak is also not found. It has been chosen to signify this potential as the peak location for the HER,

since it is the turnover point for cycles and the (absolute) maximum value reached. The according reaction is:

$2H_2O + 2e^- \rightarrow H_2 + 2OH^-$ (C4) -1,30V vs. Hg/HgO

Thus to summarize the following reactions are identified with their according potential locations. All potentials are referred versus Hg/HgO reference electrode.

A1 (-1,04V): $Fe + OH^- \rightarrow FeOH_{ads} + e^-$

A2 (-0,87V): $Fe(OH)_{ads} + OH^- \rightarrow Fe(OH)_2 + e^-$

A3 (-0,71V): $3Fe(OH)_2 + 2OH^- \rightarrow Fe_3O_4 + 4H_2O + 2e^-$

A4 (-0,52V): $Fe(OH)_2 + OH^- \rightarrow FeOOH + H_2O + e^-$

C1 (-0,91V): $FeOOH + H_2O + e^- \rightarrow Fe(OH)_2 + OH^-$

C2 (-1,02V): $Fe_3O_4 + 4H_2O + 2e^- \rightarrow 3Fe(OH)_2 + 2OH^-$

C3 (-1,16V): $Fe(OH)_2 + 2e^- \rightarrow Fe + 2OH^-$

C4 (-1,30V): $2H_2O + 2e^- \rightarrow H_2 + 2OH^-$

The convention in the Figure 36 is applied throughout the results and discussion section. Hereby, the first peak observed during oxidation is called “A1”, the second peak “A2” etc. Similarly, when the reverse scan begins the first peak encountered is “C1”. Moreover, A3 for example is always equivalent to reaction it has been linked.

In order to obtain more quantitative information of the processes, certain features of the CV curves are more closely analysed. The peak height ratio of A2/A3 and A2/A4 have been computed, the surface area of the C3 peak is approximated and the HER slope is determine at the end of cycles. In the next section, the relevance of understanding these attributes in relation to the battery performance is discussed.

3.2.2. Peak analysis

The oxidation and reduction peaks observed during CV experiments can provide key information of the processes taking place in the electrochemical cell [140]. The anodic reactions in the previous section are linked to formation of iron oxide/hydroxide species. Beside the initial redox product $Fe(OH)_2$; Fe_3O_4 and $FeOOH$ are formed and contribute to the generation of a thin layer which is electronically insulating. In particular the conversion of $Fe(OH)_2$ to magnetite and ferric oxyhydroxide is undesirable. Since, the latter are $Fe(III)$-species, which appear to be more stable and are, as a result, prone to incomplete reduction [5]. Because of this, the performance of the iron electrode is impaired as surface coverage of these molecules act as barrier for electron transfer, preventing electrochemical activity of the anode. Thus, the formation of these oxide/hydroxide compounds is ideally avoided (or minimized) as long as possible.

By means of calculation of the peak current height ratio over cycling, the development of the oxidation peaks A2, A3 and A4 are compared relative to each other for all samples. An example in shown in Figure 38, which clearly demonstrates an increase and decrease of peaks over repeated cycling. The evolution of these peaks over cycling could be a useful tool to reveal how much of formed iron hydroxide is converted to highly stable (almost irreversible) Fe_3O_4 and $FeOOH$. The ratios are defined as follows: peak height of A2/A3 and A2/A4 whereby the values of the current density are read off for a particular cycle. In Figure 38, this is shown for a cold rolled sample in the 12th cycle. The values are read-off at the peak locations as illustrated in Figure 38.

In general, large and increasing ratio values over cycling are preferred as these imply relatively much conversion of iron to $Fe(OH)_2$ (A2) compared to the follow up reactions of $Fe(OH)_2$ to Fe_3O_4 (A3) and $FeOOH$ (A4).

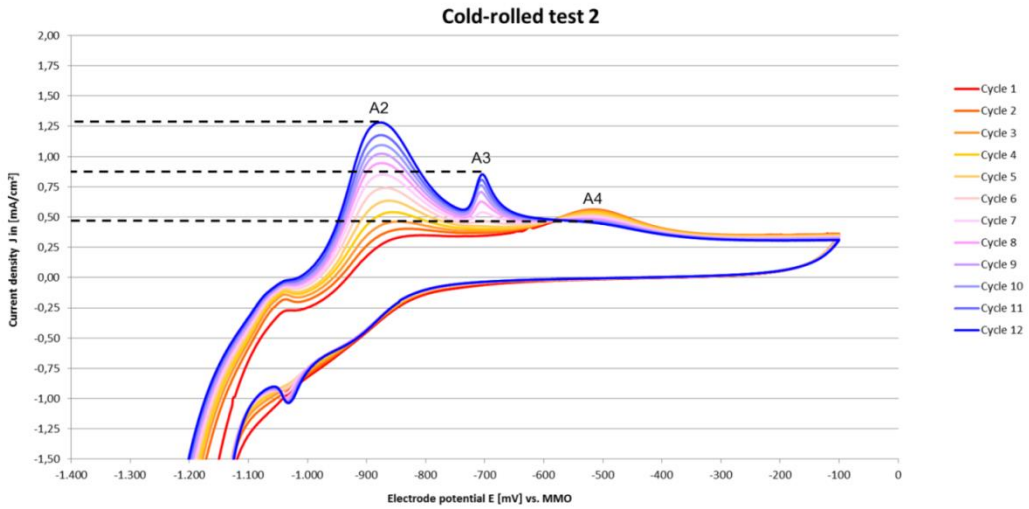

Fig. 38 A cold-rolled CV test which demonstrates the growth and decline of anodic peaks A2, A3 and A4.

Furthermore, the surface area of the third reduction peak is integrated. The C3 peak is related to the cathodic reaction:

$$Fe(OH)_2 + 2e^- \rightarrow Fe + 2OH^- \qquad \text{(C3)}$$

Given the very well-defined shape and large intensity of this peak, the method of calculating the surface area makes it highly suitable and accurate as opposed to all other peaks. Numerical integration is applied using the Riemann sum to approximate the area under the peak. An appropriate baseline is chosen as reference which sets the boundaries for the interval of integration and encloses the region of interest (see Figure 39). The area under this part of curve is equal to the charge in Coulomb. The magnitude of this area (amount of charge) can be linked to the quantity of reversion of $Fe(OH)_2$ to Fe. By convention, it is chosen to express this as a positive value and apply the unit of Coulomb per square meter [C/m^2].

Consisting of a (finite) sum of rectangles, the unit obtained after integration is $[\frac{mA \cdot mV}{cm^2}]$. Using the identity $1\,A = 1\,C/s$, and substituting this in the obtained unit, where the “m” (milli) unit

prefix has been converted, one gets $[\frac{C \cdot V}{s \cdot cm^2}]$. Finally, the latter unit is divided by the scan rate (5 mV/s), while cm^2 is converted to m^2. Following this procedure, the unit [C/m^2] is obtained.

The relevance of knowing the peak area value, is that it can be associated to the quantity of iron hydroxide reversion. This is closely related to the reversibility of formed oxide/hydroxide species, formed during the oxidation process. Besides the magnitude, it is particularly interesting to see how it develops over multiple cycles. For example, a significant decrease of this peak area over cycling could point towards less efficient conversion stable oxide/hydroxide species, which can result in a built-up of insulating compounds which enable coverage of the electrode surface.

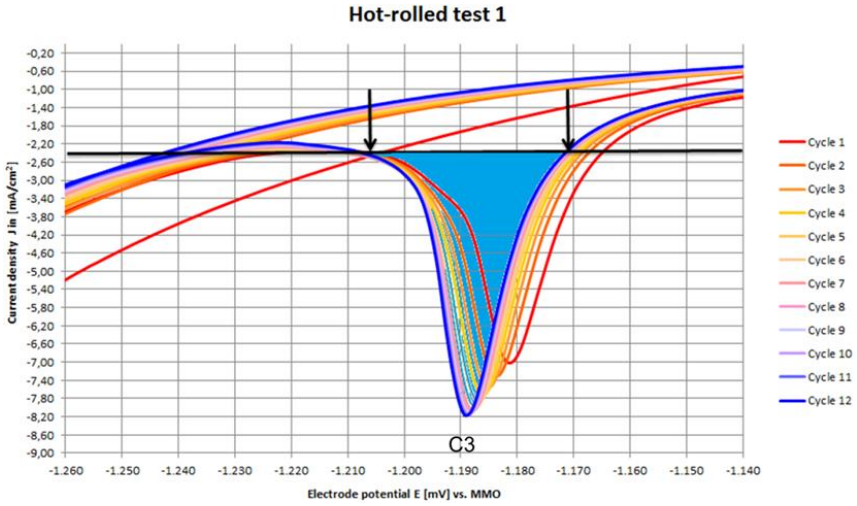

Fig. 39 A hot-rolled CV test which shows the surface area of the C3 peak in the 12th cycles (shaded blue).

The reduction of $Fe(OH)_2$, which is driven by a relatively high overpotential during charging in the iron-air battery, competes with the HER according to reaction C4. The anode electrode performance decreases because of this phenomena. Firstly, the coulombic efficiency of the cell significantly decreases as some of the applied charge is redirected into this unintentional side reaction. Secondly, extensive hydrogen formation can result in a pronounced loss of water in the electrolyte, which could cause the battery to dry-up and fail eventually.

The C4 peak is investigated to elucidate the HER intensity for the different microstructures. The gradient at the end of the backwards scan can be directly related to the severity of hydrogen gas evolution, as this marks the onset and progression, the C4 peak has made. A steep slope suggests that the HER has advanced to more negative current density values, and thus formed a larger peak. The slope is calculated by taking the linear gradient of the last 50 mV of cycles from -1250 mV to -1300 mV. The difference in current density is divided by the change in potential (= 50 mV). At this region, the CV curve has approximately reached a linear section. Using a larger range would make the assumption of a linear gradient less accurate as the CV is becomes horizontal at potentials higher than -1250 mV. A smaller range is more susceptible to errors.

It could be argued that simply the current density value at -1,30V could be read-off and utilized as indication for the HER. Since more negative values of the current density of a cycle implies a more intense hydrogen gas production. However, it is observed that during some CV tests, the curves as a whole are translated in vertical direction (upwards or downwards) compared to other CV experiments. This influences the value of the C4 peak at -1,30V. Thus, determining the HER magnitude via a linear slope approximation is a more independent method.

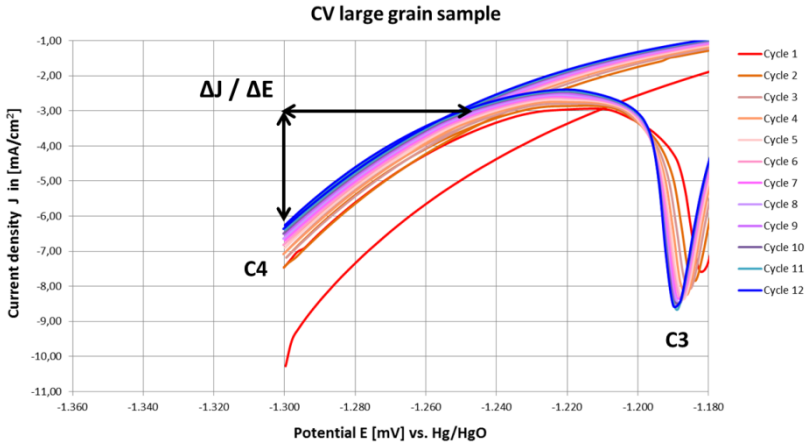

Fig. 40 A CV test with a large grained iron samples showing the slope at the backwards scan at the C4 peak, related to the intensity of the HER.

3.3. Electrochemical results

3.3.1. Electrochemical results grain size

3.3.1.1. Chronoamperometry

Chronoamperometric measurements are initial started as the first electrochemical test. Herein, the current density [mA/cm^2] is set out to the time [sec]. The purpose of this, is to let the system stabilize at starting potential (-1,3V) for CV cycling while also reverting most iron oxide/hydroxide species present at the iron surface to Fe. As a pre-conditioning step, CA is performed at -1,3V vs. Hg/HgO and kept for 120 seconds (cathodic polarization), to ensure all specimens have the same surface conditions at the start of the CV test. In Figure 41 below, the CA curves for the annealed hot-rolled anodes are shown.

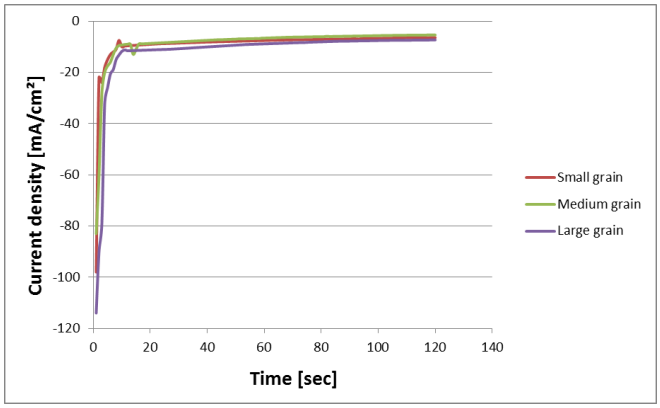

Fig. 41 Typical chronoamperometric response of the different grained samples at -1.3V vs. MMO in 6M KOH and 0.01M sodium stannate for 2 minutes.

3.3.1.2. cyclic voltammetry

Next the Cyclic voltammetry technique would follow. The CV graphs for the samples are shown in Figure 42, which showcase similarities in peaks and overall structure.

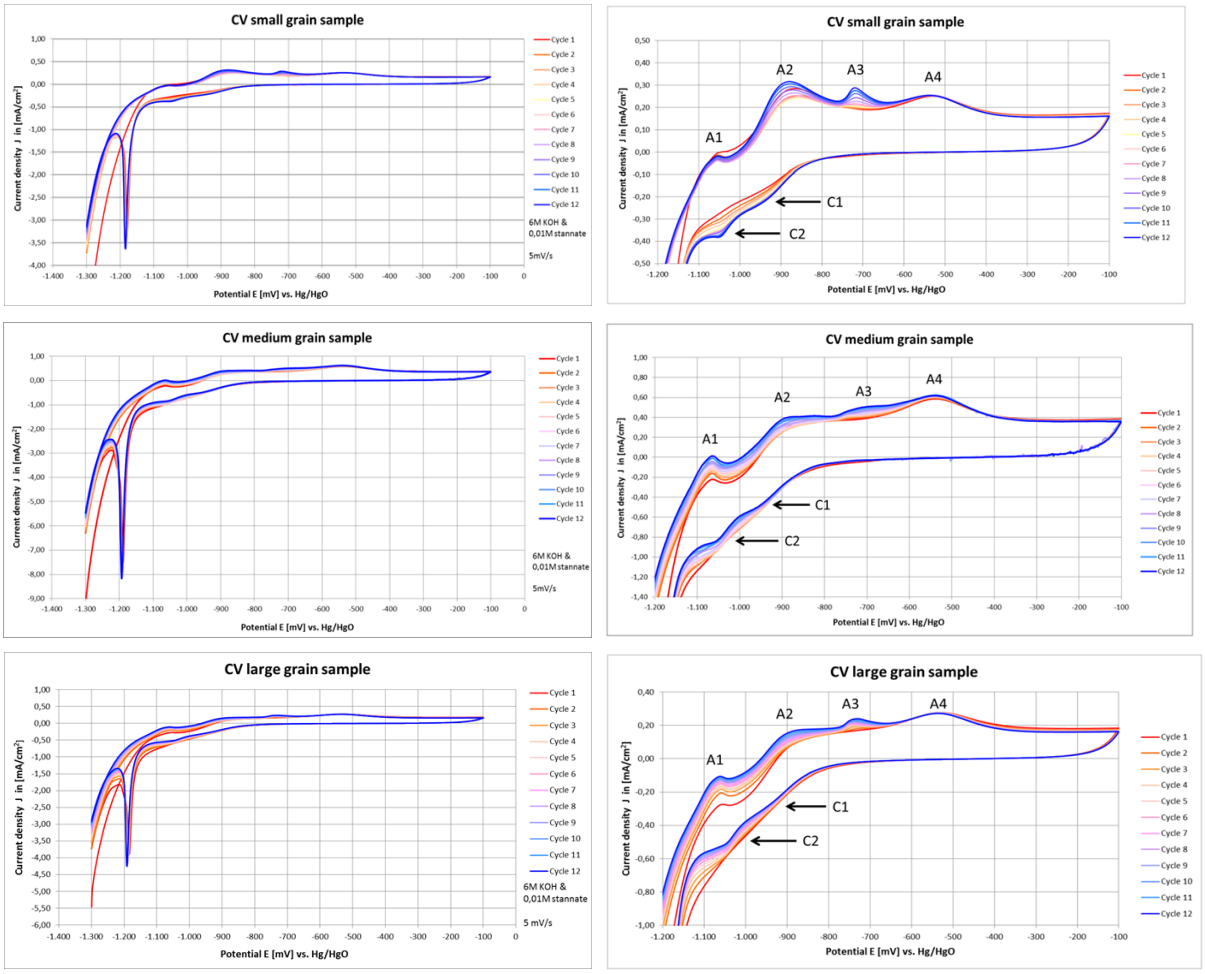

Fig. 42 Behaviour of various grained iron electrodes for 12 cycles in 6M KOH and 0.01M sodium stannate at a 5 mV/s scan rate.

Considering the first anodic peak A1, it can be observed that the coarse grained samples increase in current density with cycles while the small grain anode does show a constant peak height current. This oxidation reaction is linked to the initial process in which OH^- anions are adsorbed by iron to form $FeOH_{ads}$. Therefore, the extent of this electrochemical reaction increases, resulting in higher concentrations of $FeOH_{ads}$ for the medium and large grain specimens over cycles compared to the small grained sample. Subsequently, it is seen that the grain refined sample has a more pronounced A2 peak as opposed to the larger grain electrodes. It could indicate that the dominant reaction for the small grain sample is rather the direct oxidation of iron to iron hydroxide while the other specimens rely more on the intermediate oxidation reaction step.

The next oxidation reaction is seen at peak A3, which corresponds to the reaction of $Fe(OH)_2$ to Fe_3O_4. For all samples, it can be observed that in the first cycle, no clear A3 peak is visible. Meanwhile, as the CV continues with cycling, a gradual increase in intensity of

these peaks during 12 cycles arises. Particularly, the small grain sample shows an obvious increment of this peak. The equivalent cathodic redox reaction at the C2 peak is seen to decrease in magnitude for the coarse grained samples while the current density rises for the small grain sample with cycles. This demonstrates the accumulation of an oxide layer composed of Fe_3O_4 for especially the medium and larger grain samples, as the reversibility of this compound is lower for these samples. Surface coverage of these oxides deactivates the electrochemical reactivity of the iron anode, impeding the capacity of the anode.
The last anodic reaction (A4), in which $FeOOH$ is formed from iron hydroxide, is seen to be practically constant over cycles for all samples. The corresponding reduction of $FeOOH$, which is related to C1, shows differences among the anodes. Comparing the first with the last cycle, the magnitude of the C1 current density increases for the small grained sample. On the other the same cathodic reaction seems to stay stable or decrease slightly for the larger grained samples. This implies that reversibility of $FeOOH$ at the small grain electrode is better as cycling progresses compared to its coarser grained electrode counterparts.

3.3.1.3. Peak height ratios

The height (current density) of three anodic peaks are determined and calculated as fraction of each other, as seen in Figure 43. The oxidation peaks A2, A3 and A4 are considered, as the corresponding reactions of these peaks mark the formation of $Fe(OH)_2$, Fe_3O_4 and $FeOOH$, respectively. The oxidation of iron to iron hydroxide is the most important reaction, as this initial process provides the electrons, which flow through an external circuit, for functional purposes (in an iron-air battery). The subsequent reactions (A3 and A4) involve the oxidation of $Fe(OH)_2$ to Fe_3O_4 and $FeOOH$. Although also providing electrons, the formation of the latter compounds is ideally avoided or minimal. Since these $Fe(III)-$ species appear to be more stable (than $Fe(OH)_2$) and are, thus, prone to incomplete reduction [5]. In the iron-air battery, these stable molecules are therefore hindering the charging and discharging process, since they cover the anode surface with their inherent denser film. This coverage deactivates (locally) the activity of the anode for oxidation of iron in the next cycles. In this context, the ratios A2/A3 and A2/A4 are calculated, as these values provide an indication of the relative amount of iron hydroxide formed, which is further oxidized to the previous mentioned more stable oxide/hydroxide products.
Overall, the largest fraction values of A2/A3 in cycles 1, 6, and 12 are seen for the small grain sample. Having a value of 1.25 in the first cycle and 1.06 at the 12th cycle. While for the medium and large grained samples, the ratios are lower. If the 12th cycle is considered, the A2/A3 ratio of the small grain sample is about 20% higher compared to other samples. This would mean that formation of Fe_3O_4 is relatively small compared to the formation of $Fe(OH)_2$. Therefore, it looks like a trend can be observed with grain size. However, when taking the CV graphs into account, the reason for large A2/A3 values could be explained by the more preferred immediately oxidation of Fe into $Fe(OH)_2$ for the small grain anode. This results in a large current for the A2 reaction while, the larger grained samples are more reliant on the intermediate step oxidation process in which electrons are released consecutively.
Moreover, the A2/A3 fraction for the small and medium grain anodes in the 12th cycle declines compared to the initial cycle, implying that these anodes tend to perform worse over cycling as relatively more iron oxides are formed. On the other hand, the coarse grained sample shows the opposite trend. This could suggest that grain refinement facilitates an initial higher reactivity of the first oxidation reaction of iron in alkaline solution compared the larger grained anodes. The link to the effect of grain size can be explained by taking the work

of Ralston et al. [134], [135] in consideration. They suggest that because of the inherent higher energy and chemical activity of grain boundaries, impact the oxidation processes. Since a large grain boundary density raises the reactivity of the surface through increased diffusion and electron activity [136]. The pronounced A2 peak in the CV graph for the small grain sample could be an indication of the increased reactivity as this peak is not as clearly seen for the larger grained specimens. Experiments in which an increased number of CV cycles are applied, could be performed to check how these fractions develop further.

The peaks ratios of A2/A4 demonstrates similarities with the progression of the A2/A3 fractions over cycles. First a decrease is present from cycle 1 to 6 followed by increase from the 6th to 12th cycle, for the small and medium grain electrodes. The largest A2/A4 values are seen for the grain refined specimen compared to the larger grained samples. This could imply that the grain refinement is beneficial as a lower fraction of oxides/hydroxides are formed. However, the large grain anode showcases a significant rise although starting at a low ratio values\. This indicates that in the first cycles relatively much $FeOOH$ is formed, and in later cycles less.

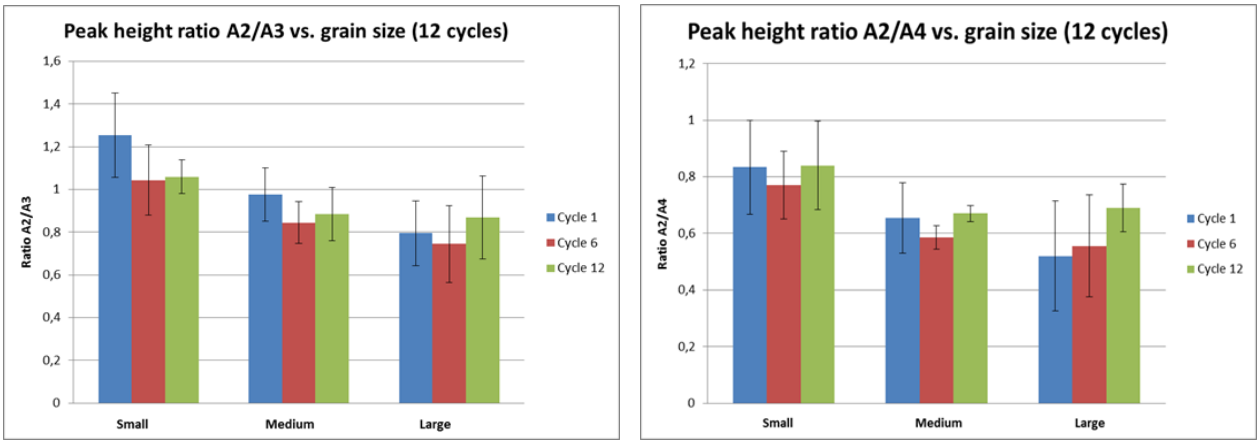

Fig. 43 Column graphs showing the progress of the A2/A3 and A2/A4 peak height ratios for the various grain sized samples for cycle 1,6 and 12.

3.3.1.4. Peak area C3

Next, the calculated surface area of the C3 peak is reviewed. Relating to the reaction in which $Fe(OH)_2$ is reduced to metallic iron, the area of the this peak could hint to towards a better or worse reversibility of the iron hydroxide species among samples. In the reverse cathodic cycle, $Fe(OH)_2$ can be formed via the reaction according to C1 and C2. Ideally, the formation of iron hydroxide is attributed to the reduction of $FeOOH$. Since the presence of the cathodic C2 peak would indicate that Fe_3O_4 (the most stable and insulating product) has been produced in the first place. Looking at the CV results in Figure 42, it can be observed that the C1 and C2 peak current densities increase and become more distinguishable as cycling continues for the small grain electrode. On the contrary, the medium and large grain samples show that these peak currents tend to decrease with cycling. Thus, the contribution of the C3 peak area is largely attributed the C1 and C2 cathodic reactions for the small grain specimen, while this is not the case for the larger grained anodes. The peak surface areas are nearly constant over 12 cycles and approximately similar (± 60 C/m^2) for all electrodes. Given the result of the CV and the calculated peak area of C3 in Figure 44, it suggests that amount of Fe_3O_4 and $FeOOH$ formed, in absolute sense, is larger for the small grain sample.

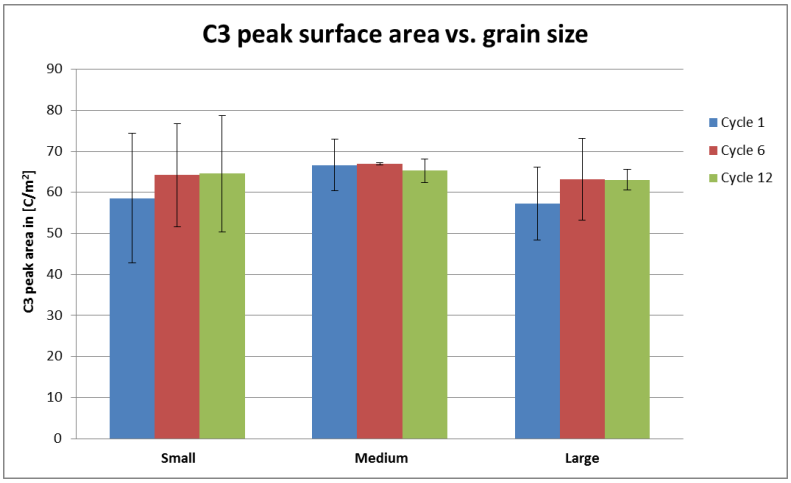

Fig. 44 Column graphs showing the progress of the C3 peak area of the various grain sized samples for cycle 1,6 and 12.

3.3.1.5. HER intensity

Finally, the curve gradients at the end of cycle 1,6 and 12 are considered for the small and large grain iron samples in Figure 45. This can be linked to the intensity of hydrogen gas evolution at the end of the reverse cathodic scan. Evolution of hydrogen gas is a parasitic side reaction which lowers the coulombic efficiency in iron-air batteries due to irreversible loss of electrons in every cycle. Ideally, solely the reduction $Fe(OH)_2$ takes place to recharge the battery. Data from tests with the medium grain specimen was heavily influenced by outliers caused by errors occurring with the EC-lab software. Because of that, these results have been omitted. The results indicate that the HER slope gradually decreases after initial cycling for both anodes. Moreover, the intensity for both materials is seen to be quite similar, being around 450 A/(V·cm^2) in the first cycle, dropping to 400 A/(V·cm^2) at the 12th cycle. Notably, the gradient decline is larger for the small grain sample from the first to the last

cycle. A decrease of nearly 15% is seen for the small grain electrode, while only a reduction of 7% is observed for the anode composed of larger grains. This implies that the grain refined anode becomes more efficient as cycling proceeds.

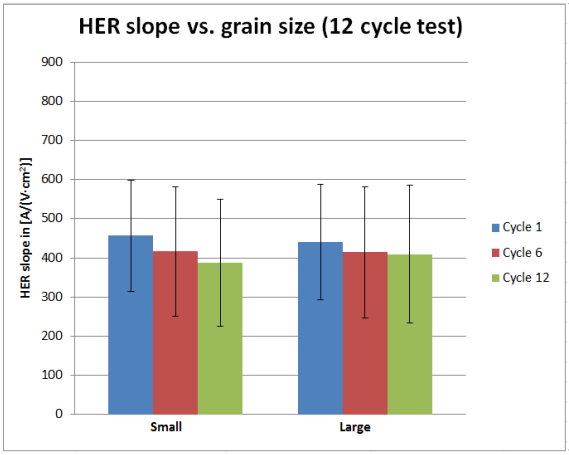

Fig. 45 Column graphs showing the progress of the HER intensity of the various grain sized samples for cycle 1,6 and 12.

3.3.1.6. Impedance tests

After the CV tests have completed 12 and one half cycle, CA is again utilized, now at potential of -0,1V vs. Hg/HgO for five minutes to ensure the samples have the same surface conditions at the start of EIS experiment. The extra half cycle performed is the forward scan in which the iron anode is subjected to all anodic peaks, as discussed earlier. Therefore, a layer of iron oxide/hydroxide compounds is expected to be present on the electrode surface. A frequency range of 10 mHz to 100 kHz is applied. The results are presented by Bode plots and Nyquist plots in Figure 46. At a low frequency of 10 mHz, it is seen that the average impedance values are 35.5 kΩ, 42.7 kΩ and 33.1 kΩ for the small, medium and large sample, respectively. These resistances at low frequencies can mostly be ascribed to the presence of iron oxide compound Fe_3O_4 which typically provide a larger resistances for charge transfer in comparison to most iron hydroxide molecules [125], [139]. This is due to more crystalline lattice structure of oxides which forms a less defective structure, which results in higher resistances observed. The highest resistance, which is seen for the medium grain sized electrode could therefore indicate that here, relatively more unwanted Fe_3O_4 is formed. A justification which supports this presumption with the cyclic voltammetry results can unfortunately not be discovered. Since CV tests of the medium grain electrode do not clearly indicate a more significant rise of oxidation peak A3 compared to the other anodes.

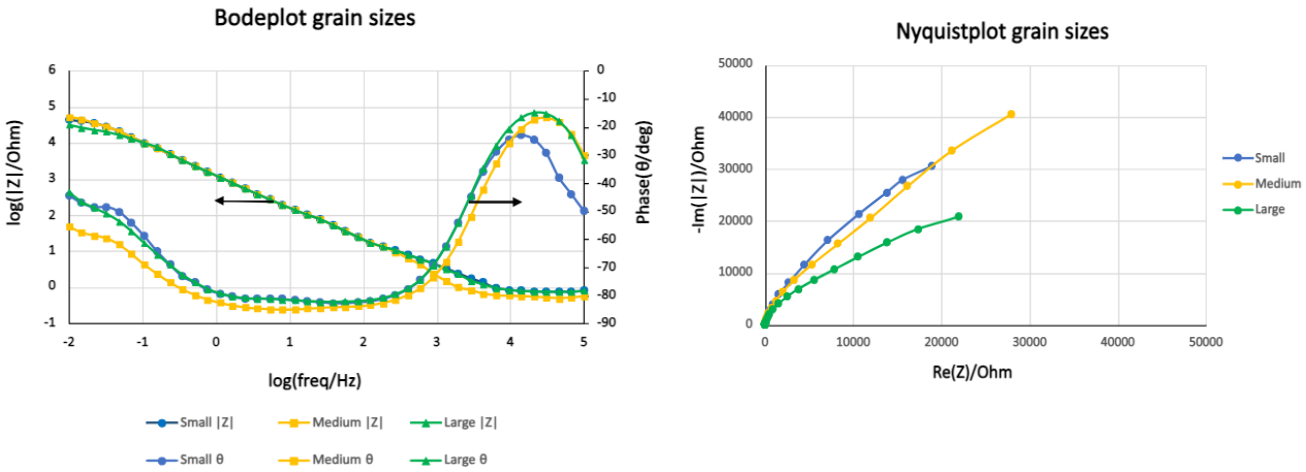

Fig. 46 Bode plot and Nyquist plot for samples small, medium and large grain sample with frequency range 10^{5} to 10^{-2} Hz.

	Log(|Z|/Ohm) at 10 mHz	|Z|/Ohm at 10 mHz
Small	4.55 ± 0.22	$3.55\times10^{4\pm0.22}$
Medium	4.63 ± 0.19	$4.27\times10^{4\pm0.19}$
Large	4.52 ± 0.17	$3.31\times10^{4\pm0.17}$

Table 9) Calculated average impedance grain size anodes at 10 mHz

A good fit was difficult to acquire for the samples. The most suitable fit that could be obtained with Zfit, resulted in the circuit seen in Figure 47. This equivalent circuit is comparable to other applied circuits in literature to represent a corroding metal in a (corrosive) solution where a layer of piled up corrosion products is formed [125] and to mimic the corrosion of metal with a defective/porous coating [126]. Therefore, the proposed model in Figure 47 is assumed to be correct, given the similarities to these systems.

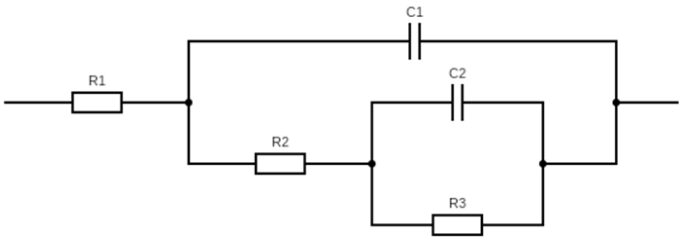

Fig. 47 Proposed equivalent circuit to interpret the EIS data

The circuit in the Figure 47 above consist of two time constants wherein R1 represents the ohmic resistance of the electrolyte, R2 the resistance of the oxide/hydroxide layer, C1 the oxide/hydroxide layer film capacitance, R3 the polarization resistance at the iron/solution interface and C2 the double layer capacitance at iron/solution interface. Most likely, the capacitor components C1 and C2 in the given equivalent circuit are in reality “imperfect” capacitors, which could be better modelled by constant phase elements (CPE). Proper fitting of data could point out if this is the case.

3.4. Hot/cold rolled results

3.4.1. Electrochemical examination

3.4.1.1. chronoamperometry

CA measurements are initial started as the first electrochemical test. The CA is performed at -1,3V vs. Hg/HgO and kept for 120 seconds (cathodic polarization). After this period, the current density has largely stabilized at a value around of J = -5 mA/cm^2 . Overall the rolled samples did exhibit similar behaviour at this stage of the experiment as observed in Figure 48.

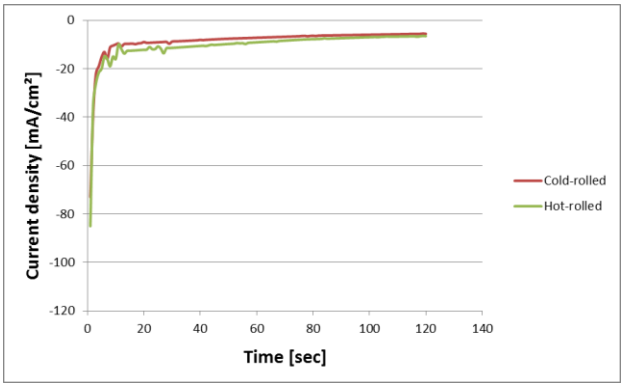

Fig. 48 Typical chronoamperometric response of the hot and cold rolled samples at -1.3V vs. MMO in 6M KOH and 0.01M sodium stannate for 2 minutes.

3.4.1.2. cyclic voltammetry

Sequentially, cyclic voltammetry technique follow the CA. The CV graphs for the hot-rolled and cold-rolled samples are shown in Figure 49, which showcase similarities in peaks and overall structure.

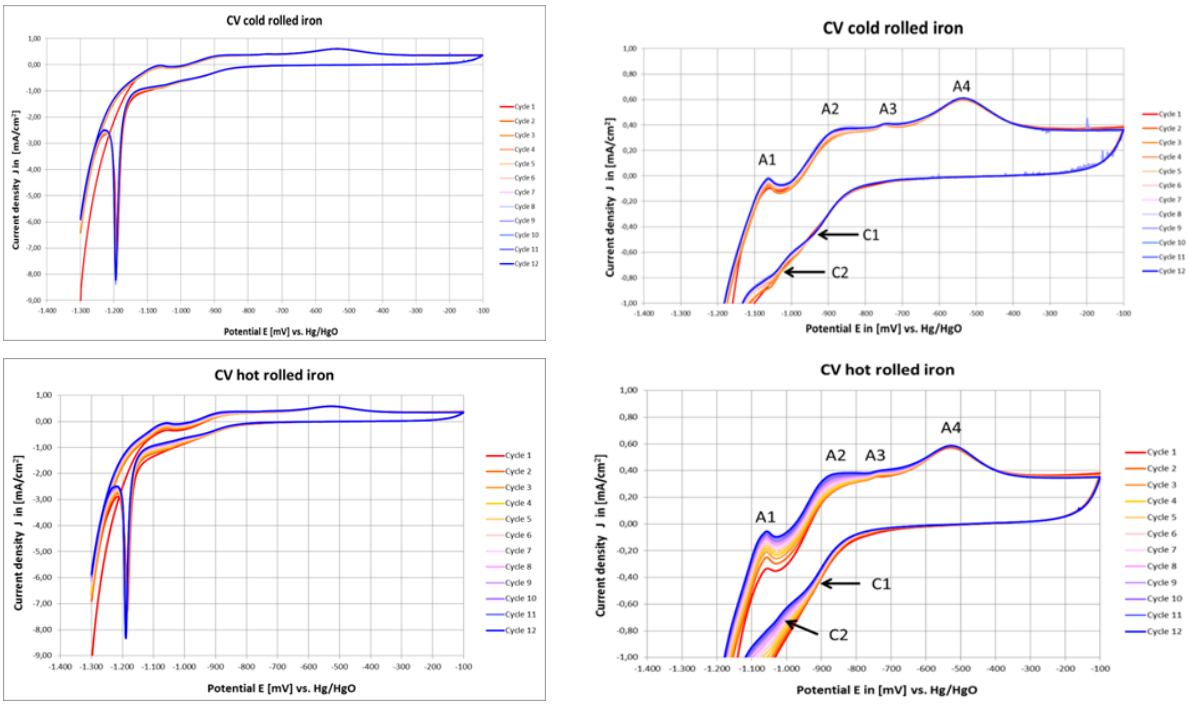

Fig. 49 Behaviour of rolled iron electrodes for 12 cycles in 6M KOH and 0.01M sodium stannate at a 5 mV/s scan rate.

Considering the first oxidation peak A1, it can be seen the hot rolled sample showcases a significant peak increase over cycling, which is to lesser extent observed for the cold rolled electrode. This could indicate, as previously described in the grain size section, that the dominant reaction for the hot rolled anode relies (increasing) more on the intermediate oxidation reaction step compared to cold rolled sample. Remarkably, the A3 and A4 peaks in the CV of the cold rolled sample remain practically constant over cycling while also be suppressed effectively over 12 cycles. This demonstrates that the formation of unfavourable especially Fe_3O_4 (and also $FeOOH$) compounds remains under control, a feature which was not seen for the heat treated hot rolled anodes. For the as-received hot rolled sample, a minimal, but noticeable increase of the A3 peak current can be seen as well as a constant A4 anodic peak. In the reverse scan, shows a constant peak for C1 current while a slightly decrease of the C2 peak is seen for the cold rolled sample. The hot rolled electrode exhibits a more pronounced decrease for both these reduction reaction peaks. An accumulation of oxide/hydroxides layer is therefore expected to occur to a greater extent for the hot rolled specimen. Meanwhile, the cold rolled sample displays a better reversibility of the formed oxides/hydroxides.

3.4.1.3. Peak height ratios

The A2/A3 peak height fractions (Figure 50) of the cold rolled electrode shows that, on average, an increasing trend is observed, suggesting that over cycling relatively less iron oxides are formed. On the other hand, the hot rolled sample illustrates a more or less consistent A2/A3 ratio at a value around 0.9. Similarly for the A2/A4 a similar course recognized. Because of a constant C4 peak height during all experiments, the rise in A2/A4 for the cold rolled electrode indicates that this can be ascribed to an increase of the A2 oxidation reaction which is beneficial. The results of the hot rolled specimen shows that this fraction remains almost stable. Experiments where more cycles are executed as well as more repeated tests should confirm if more clear differences are present among these materials (or not).

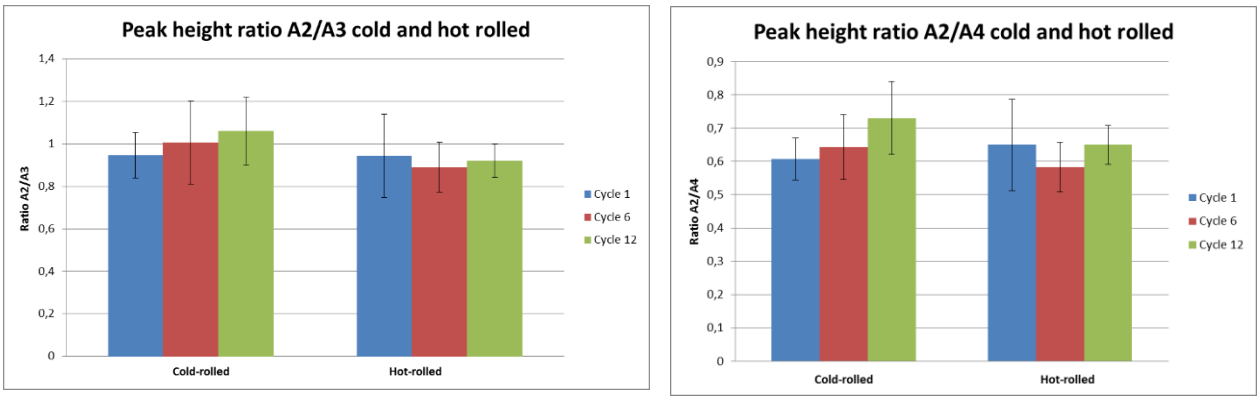

Fig. 50 Column graphs showing the progress of the A2/A3 and A2/A4 peak height ratios for rolled iron samples for cycle 1,6 and 12.

The oxidation peak height ratios obtained, present a marginal improvement in performance exists for the cold-rolled sample compared to the hot-rolled counterpart. This is primarily based on the growing peak ratios tendency of A2/A3 and A2/A4 for the cold-rolled iron over 12 cycles.

3.4.1.4. Peak area C3

Subsequently, an assessment is conducted on the computed surface area of the C3 peak. Considering the outcomes depicted in the column chart (Figure 51) presented below, it becomes evident that variations in rolled materials do not appear to significantly affect this process during cycling. The peak area values uniformly cluster around 100 C/m², and the error bars consistently overlap to a considerable extent. However, when comparing the charge densities with the electrodes in the grain size section, the values are significantly larger. For the anodes in which the grain size is varied, the charge density is nearly 40% lower (around 60 C/m²). The C3 peak area, which is linked to the conversion of $Fe(OH)_2$ to Fe, implies that iron oxide/hydroxide species are more reversible. Since $Fe(OH)_2$ is formed from the reduction reactions according to C1 and C2.

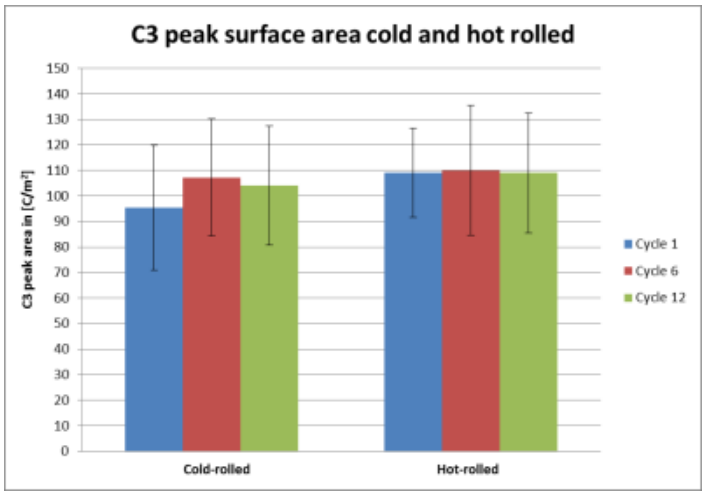

Fig. 51 Column graphs showing the progress of the C3 peak area of the rolled iron samples for cycle 1,6 and 12.

3.4.1.5. HER intensity

The HER slopes of the C3 peak showcase a descending pattern of the gradient over 12 cycles, in Figure 52 for both cold and hot rolled. Although slightly affected by an outlier, the HER intensity seems around 15% lower for the cold rolled sample compared to its hot rolled counterpart. Since a small variation of crystallographic orientation is found between the cold and hot rolled iron, the HER kinetics might be affected by this microstructural factor. Limited relevant studies are available in which this has been extensively investigated. A few papers which did investigate the effect of crystallographic orientation on the HER kinetics for pure metals like Au [142] and Pt [141] show contrasting findings. For a gold (Au) single crystal in an acidic environment, the HER kinetics are described to follow a cathodic activity sequence of (111) > (100) > (110). On the other hand, a platinum low-index single-crystal shows an orientation sequence (110) > (001) > (111) for the HER kinetics in alkaline solution. Reasons that might play a role are hydrogen adsorption free energy, the work function of the surface and hydrogen coverage on the surface [142], [143].

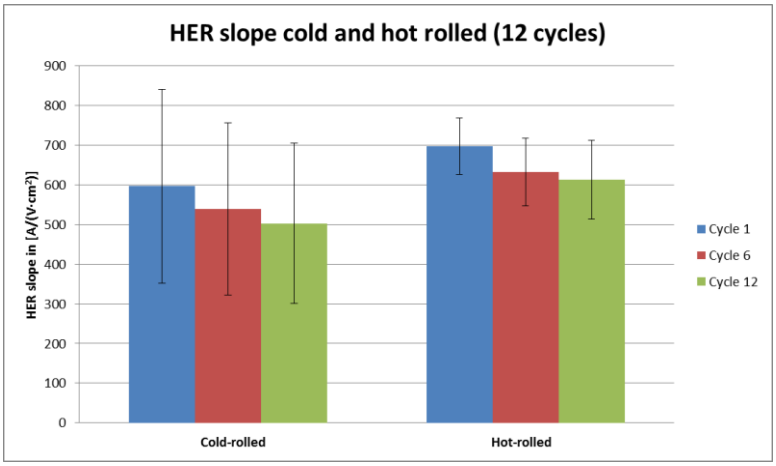

Fig. 52 Column graphs showing the progress of the HER intensity of rolled iron samples for cycle 1,6 and 12.

3.4.1.6. Impedance tests

The electrochemical impedance tests, represented through Bode plots and Nyquist plots in Figure 53, align mostly with the findings from cyclic voltammetry. Specifically, there is a minimal difference between hot-rolled and cold-rolled iron regarding the amount of oxide compounds formed. The resistance for the systems with cold rolled and hot rolled iron specimens is practically similar, with the cold rolled being slightly lower on average. When these results are put next EIS results from the samples from the grain size section, a significant lower impedance is observed. This is in correspondence with the CV tests for the rolled samples, where clearly less formation of Fe_3O_4 is seen. Therefore, grain refinement could be a factor influencing the formation of the iron oxides. Producing pure iron anodes with even smaller grains and similar testing techniques should indicate if there is a correlation with grain size.

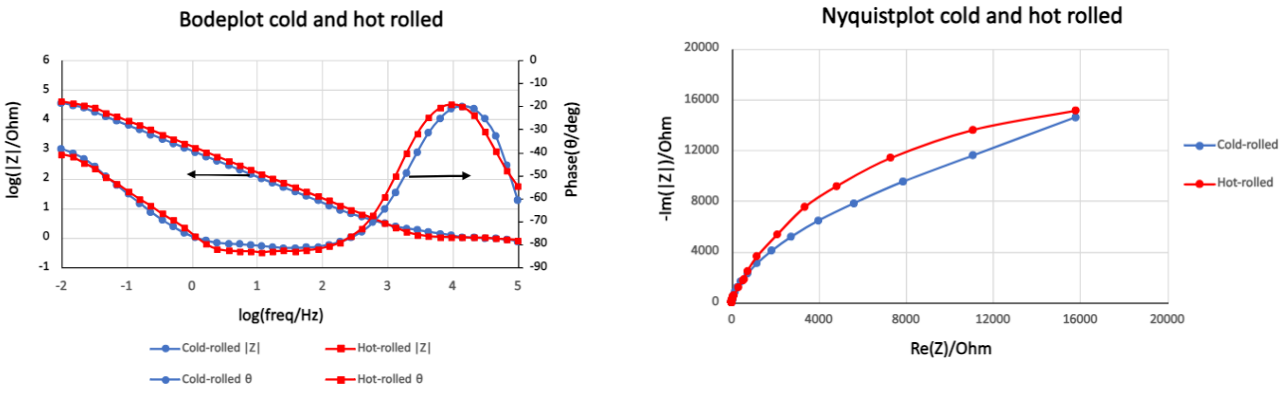

Fig. 53 Bode plot and Nyquist plot for samples hot-rolled and cold-rolled iron with frequency range 10^5 to 10^{-2} Hz.

	Log(|Z|/Ohm) at 10 mHz	|Z|/Ohm at 10 mHz
Cold-rolled	4.37 ± 0.19	$2.34\times10^{4\pm0.19}$
Hot-rolled	4.42 ± 0.18	$2.63\times10^{4\pm0.18}$

Table 10) Calculated average impedance rolled iron at 10 mHz

3.5. Dual phase steel results

3.5.1. Electrochemical examination

3.5.1.1. chronoamperometry

Chronoamperometric measurements are initial started as the first electrochemical test. Herein, the current density [mA/cm^2] is set out to the time [sec]. The CA is performed at -1,3V vs. Hg/HgO and kept for 120 seconds (cathodic polarization). After this period, the current density has largely stabilized at a value around of J = -5 mA/cm^2 for both the ferrite iron and dual phase steel.

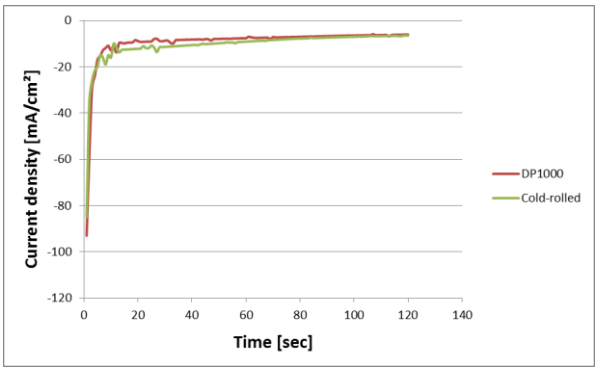

Fig. 54 Typical chronoamperometric response of ferrite and ferrtite+martensite samples at -1.3V vs. MMO in 6M KOH and 0.01M sodium stannate for 2 minutes.

3.5.1.2. cyclic voltammetry

Next the Cyclic voltammetry technique would follow. The CV graphs for the samples are shown in Figure 55 , which showcase similarities in peaks and overall structure.

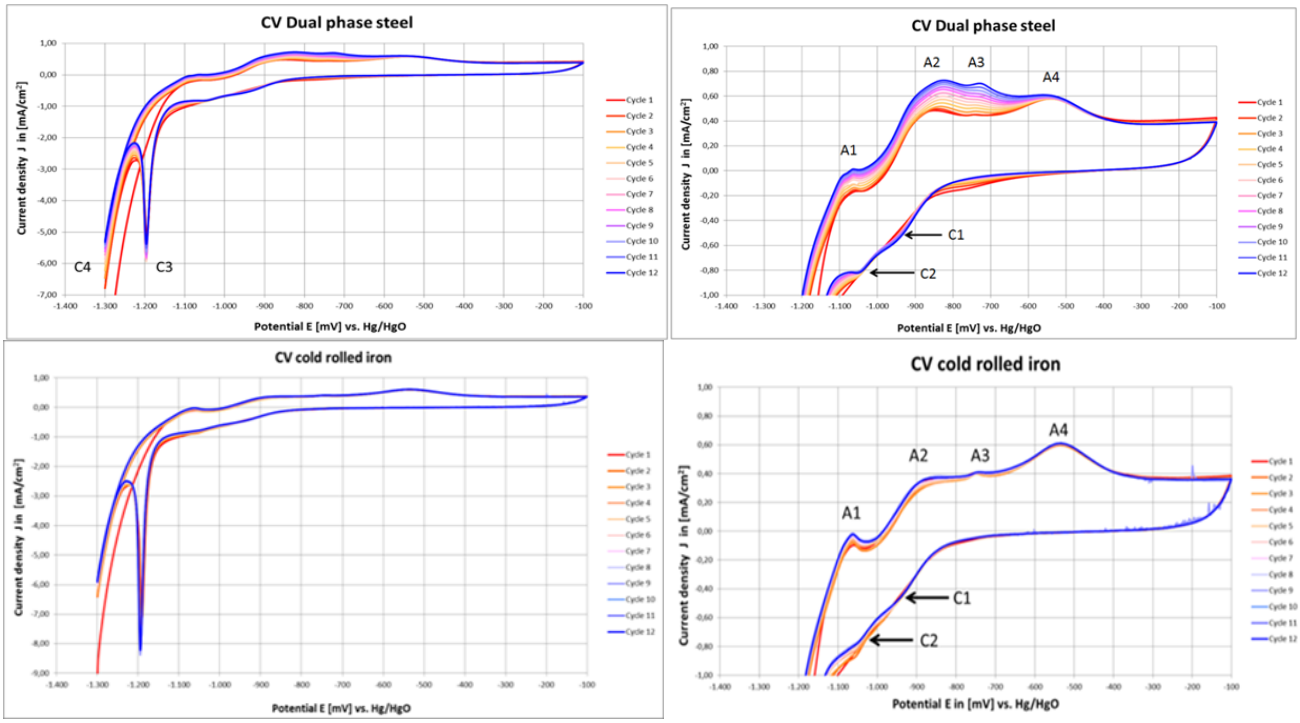

Fig. 55 Behaviour of DP1000 vs. cold rolled iron for 12 cycles in 6M KOH and 0.01M sodium stannate at a 5 mV/s scan rate.

The CV results indicate the DP1000 electrode shows an increment in current density for the oxidation reaction at A1, A2, and A3. Thus, indicating that the conversion of formation of Fe to $Fe(OH)_2$ and $Fe(OH)_2$ to Fe_3O_4 is enhanced with cycles. This is in contrast to the earlier discussed rolled iron which exhibits hardly any increase of the first three oxidation reactions. Furthermore, the anodic reaction of A4 is stable for 12 cycles as is seen in all other samples. The reduction reactions for the dual phase steel specimen shows an increasing C1 cathodic current, which suggests $FeOOH$ shows better reversibility over cycles. Meanwhile, the C2 peak is observed to remain constant. Overall, the anodic currents in the dual phase material are rising as cycling proceeds while the anodic peaks in the cold rolled sample are seen to stay more constant. The could imply that less stable $Fe_3O_4$is formed for the iron anode composed of solely ferrite.

3.5.1.3. peak height ratios

Regarding the A2/A3 ratio, the dual phase sample exhibits a nearly constant progress over cycling which has an average value of 0.99 in the 1st cycle and 0.94 at the 12th cycle as seen in Figure 56. The single phased iron sample shows an increasing trend of the ratio over consecutive cycling, being 0.95 at the initial cycle and 1.06 at the last cycle. This could imply that the α-iron specimen becomes increasingly effective in the conversion of iron to iron hydroxide, relative to the subsequent oxidation reaction to Fe_3O_4. Although, these differences in behaviour are small and on average the ratio of the A2/A3 ratio is similar. Experiments where more cycles are executed as well as more repeated tests could confirm if more clear differences are present among these materials.

The peak height ratio A2/A4 development of DP1000 is determined. The sample displays a rising ratio over 12 cycles, achieving a value of 1.13 at the 12th cycle. This is (partially) in contrast with cold-rolled ferrite sample. On the one hand, the pure (ferritic) iron sample also exhibits an increasing development of the A2/A4 ratio over cycling. On the other hand however, the average A2/A4 value of the dual phase steel is 1.02 versus 0.66 for the pure iron specimen. Despite the error margins present, this difference is approximately 55%. This suggests that the martensite/ferrite material considerably outperforms the α-iron sample. Since it demonstrates that the conversion of iron to iron hydroxide, relative to the subsequent oxidation reaction to $FeOOH$ is highly more effective.

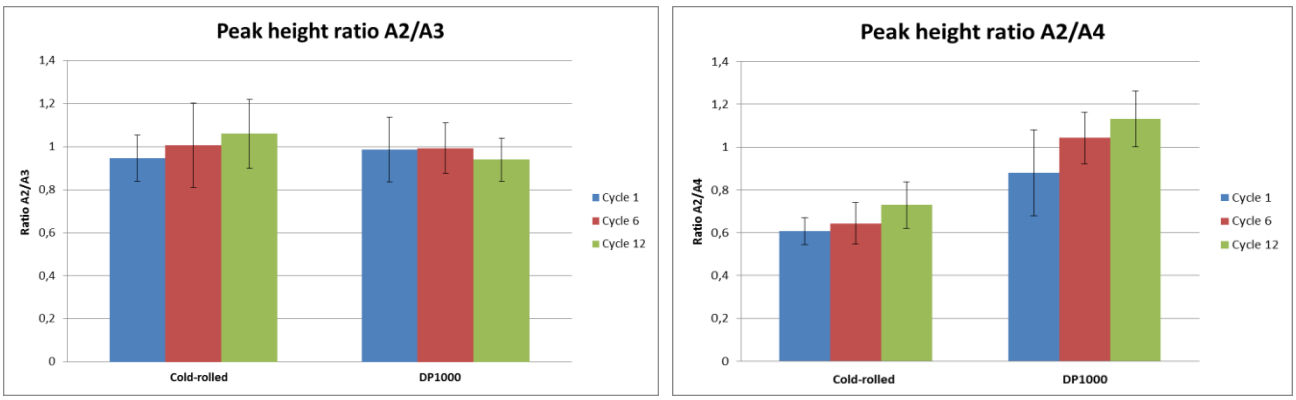

Fig. 56 Column graphs showing the progress of the A2/A3 and A2/A4 peak height ratios for a ferrite and ferrite+martensite samples for cycle 1,6 and 12.

In summary, a difference in A2/A3 ratio between DP1000 and ferrite phase iron, which is related to the formation of Fe_3O_4, is somewhat present. A slight upwards trend is seen for the single phased pure iron. The difference in A2/A4 ratio between DP1000 and ferrite phase iron, which is related to the formation of $FeOOH$ is more pronounced. Relatively, less $FeOOH$ product is formed for dual phase steel compared to the pure iron sample. On average, this difference in ratio is over 50%. This could indicate that less hydroxides are formed for the DP anode.

3.5.1.4. peak area C3

The surface area calculated of the C3 peak, associated to the reaction: $Fe(OH)_2 + 2e^- \rightarrow Fe + 2OH^-$ for DP1000 is illustrated in Figure 57. The dual phase steel shows an increasing trend in peak area over cycling, indicating more iron hydroxide is converted in later cycles. Being 35 C/m^2 in the initial stage and 44 C/m^2 at the last cycle. The α-iron sample also displays an increasing trend over cycling from 95 to 103 C/m^2. Though in Figure 57, it's observed that the mean C3 peak area of pure iron is over twice as large in comparison to DP1000. It seems that the more intense HER can partly be clarify the lower C3 peak area. Due to this phenomena, more electrons are diverted to the HER and less towards the reaction for C3. Taking all CV graphs for the DP1000 electrodes in consideration, the C3 peak potential seems slightly shifted towards the HER reaction which could also explain the lower C3 peak area, as this is now more concealed.

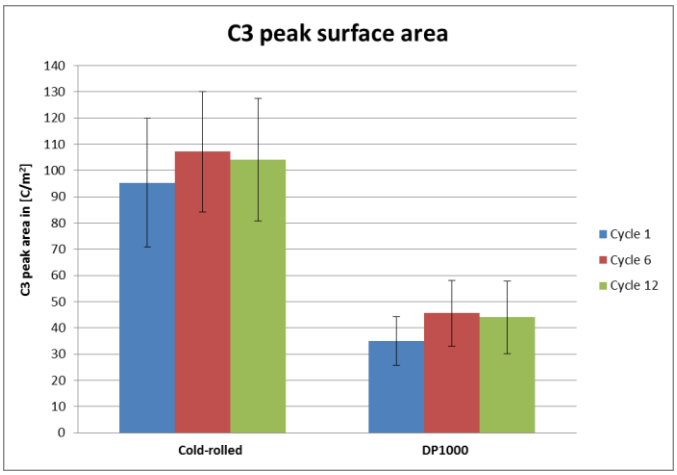

Fig. 57 Column graphs showing the progress of the C3 peak area of the DP1000 and cold-rolled iron samples for cycle 1,6 and 12.

3.5.1.5. HER intensity

Lastly, the HER C4 peak is inspected for DP1000 steel. The HER gradient progress over 12 cycles is depicted in Figure 58. A familiar trend is observed in which the HER slope slowly decreases over cycling from 700 to 600 A/(V·cm^2). Compared to the single phase iron, DP1000 displays as slightly higher HER rate if the uncertainty bars are left aside. A 17% rise in HER gradient for is present which could mean that pure iron sample exhibit less hydrogen gas formation. Given the extensive overlap of error margins, the current result could be verified by conducting additional rerun experiments.

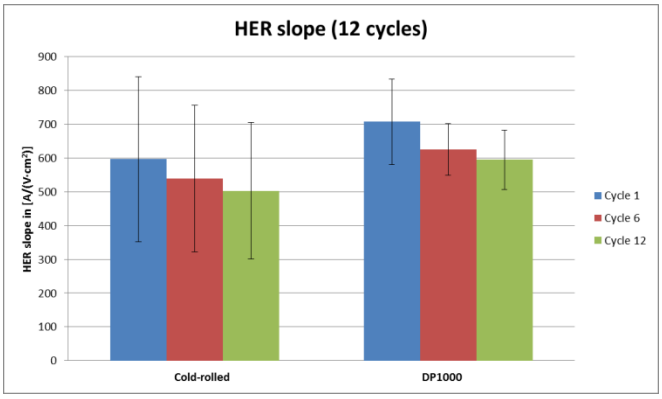

Fig. 58 Column graphs showing the progress of the HER intensity of DP1000 and pure cold rolled samples for cycle 1,6 and 12.

3.5.1.6. Impedance Tests

Bode plots indicate a similar course over the frequency range applied for both specimens, in Figure 59. Looking at the Nyquist plot it becomes clear that the α-iron specimen shows a marginally higher resistance at low frequencies which implies that the oxide/hydroxide film produced on this sample after 12 consecutive cycles forms a greater barrier for charge transfer. A total resistance of 17.4 kΩ versus 23.4 kΩ are found at 10 mHz for the dual phase and pure iron sample, respectively (34% larger impedance for the purely ferritic specimen).

Possibly a denser layer is formed which consist of more Fe_3O_4 and/or $FeOOH$. Given the CV findings, the most probable explanation is the relatively lower A2/A4 ratio for the α-iron material which suggests more (irreversible) $FeOOH$ could be present after 12 cycles. Future experiments where the data fitting is applied in which a suitable equivalent circuit is obtained, including fitting values could validate if this presumption justified.

	Log(|Z|/Ohm) at 10 mHz	|Z|/Ohm at 10 mHz
DP1000	4.24 ± 0.14	$1.74\times10^{4\pm0.14}$
Cold rolled	4.37 ± 0.19	$2.34\times10^{4\pm0.19}$

Table 11) Calculated average impedance DP1000 and cold rolled at 10 mHz

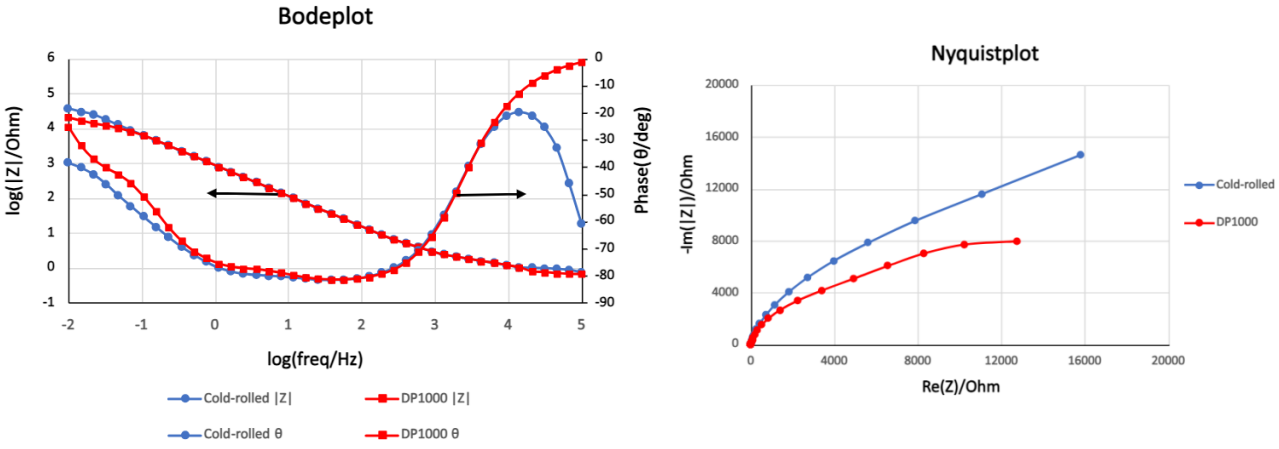

Fig. 59 Bode plot and Nyquist plot for samples dual phase steel vs. pure (ferrite) iron with frequency range 10^5 to 10^{-2} Hz.

3.6. Iron foam

3.6.1. Electrochemical examination

An iron foam which has been probed as anode material, exhibits a somewhat different CV curve overall compared to solid iron electrodes. This is very likely due to porous nature of this material, which allows electrolyte to be slowly absorbed into the material over time. The enlarged available surface area permits a larger amount of active material to react with the solution. The latter translates to a greater amount of species to oxidize and reduce, which is seen in the CV in Figure 60.

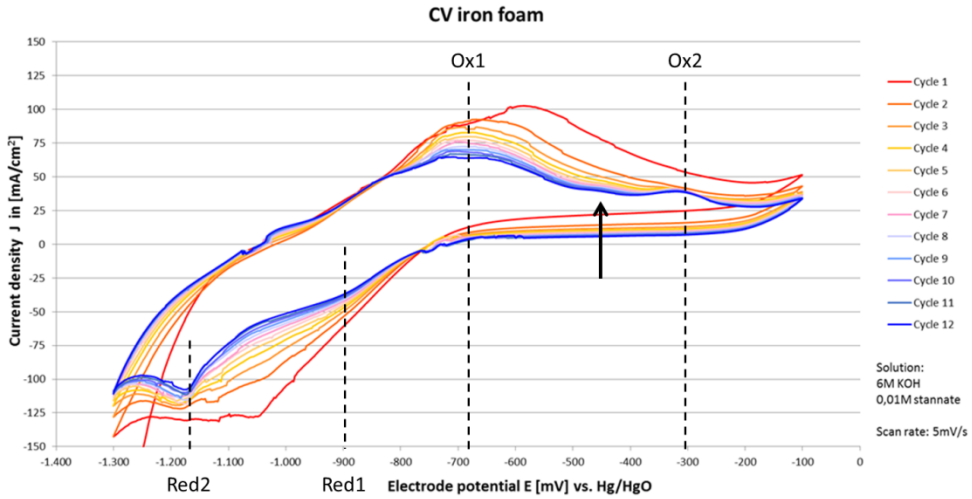

Fig. 60 Behaviour of the iron foam for 12 cycles in 6M KOH and 0.01M sodium stannate at a 5 mV/s scan rate.

More specifically, the foam showcases peak current densities which are order of magnitudes higher compared to the flat non-porous iron pieces. At the same time, the peaks locations are not as well pronounced as for the solid samples, since peak widening as a consequence of overlap has occurred. In addition, due to the slow absorption of the solution, peak shifts appear to have taken place as some reactions could have occurred simultaneously . Another factor that could have played a role was the preparation applied to remove initial rust of the foam. Due to the characteristic porous nature of this material, it doesn't lend itself for the conventional sample preparation routine, consisting of sanding and polishing. Therefore the alternative method applied, as earlier described could have been less effective in removing superficial contaminations and irregularities.

The cyclic voltammetry graph for the iron foam illustrates the rise of peaks over cycling (some of which apparently extend over a wide potential range) as well as a possible shift in peak locations. The exact processes taking place are complicated to identify at first sight. Therefore the behaviour of the curve is clarified for the initial cycling stages followed by the final cycling phase.

Initially, CA is applied for 5 minutes at a potential of -1.0V vs. Hg/HgO. Next, CV is started at -1.3V to -0.1V vs. Hg/HgO and back, for 12 cycles. Then, after one half cycle, CA is again

implemented at -0.1V vs. Hg/HgO for 5 minutes. Lastly, EIS is applied with the same settings as described for the solid iron electrodes.

In cycle 1 (red line), a broad top spans over -0,8 and -0,5V which seems to be composed of two individual overlapping peaks. This phenomena can be ascribed to initial oxidation of iron (with or without intermediate product $FeOH_{ads}$ formation) to $Fe(OH)_2$. This peak just exceeds 100 mA/cm^2 as its maximum current density. Further oxidation peaks are not detected in the CV for the potential range applied. In the reverse reduction process of the first cycle, likewise only one distinct wide peak is present between -1,0V and -1,2V. Logically, this one could be related to the reduction of iron hydroxide. At -1,3V the HER has initiated.

Alternatively, since the first oxidation peak shows to form an abundance $Fe(OH)_2$, the possible subsequent oxidation of $Fe(OH)_2$ into another oxide/hydroxide product could be concealed by the initial broad anodic peak. For example, due to capillary effect of the absorbing electrolyte in the foam, it's not ruled out that the peak locations have shifted wherein the peak maximum at -0,6V is caused by the reaction:

$$3Fe(OH)_2 + 2OH^- \rightarrow Fe_3O_4 + 4H_2O + 2e^-$$

Which would be the expected successive reaction taking place (as observed for the solid iron samples). A CV test consisting of solely one anodic half cycle and subsequent surface analysis (for example SEM/EDX) of species could prove or disprove its presence.

As cycling continues, the CV curves decrease in magnitude while some peaks are seen to arise. Considering the last cycle (blue line), the previous mentioned broad peak between -0,8V and -0,5V, flattened and is narrower. Two obvious peaks cannot be distinguished anymore but rather a single one at -0,7V. Moreover, two other oxidation peaks emerge at -0,45V and -0,3V. These are most likely linked to the further oxidation of $Fe(OH)_2$ to Fe_3O_4 and $FeOOH$, respectively. Similarly, surface analysis after 12 and one anodic half cycle could clarify which species are present and in what quantity. Because of the relative lower purity iron composition of the foam (table. 7), other elements/chemical compounds could also be responsible for the curve behaviour.

In the last reduction cycle, two peaks are identified at -0,9V and -1,17V. The latter is nearly identical to the potential for the reduction reaction of $Fe(OH)_2$ (C3, -1,16V) observed in the solid pure iron samples. Therefore, this peak is attributed to the aforementioned reaction. Lastly, the peak at -0,9V is similar to the reduction of iron hydroxide to $FeOOH$ (C1) which was determined to be located at -0,91V for pure iron. Thus after repeated cycling this peak develops and corresponds to reduction of $Fe(OH)_2$.

The rather small bump which arises near -0,45V vs. Hg/HgO in the final cycles is likely due to the formation of Fe_3O_4. As the reaction potential typically lies between the potentials of the A1 and A3 reactions earlier discussed. Because of its limited intensity (and possible irreversibility), the corresponding reduction peak is also hard to recognize in the cathodic half cycle.

Suggestions for getting a better understanding of the oxidation/reduction of the iron foam include applying more cycles in order to see the progress of peaks more clearly over cycling. Another approach could be to vary scan rates to possibly observe different behaviour of the reaction kinetics in the cyclic voltammogram.

Overall, peaks in the CV are more complex to classify compared to solid (pure) iron specimen. Most importantly, the specific cellular design of the foam is responsible for this phenomenon. Initial cycling seems to indicate a lot of iron is conversed to $Fe(OH)_2$ while the formation of unwanted iron oxide products is minimal. As cycling progresses however, the current density peak for the conversion to $Fe(OH)_2$ is seen to decline to about 67 mA/cm^2 in the 12th cycle. Meanwhile the reaction peaks associated to the evolution of Fe_3O_4 and $FeOOH$ grow steadily. It implies that iron oxide and hydroxide species built up over time, as the reduction peak for $Fe(OH)_2$ to Fe becomes less effective.

3.6.2. Impedance tests

The Nyquist and Bode plots for the iron foam are illustrated in Figure 61. The plots showcase different behaviour compared to the planar iron electrodes. Firstly, the total impedance which is reached at low frequencies, is almost three orders of magnitudes smaller.

First, considering the pre-set anode surface area (exposed to the electrolyte) in EC-lab. The total surface of samples is required to fill in, in order to acquire and compare CV plots (current density in [mA/cm^2]) of samples. Solid (non-porous) specimens inherently have a fixed surface area which can be determined. For a porous foam which has an irregular permeable structure, this is not the case. For convenience, the same surface area exposed to the electrolyte is applied for the iron foam material as the exact area is difficult to calculate. In reality, the surface area exposed to solution for the foam is considerably higher. Due to more "impure" composition of the foam, the oxide/hydroxide film that forms in are more imperfect compared to iron oxide/hydroxides formed for the high purity iron anodes. Moreover, due to the porous structure, the oxides/hydroxides might not able to form a stable layer at the surface of the foam. This translate to a more defective, porous film with a lower resistance at the surface.

The impedance plots do display realistic data which is useful to compare with the solid samples. Particularly, the presence of a semi-circle with a tail in the Nyquist plot is observed. This is linked to a Warburg element for equivalent circuit in EIS fitting, which is related to diffusion control mechanism. This process is expected since a cellular network in foam allows for diffusion of electrolyte and species through the foam.

	Log(|Z|/Ohm) at 10 mHz	|Z|/Ohm at 10 mHz
Iron foam	1.41 ± 0.25	$2.57\times10^{1\pm0.25}$

Table 12) Calculated average impedance foam at 10 mHz

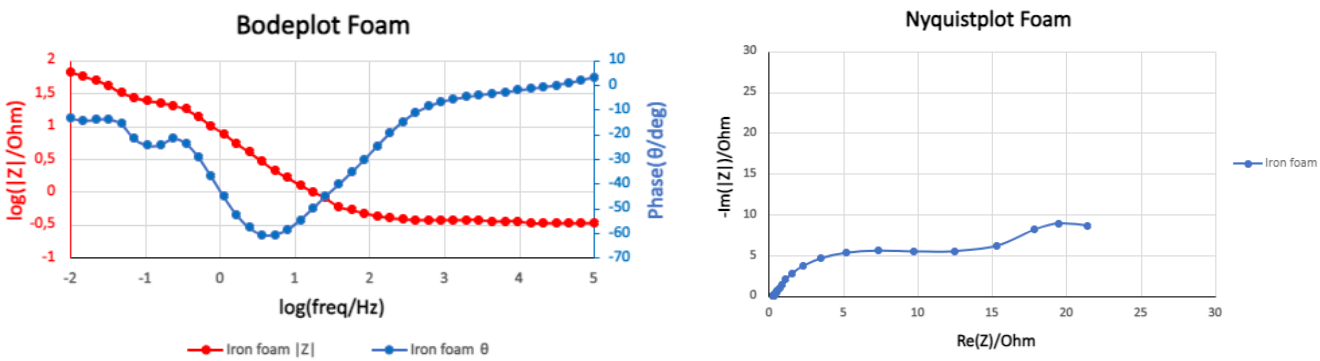

Fig. 61 Bode plot and Nyquist plot for iron foam with frequency range 10^5 to 10^{-2} Hz.

3.7. Sodium stannate

Sodium stannate $Na_2[Sn(OH)_6]$ (also represented as $Na_2SnO_3 \cdot 3H_2O$ or Na_2SnO_3 as its anhydrous form) is an inorganic compound which has a variety of applications in several different industries. Most commonly, it is applied as a salt in alkaline tin plating electrolyte. Herein, the surface of a metal or alloy is coated with thin film composed of Tin. It can function as a corrosion resistant layer for iron and steels for example, inhibiting oxidation processes. Furthermore, electronic components in circuits and electrical wiring benefits from tinplating as it provides excellent conductivity as well as clean smooth surface [131].

A few studies suggests that sodium stannate in small quantities (added to the electrolyte) in certain metal battery applications can be advantageous.

Chang et al. [132] has investigated the effect of stannate as an electrolyte additive on corrosion and electrochemical performances for aluminium electrodes in an alkaline solution in the context of aluminium batteries. Most notably, problems arise in the form of self-discharge reactions and evolution of hydrogen gas which are undesirable. Pure aluminium in 4 mol·L^{-1} KOH methanol-water mixed solution is subjected to galvanostatic discharge and polarization curve experiments. Na_2SnO_3 with various concentration 0.0 – 10 mmol·L^{-1} (0 – 0,01M) are added to the solution. The EDAX results indicate that the aluminium surface is covered with a dense and thin deposition film in the electrolyte composed of elemental Tin, which facilitates a higher overpotential for hydrogen evolution. As stannate content increases, the film is said to grow in thickness, but cracks start to occur in the deposition layer. The following reaction (33) is stated to take place in the system:

$$3SnO_3^{2-} + 4Al + 9H_2O \rightarrow 3Sn + 4Al(OH)_4^- + 2OH^- \qquad (33)$$

It is observed that severe corrosion is present in the electrolyte for the aluminium without added sodium stannate. A reduction in current density of 87% is observed for 1.5 mmol·L^{-1} compared to 0 mmol·L^{-1} Na_2SnO_3 solved in solution. This (low) concentration is shown to be the most effective.

In a similar report, the same authors also studied the effect of pure aluminium samples pre-treated in alkaline stannate solutions on the galvanostatic discharge performance and the effect of partial replacement of water solvent by methanol for the electrolyte on hydrogen gas formation [132], [133]. These studies reveal relatively low corrosion rate, better discharge performance and inhibition of the HER are obtained. The presence of elemental Sn in the deposition layer supposedly facilitates the formation of a porous discharge product film at the discharge surface, enhancing discharge performance.

Initially, the provided solution for electrochemical tests was composed of 6M KOH and 0.01M sodium stannate trihydrate. During the course of the research, the interest towards the actual effect of this stannate in the electrolyte was evoked. Therefore, tests have also been carried out in which stannate is not added to the solution. Tests where no sodium stannate was added to the electrolyte are described in this section. Due to the time constraints for the thesis, an elaborate, in detail analysis with the peak height ratios etc. (as in previous sections) could not be completely performed unfortunately. Since not for all samples a total of two (successful) repeated experiment could be acquired in time. However, some very clear effects of tests without sodium stannate did appear to be present.

For all tests that could be performed, it was seen that the HER was much more intense during 12 cycles for all solid sample when no $Na_2SnO_3 \cdot 3H_2O$ was present in the solution. This is directly observable by the far more negative values reached for the C4 peak. When calculating the gradient in the same manner as described before, slopes of around 1500-1900 A/(V·cm^2) are seen on average as opposed to 400-700 A/(V·cm^2) for the experiments including stannate. Thus sodium stannate additive in the solution provides approximately a threefold reduction in HER gradient.

For convenience sake only the hot-rolled iron and DP1000 steel are shown to illustrate this discrepancy in HER magnitude in Figure 62.

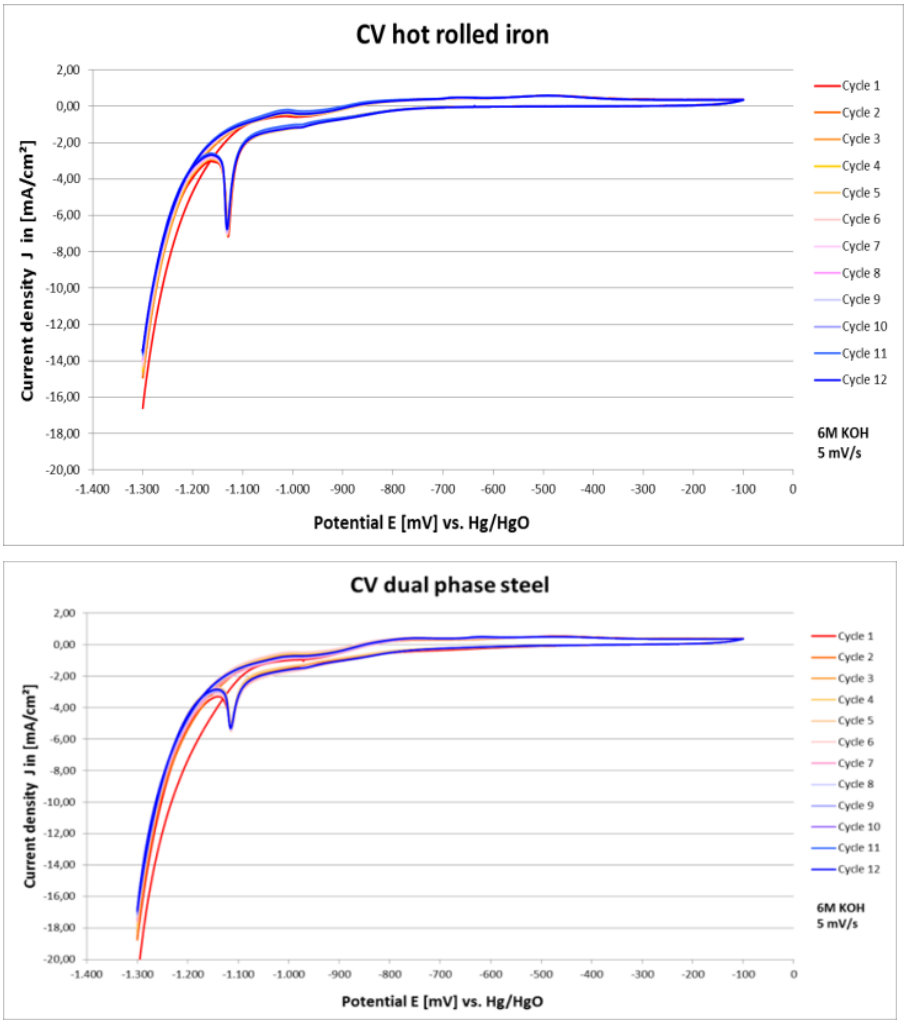

Fig. 62 a) hot-rolled iron without sodium stannate. b) DP1000 steel without sodium stannate

Regarding the remaining oxidation and reduction reactions peaks the sodium stannate did not appear to have any meaningful effect for the solid samples.

Furthermore, the iron foam is demonstrated with and without 0.01M $Na_2SnO_3 \cdot 3H_2O$, as seen in Figure 63.

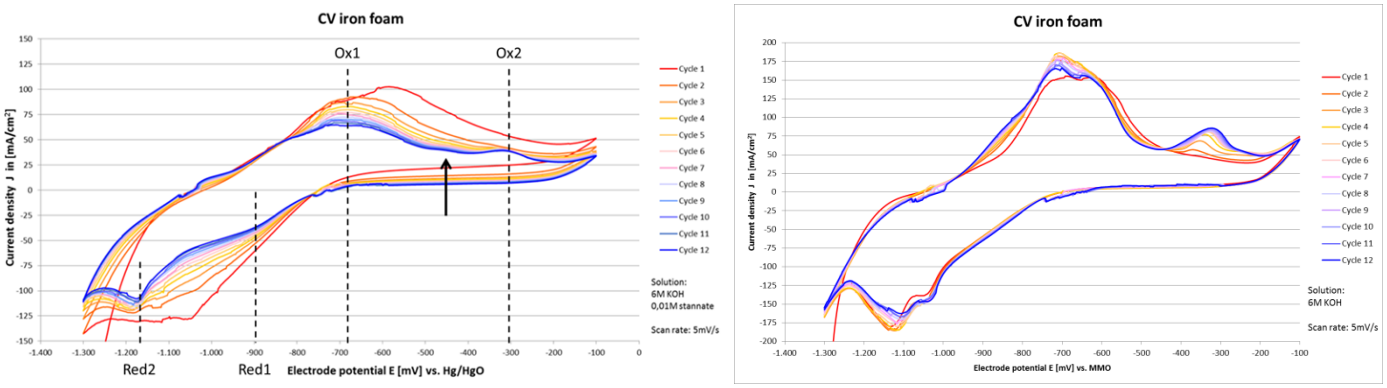

Fig. 63 On the left, CV curve of iron foam with sodium stannate. On the right, CV graphs without stannate in the solution.

As well as a higher HER, the CV graph of the foam without stannate seems to have overall a more steady behaviour of the oxidation and reduction reactions over 12 cycles. Peaks do not to alter in magnitude drastically except for one. At -300mV a peak is seen to arise which can be linked to the Ox2, as in the Figure on the left. Suggesting that sodium stannate could also play a role in inhibiting the formation of iron oxides/hydroxides products.

Due to the (apparently) significant impact of sodium stannate, some solid samples exposed to 6M KOH and 0.01M Na_2SnO_3 have been carefully blown dry and investigated via SEM and XRF after CV and EIS tests. However, any traces of stannate (i.e. elements Na and Sn) could not be found on the specimens. Thus, indicating that (at least after tests), this species itself does not adhere to the iron surface. For the foam this procedure was not performed.

Additional tests should confirm if the effects of stannate are truly significant and were not influenced by other factors like a switch in measurement station or caused by ambient disturbances and such.

4. Conclusion and recommendations

The current Thesis has attempted to clarify the complex relationship between the microstructure of iron and its oxidation and reduction behaviour. This was specifically performed in an alkaline electrolyte and with electrochemical experiments which imitates the conditions for iron electrodes in Fe-air batteries. Several microstructures have been created and tested to recognize trends, whereby ideally the effect of one isolated microstructural feature could be explained. Moreover, an iron foam was tested as an alternative electrode topology for comparison with solid iron samples. Finally, the influence of 0,01M $Na_2SnO_3 \cdot 3H_2O$ was probed as it could be effective to suppress the HER.

Considering the hypotheses proposed, the following conclusions can be made based on the findings in the present research report:

- Regarding grain size; cyclic voltammetry experiments indicate that small grained iron exhibits slightly better reversibility of the oxide/hydroxide products. A weak trend with grain size was observed here. However, EIS did demonstrates the largest resistance was found for the medium grained sample, followed by the small grain anode and, lastly, the large grain electrode, which contradicts the CV results. In terms of HER kinetics, a slightly larger decline in HER slope was observed for the small grain sample. The proposed hypothesis in section 1.8. is thus refuted.

- Identification of the microstructures did reveal no difference was present in ρ_{GND} between the provided hot-rolled and cold-rolled iron. Therefore, the effect of ρ_{GND} could not be established and the proposed hypothesis not be verified or refuted. A difference in crystallographic orientation was found instead. The cold-rolled sample with a relatively strong <111> // ND orientation, exhibits a tendency to form relatively less oxide/hydroxide products over cycling compared to the hot-rolled sample, which a weak preference of the <101> // ND component. On average, the cold-rolled sample shows a lower HER intensity. EIS results for both samples are nearly identical. The proposed hypothesis in section 1.8. could neither be confirmed nor refuted.

- Regarding phase constituents; The cold-rolled dual phase steel forms relative less $FeOOH$ compared to cold-rolled iron (fully ferrite), according to CV tests. Furthermore, impedance experiments do show a lower resistance at low frequencies for DP1000 steel in comparison to the pure iron anode. Meanwhile, the HER intensity is slightly lower for the pure iron specimen. Therefore, proposed hypothesis in section 1.8 is confirmed.

- Open-cell foam; An iron foam composed of a cellular structure demonstrates anodic and cathodic currents which are order of magnitudes larger compared to solid iron electrodes. Nonetheless, reactions are more difficult identify due to absorption of the electrolyte. The proposed hypothesis in section 1.8. is confirmed.

- Regarding sodium stannate; The addition of 0,01M $Na_2SnO_3 \cdot 3H_2O$ to the electrolyte greatly reduces the HER intensity for solid samples. A two to threefold reduction is observed. Other reactions occurring do not seem to be affected by this additive for the solid samples. For the foam material, the reduction in HER is also seen to decrease, although to a lesser extent. An oxidation reaction related to the formation of insulative oxide species seems to be repressed in the presence of sodium stannate. A deposition layer formed containing Tin could be the cause for these phenomena. The proposed hypothesis in section 1.8. is confirmed.

Recommendations for future research considering the observations of the current study include:

- More investigation is performed towards the effect and efficacy of sodium stannate as electrolyte additive. Several concentrations could be applied to find an optimum concentration for reducing certain (unwanted) reactions.

- The iron foam concept is further improved by adding additives to this electrode. Potentially, such a modified foam can provide more current while also providing excellent resistance to the formation of insulating species.

- One could perform similar tests as in the current thesis with iron samples having distinct differences in defect density aspects, in order to unveil the effect of these properties.

- During cyclic voltammetry in the current thesis, more cycles could have been applied for all CV tests, to showcase a more clear course of the samples. Also, EIS experiments in which proper fitting values and equivalent circuits are obtained could be pursued. Since this could help to better analyse the impedance contributions of certain compounds.

- In this thesis, surface characterization after electrochemical experiments is barely conducted. Techniques like XPS analysis could be used to determine the quantity or fractions of oxide and hydroxides on the anode surface after tests.

- In the context of improving iron-air batteries, full-cell (charge/discharge) tests could also be employed to investigate the effect of specific microstructures in these type of experiments.

5. References

[1] Ministère de la Transition Écologique et Solidaire. Impacts of Climate Change; Ministère de la Transition Écologique et Solidaire: Paris, France, 2015; Volume 213.

[2] National Academy of Sciences. Climate Change: Evidence and Causes; National Academies Press: Washington DC, USA, 2014.

[3] Blomgren, G.E. The Development and Future of Lithium Ion Batteries. J. Electrochem. Soc. 2017, 164, A5019–A5025.

[4] Amine, K.; Kanno, R.; Tzeng, Y. Rechargeable lithium batteries and beyond: Progress, challenges, and future directions. MRS Bull. 2014, 39, 395–401

[5] Weinrich, H., Durmus, Y.E., Tempel, H., Kungl, H., Eichel, R.-A. Silicon and iron as resource-efficient anode materials for ambient-temperature metal-air batteries: A review 2019 Materials12(13),2134

[6] Rahman, M.A.;Wang, X.;Wen, C. High Energy Density Metal-Air Batteries: A Review. J. Electrochem. Soc. 2013, 160, A1759–A1771

[7] Christensen, J.; Albertus, P.; Sanchez-Carrera, R.S.; Lohmann, T.; Kozinsky, B.; Liedtke, R.; Ahmed, J.; Kojic, A. A Critical Review of Li/Air Batteries. J. Electrochem. Soc. 2012, 159, R1–R30

[8] Jung, K.-N.; Kim, J.; Yamauchi, Y.; Park, M.-S.; Lee, J.-W.; Kim, J.H. Rechargeable lithium–Air batteries: A perspective on the development of oxygen electrodes. J. Mater. Chem. A 2016, 4, 14050–14068.

[9] LithiumBattery, JB BATTERY, The Pros And Cons Of Lithium Ion Batteries With Advantages and Disadvantages, 2019, https://www.lithiumbatterychina.com/blog/2021/08/02/the-pros-and-cons-of-lithium-ion-batteries-with-advantages-and-disadvantages/

[10] Evergreen, S. arstechnica. Lithium costs a lot of money—so why aren't we recycling lithium batteries? 2022, https://arstechnica.com/science/2022/04/lithium-costs-a-lot-of-money-so-why-arent-we-recycling-lithium-batteries/

[11] Marsh, J. EnergySage. Recycling solar batteries and electric car batteries: what you need to know about lithium-ion battery recycling, 2021, https://news.energysage.com/lithium-ion-battery-recycling/

[12] Li Y. Y.; Restauro A.R.; To E. Bloomberg. The Trouble With Lithium, 2022, https://www.bloomberg.com/news/features/2022-05-25/lithium-the-hunt-for-the-wonder-metal-fueling-evs?leadSource=uverify%20wall

[13] Larcher, D.; Tarascon, J.-M. Towards greener and more sustainable batteries for electrical energy storage. Nat. Chem. 2015, 7, 19–29.

[14] Vesborg, P.C.K.; Jaramillo, T.F. Addressing the terawatt challenge: Scalability in the supply of chemical elements for renewable energy. RSC Adv. 2012, 2, 7933–7947

[15] U.S. Geological Survey. Mineral Commodity Summaries; U.S. Geological Survey: Reston, VA, USA, 2015; Volume 1.

[16] Andrus, C.D. Principles of a Resource/Reserve Classification For Minerals; U.S. Geological Survey: Reston, VA, USA, 1980.

[17] International Energy Agency. Global EV Outlook 2017; International Energy Agency: Paris, France, 2017; ISBN 9789264278882.

[18] Wellmer, Friedrich-Wilhelm; Becker-Platen, Jens Dieter. "Global Nonfuel Mineral Resources and Sustainability"

[19] Mucha, Lena; Sadof, Karly Domb; Frankel, Todd C. (2018-02-28). "Perspective - The hidden costs of cobalt mining". The Washington Post.

[20] Liu Q., Pan Z., Wang E., An L., Sun G. Aqueous Metal-Air Batteries: Fundamentals and Applications, 2020, Energy Storage Materials 27, pp. 478-505

[21] McKerracher, R.D.; Ponce De Leon, C.; Wills, R.G.A.; Shah, A.A.; Walsh, F.C. A Review of the Iron-Air Secondary Battery for Energy Storage. Chempluschem 2015, 80, 323–335

[22] Ravikumar, M.K.; Sundar Rajan, A.; Sampath, S.; Priolkar, K.R.; Shukla, A.K. In Situ Crystallographic Probing on Ameliorating Effect of Sulfide Additives and Carbon Grafting in Iron Electrodes. J. Electrochem. Soc. 2015, 162, A2339–A2350

[23] Vijayamohanan, K.; Balasubramanian, T.S.; Shukla, A.K. Rechargeable alkaline iron electrodes. J. Power Sour. 1991, 34, 269–285

[24] Manohar, A.K.; Malkhandi, S.; Yang, B.; Yang, C.; Surya Prakash, G.K.; Narayanan, S.R. A High-Performance Rechargeable Iron Electrode for large-scale battery-Based Energy Storage. J. Electrochem. Soc. 2012,159, A1209–A1214.

[25] Narayanan, S.R.; Prakash, G.K.S.; Manohar, A.; Yang, B.; Malkhandi, S.; Kindler, A. Materials challenges and technical approaches for realizing inexpensive and robust iron-air batteries for large-scale energy storage. Solid State Ionics 2012, 216, 105–109

[26] Shangguan, E.; Li, F.; Li, J.; Chang, Z.; Li, Q.; Yuan, X.-Z.;Wang, H. FeS/C composite as high-performance anode material for alkaline nickel-iron rechargeable batteries. J. Power Sour. 2015, 291, 29–39.

[27] Figueredo-Rodríguez, H.A.; McKerracher, R.D.; Insausti, M.; Luis, A.G.; De León, C.P.; Alegre, C.; Baglio, V.; Aricò, A.S.; Walsh, F.C. A Rechargeable, Aqueous Iron Air Battery with Nanostructured Electrodes Capable of High Energy Density Operation. J. Electrochem. Soc. 2017, 164, A1148–A1157.

[28] Chen, Z.; Yu, A.; Higgins, D.; Li, H.;Wang, H.; Chen, Z. Highly Active and Durable Core—Corona Structured Bifunctional Catalyst for Rechargeable Metal—Air Battery Application. Nano Lett. 2012, 12, 1946–1952.

[29] BU-105: Battery Definitions and what they mean, 2021, https://batteryuniversity.com/article/bu-105-battery-definitions-and-what-they-mean

[30] Wang, H.; Liang, Y.; Gong, M.; Li, Y.; Chang, W.; Me_ord, T.; Zhou, J.; Wang, J.; Regier, T.; Wei, F.; et al. An ultrafast nickel-iron battery from strongly coupled inorganic nanoparticle/nanocarbon hybrid materials. Nat. Commun. 2012, 3, 917.

[31] Yang, C.; Manohar, A.K.; Narayanan, S.R. A High-Performance Sintered Iron Electrode for Rechargeable Alkaline Batteries to Enable Large-Scale Energy Storage. J. Electrochem. Soc. 2017, 164, A418–A429.

[32] H.W. Weinrich, Resource-Efficient Anodes for Rechargeable Fe-Air Batteries with High Energy Density, 2018

[33] Jiang J, Liu J. Iron anode-based aqueous electrochemical energy storage devices: recent advances and future perspectives. Interdiscip Mater. 2022;1:116-139. doi:10.1002/idm2.12007

[34] Currents in Electrochemical Cells, Harvey D. DePauw University, 2022; https://chem.libretexts.org/Bookshelves/Analytical_Chemistry/Instrumental_Analysis_(LibreTexts)/22%3A_An_Introduction_to_Electroanalytical_Chemistry/22.05%3A_Currents_in_Electrochemical_Cells

[35] Pourbaix Diagrams, Chemistry 310, Penn State University, 2021; https://chem.libretexts.org/Bookshelves/Inorganic_Chemistry/Book%3A_Introduction_to_Inorganic_Chemistry_(Wikibook)/04%3A_Redox_Stability_and_Redox_Reactions/4.06%3A_Pourbaix_Diagrams

[36] Weinrich H., Come J., Tempel H., Kungl H., Eichel R-A., Balke N., Understanding the nanoscale redox-behavior of iron-anodes for rechargeable iron-air batteries, https://doi.org/10.1016/j.nanoen.2017.10.023

[37] Garche, J.; Dyer, Chris K.; Moseley, Patrick T.; Ogumi, Zempachi; Rand, David A. J.; Scrosati, Bruno (2013). Encyclopedia of Electrochemical Power Sources. Newnes. p. 407. ISBN 978-0-444-52745-5.

[38] Li, Y.; Dai, H. Recent advances in zinc-air batteries. Chem. Soc. Rev. 2014, 43, 5257–5275.

[39] Wang, Z.-L.; Xu, D.; Xu, J.-J.; Zhang, X.-B. Oxygen electrocatalysts in metal-air batteries: From aqueous to nonaqueous electrolytes. Chem. Soc. Rev. 2014, 43, 7746–7786.

[40] Lee, D.U.; Xu, P.; Cano, Z.P.; Kashkooli, A.G.; Park, M.G.; Chen, Z. Recent progress and perspectives on bi-functional oxygen electrocatalysts for advanced rechargeable metal-air batteries. J. Mater. Chem. A 2016, 4, 7107–7134.

[41] Zhang, J.; Zhao, Z.; Xia, Z.; Dai, L. A metal-free bifunctional electrocatalyst for oxygen reduction and oxygen evolution reactions. Nat. Nanotechnol. 2015, 10, 444–452.

[42] Lee, J.-S.; Tai Kim, S.; Cao, R.; Choi, N.-S.; Liu, M.; Lee, K.T.; Cho, J. Metal-Air Batteries with High Energy Density: Li-Air versus Zn-Air. Adv. Energy Mater. 2011, 1, 34–50.

[43] Cheng, F.; Chen, J. Metal-air batteries: From oxygen reduction electrochemistry to cathode catalysts. Chem. Soc. Rev. 2012, 41, 2172–2192.

[44] L. Carlsson, L. _jefors, J. Electrochem. Soc. 1980, 127, 525 –528.

[45] F. W. T. Goh, Z. Lui, X. Ge, Y. Zong, G. Du, T. S. A. Hor, Electrochim. Acta 2013, 114, 598– 604.

[46] K. Guo, Y. Li, J. Yang, Z. Zou, X. Xue, X. Li, H. Yang, J. Mater. Chem. A 2014, 2, 1509 –1514.

[47] N. Sasikala, K. Ramya, K. S. Dhathathreyan, Energy Convers. Manage. 2014, 77, 545– 549

[48] K. Jung, J. Jung, W. B. Im, S. Yoon, K. Shin, J. Lee, ACS Appl. Mater. Interfaces 2013, 5, 9902 – 9907.

[49] C. Zhu, A. Nobuta, I. Makatsugawa, T. Akiyama, Int. J. Hydrogen Energy 2013, 38, 13238 –13248.

[50] M. Yuasa, M. Nishida, T. Kida, N. Yamazoe, K. Shimanoe, J. Electrochem. Soc. 2011, 158, A605–A610.

[51] H. Ohkuma, I. Uechi, M. Matsui, Y. Takeda, O. Yamamoto, N. Imanishi, J. Power Sources 2014, 245, 947 –952.

[52] T. Takeguchi, T. Yamanaka, H. Takahashi, H. Watanabe, T. Kuroki, H. Nakanishi, Y. Orikasa, Y. Uchimoto, H. Takano, N. Ohguri, M. Matsuda, T. Murota, K. Uosaki, W. Ueda, J. Am. Chem. Soc. 2013, 135, 11125– 11130.

[53] S. Zhuang, H. Zhang, S. Liu, F. Tu, W. Zhang, C. Zhao, Int. J. Electrochem. Sci. 2014, 9, 1690– 1701.

[54] D. Kubo, K. Tadanaga, A. Hayashi, M. Tatsumisago, J. Mater. Chem. A 2013, 1, 6804 –6809.

[55] Z. Zhang, X. Wang, G. Cui, A. Zhang, X. Zhou, H. Xu, L. Gu, Nanoscale 2014, 6, 3540 –3544.

[56] J. Prakash, D. A. Tryk, E. B. Yeager, J. Appl. Electrochem. 1999, 29, 1463 – 1469.

[57] Balasubramanian, T.S., Shukla, A.K. Effect of metal-sulfide additives on charge/discharge reactions of the alkaline iron electrode, 1993, Journal of Power Sources 41(1-2), pp. 99-105

[58] Manohar, A.K., Yang, C., Narayanan, S.R., The role of sulfide additives in achieving long cycle life rechargeable iron electrodes in alkaline batteries, 2015, Journal of the Electrochemical Society 162(9), pp. A1864-A1872

[59] Gil Posada, J.O., Hall, P.J., Multivariate investigation of parameters in the development and improvement of NiFe cells, 2014, Journal of Power Sources 262, pp. 263-269

[60] S. Malkhandi, B. Yang, A.K. Manohar, G.K.S. Prakash, S.R. Narayanan, Self assembled monolayers of n-alkanethiols suppress hydrogen evolution and increase the efficiency of rechargeable iron battery electrodes, J. Am. Chem. Soc. 135 (2012) 347e353.

[61] Z. He, F. Xiong , S. Tan , X. Yao , C. Zhang , Q. An, Iron metal anode for aqueous rechargeable batteries, 2021, Materials Today Advances 11,100156

[62] A.K. Manohar, C. Yang, S. Malkhandi, B. Yang, G.K. Surya Prakash, S.R. Narayanan, Understanding the factors affecting the formation of carbonyl iron electrodes in rechargeable alkaline iron batteries, J. Electrochem. Soc. 159 (2012) A2148eA2155.

[63] R. Li, X. Ba, H. Zhang, P. Xu, Y. Li, C. Cheng, J. Liu, Conformal multifunctional titania shell on iron oxide nanorod conversion electrode enables high stability exceeding 30 000 cycles in aqueous electrolyte, Adv. Funct. Mater. 28 (2018).

[64] S. Lv, D. Zhao, Y. Li, J. Liu, A homogenous mixed coating enabled significant stability and capacity enhancement of iron oxide anodes for aqueous nickel iron batteries, Chem Commun (Camb) 55 (2019) 10308e10311

[65] B. Tian, J. Swiatowska, V. Maurice, S. Zanna, A. Seyeux, P. Marcus, The effect of Na2S additive in alkaline electrolyte on improved performances of Fe-based air batteries, Electrochim. Acta 259 (2018) 196e203.

[66] U. Casellato, N. Comisso, G. Mengoli, Effect of Li ions on reduction of Fe oxides in aqueous alkaline medium, Electrochim. Acta 51 (2006) 5669e5681.

[67] J.O.G. Posada, P.J. Hall, The effect of electrolyte additives on the performance of iron based anodes for NiFe cells, J. Electrochem. Soc. 162 (2015) A2036eA2043.

[68] K. Hayashi, Y. Wada, Y. Maeda, T. Suzuki, H. Sakamoto, W.K. Tan, G. Kawamura, H. Muto, A. Matsuda, Electrochemical performance of sintered porous negative electrodes fabricated with atomized powders for iron-based alkaline rechargeable batteries, J. Electrochem. Soc. 164 (2017) A2049eA2055.

[69] J.O. Gil Posada, P.J. Hall, Post-hoc comparisons among iron electrode formulations based on bismuth, bismuth sulphide, iron sulphide, and potassium sulphide under strong alkaline conditions, J. Power Sources 268 (2014) 810e815.

[70] A.R. Paulraj, Y. Kiros, B. Skårman, H. Vidarsson, Core/shell structure nano-iron/ iron carbide electrodes for rechargeable alkaline iron batteries, J. Electrochem. Soc. 164 (2017) A1665eA1672.

[71] J.O. Gil Posada, A.H. Abdalla, C.I. Oseghale, P.J. Hall, Multiple regression analysis in the development of NiFe cells as energy storage solutions for intermittent power sources such as wind or solar, Int. J. Hydrogen Energy 41 (2016) 16330e16337.

[72] J.O.G. Posada, P.J. Hall, Towards the development of safe and commercially viable nickel-iron batteries: improvements to Coulombic efficiency at high iron sulphide electrode formulations, J. Appl. Electrochem. 46 (2016) 451e458.

[73] B. Yang, S. Malkhandi, A.K. Manohar, G.K. Surya Prakash, S.R. Narayanan, Organo-sulfur molecules enable iron-based battery electrodes to meet the challenges of large-scale electrical energy storage, Energy Environ. Sci. 7 (2014).

[74] A.S. Rajan, S. Sampath, A.K. Shukla, An in situ carbon-grafted alkaline iron electrode for iron-based accumulators, Energy Environ. Sci. 7 (2014).

[75] A.K. Manohar, C. Yang, S. Malkhandi, G.K.S. Prakash, S.R. Narayanan, Enhancing the performance of the rechargeable iron electrode in alkaline batteries with bismuth oxide and iron sulfide additives, J. Electrochem. Soc. 160 (2013) A2078eA2084.

[76] Arunkumar, P.S., Maiyalagan, T., Kheawhom, S., Mao, S., Jiang, Z., Effect of carbon material additives on hydrogen evolution at rechargeable alkaline iron battery electrodes, 2021, Materials Science for Energy Technologies 4, pp. 236-241

[77] Mitra, D., Rajan, A.S., Irshad, A., Narayanan, S.R., High Performance Iron Electrodes with Metal Sulfide Additives, 2021, Journal of the Electrochemical Society 168(3),030518

[78] A. Ito, L. Zhao, S. Okada, and J. Yamaki, Synthesis of nano-Fe3O4-loaded tubular carbon nanofibers and their application as negative electrodes for Fe/air batteries, J. Power Sources, 196, 8154 (2011).

[79] Hua, Z., Deng, Y., Li, K., Yang, S., Low-density nanoporous iron foams synthesized by sol-gel autocombustion, 2012, Nanoscale Research Letters 7,129

[80] Zheng, W., Liu, M., Lee, L.Y.S., Best Practices in Using Foam-Type Electrodes for Electrocatalytic Performance Benchmark,2020, ACS Energy Letters 5(10), pp. 3260-3264

[81] Banhart, J., Manufacturing routes for metallic foams, 2000, JOM 52(12), pp. 22-27

[82] M.F. Ashby, A.G. Evans, N.A. Fleck, L.J. Gibson, J.W. Hutchinson and H.N.G. Wadley Metal Foams: A Design Guide, 2000

[83] Weinrich, H.; Gehring, M.; Tempel, H.; Kungl, H.; Eichel, R.-A. Impact of the charging conditions on the discharge performance of rechargeable iron-anodes for alkaline iron-air batteries. J. Appl. Electrochem. 2018, 48, 451–462.

[84] Sundar Rajan, A.; Ravikumar, M.K.; Priolkar, K.R.; Sampath, S.; Shukla, A.K. Carbonyl-Iron Electrodes for Rechargeable-Iron Batteries. Electrochem. Energy Technol. 2014, 1, 2–9.

[85] Posada, J.O.G.; Hall, P.J. Controlling hydrogen evolution on iron electrodes. Int. J. Hydrogen Energy 2016, 41, 20807–20817

[86] Long, N.V., Yang, Y., Thi, C.M., Hang B.T., Cao, Y., Nogami, M., Controlled synthesis and characterization of iron oxide micro-particles for Fe-air battery electrode material, 2015, Colloid and Polymer Science 293(1), pp. 49-63

[87] Weinrich, H., Pleie, J., Schmid, B., (...), Kungl, H., Eichel, R.-A., In Situ Hydrogen Evolution Monitoring During the Electrochemical Formation and Cycling of Pressed-Plate Carbonyl Iron Electrodes in Alkaline Electrolyte, 2022, Batteries and Supercaps 5(5),e202100415

[88] Figueredo Rodriguez,H.A.;Mckerracher, R.D.; PonceDe León,C.;Walsh, F.C. Improvement of Negative Electrodes for Iron-Air Batteries: Comparison of Different Iron Compounds as Active Materials. J. Electrochem. Soc. 2019, 166, A107–A117.

[89] Hang, B.T.; Hayashi, H.; Yoon, S.-H.; Okada, S.; Yamaki, J. Fe2O3-filled carbon nanotubes as a negative electrode for an Fe-air battery. J. Power Sour. 2008, 178, 393–401.

[90] Hang, B.T.; Thang, D.H.; Kobayashi, E. Fe/carbon nanofiber composite materials for Fe-air battery anodes. J. Electroanal. Chem. 2013, 704, 145–152

[91] Bui, H.T., Vu, T.M., Hydrothermal Preparation of Fe2O3 Nanoparticles for Fe-Air Battery Anodes, 2019, Journal of Electronic Materials 48(11), pp. 7123-7130

[92] Cohn, G.; Ein-Eli, Y. Study and development of non-aqueous silicon-air battery. J. Power Sour. 2010, 195, 4963–4970

[93] Wang, H.; Liang, Y.; Gong, M.; Li, Y.; Chang, W.; Me_ord, T.; Zhou, J.; Wang, J.; Regier, T.; Wei, F.; et al. An ultrafast nickel-iron battery from strongly coupled inorganic nanoparticle/nanocarbon hybrid materials. Nat. Commun. 2012, 3, 917

[94] Li, X., Xiao D., Modification of corroded metal (Ni or Fe) foam for high performance rechargeable alkaline Ni/Fe batteries, 2020, ChemElectroChem 10.1002/celc.202000809

[95] Nikamoto, T., Sasaki, H., Microstructure-dependent corrosion and passivation of iron with a high carbon content in weak alkaline solution, 2021, Construction and Building Materials 269,121297

[96] Yilmaz, A. (2021). The effect of microstructure on micro- and macro-scale corrosion and passivation behaviour of low-alloyed ferrous materials. https://doi.org/10.4233/uuid:ab648631-4b9a-4c4b-add6- 5696b3cf0165

[97] Aremu E. O., Ryu K-S., Performance and degradation behavior of carbonyl Fe – MoS2 composite as anode material in Fe-air batteries, 2019, Electrochimica Acta Volume 313, Pages 468-477

[98] H. Weinrich, Renaissance der Eisen-Luft-Batterie, Forschungszentrum Jülich, 2017, https://www.fz-juelich.de/de/aktuelles/news/fachmeldungen/2017/2017-11-3-eisen-luft-batterie

[99] A. Zablocki, Fact Sheet Energy Storage https://www.eesi.org/papers/view/energy-storage-2019, 2019

[100] Yang, Chi-Jen (11 April 2016). Pumped Hydroelectric Storage. Duke University. ISBN 9780128034491.

[101] “What is a flow battery?”, https://flowbatteryforum.com/what-is-a-flow-battery/, IFBF 2022

[102] Fuel Cells Hydrogen and Fuel Cell Technologies Office, https://www.energy.gov/eere/fuelcells/fuelcells#:~:text=A%20fuel%2C%20such%20as%20hydrogen,creating%20a%20flow%20of%20electricity.

[103] The Electropaedia, battery performance characteristics, https://www.mpoweruk.com/performance.htm, 2005

[104] Quantumscape, Distinguishing charge rates for next generation batteries, https://www.quantumscape.com/resources/blog/distinguishing-charge-rates-for-next-generation-batteries/#:~:text=What%20is%20a%20C%2Drate,%2D100%25%20in%20one%20hour, 2021

[105] Honsberg C., Bowden S., Battery capacity, https://www.pveducation.org/pvcdrom/battery-characteristics/battery-capacity

[106] Y. bing Guo, C. Li, Y. chang Liu, L. ming Yu, Z. qing Ma, C. xi Liu, and H. jun Li, Effect of microstructure variation on the corrosion behavior of high-strength low-alloy steel in 3.5wt% NaCl solution, International Journal of Minerals, Metallurgy and Materials 22, 604, 2015

[107] Y. Takabatake, K. Fushimi, T. Nakanishi, and Y. Hasegawa, Grain-dependent passivation of iron in sulfuric acid solution, Journal of the Electrochemical Society 161, C594, 2014

[108] Garche, Jurgen; Dyer, Chris K.; Moseley, Patrick T.; Ogumi, Zempachi; Rand, David A. J.; Scrosati, Bruno (2013). Encyclopedia of Electrochemical Power Sources. Newnes. p. 407. ISBN 978-0-444-52745-5.

[109] Vijayamohanan, K.; Shukia, A.K.; Sathyanarayana, S. Role of sulphide additives on the performance of alkaline iron electrodes. J. Electroanal. Chem. Interfacial Electrochem. 1990, 289, 55–68

[110] Jain, D., reactivity series of metals, https://www.toppr.com/bytes/reactivity-series-of-metals/, 2018

[111] Shi, Wn., Yang, Sf. & Li, Js. Effect of nonmetallic inclusions on localized corrosion of spring steel. Int J Miner Metall Mater 28, 390–397 (2021)

[112] K. Fushimi, R. Nakagawa, Y. Kitagawa, and Y. Hasegawa, Micro- And nanoscopic aspects of passive surface on pearlite structure of carbon steel in pH 8.4 boric acid-borate buffer, Journal of the Electrochemical Society 166, C3409 (2019)

[113] Effect of Annealing on Microstructure and Corrosion Behavior of Interstitial Free Steel He, Q.; Jiang, X.; Cai, P.; Zhang, L.; Sun, T.; Yang, X.; Zhou, K.; Zhang, L. Effect of Annealing on Microstructure and Corrosion Behavior of Interstitial Free Steel. Materials 2022, 15, 24. https://doi.org/10.3390/ma15010024

[114] Lyon, Stuart. (2010). Corrosion of Carbon and Low Alloy Steels. Shreir's Corrosion. 3. 1693-1736. 10.1016/B978-044452787-5.00190-6

[115] Rodionova, I.G., Feoktistova, M.V., Baklanova, O.N. et al. Effect of Chemical Composition and Microstructure Parameters on Carbon and Low-Alloy Steel Corrosion Resistance. Metallurgist 61, 770–776 (2018). https://doi org.tudelft.idm.oclc.org/10.1007/s11015-018-0562-9

[116] Samusawa, I., Izumi, D., Shimamura, J., Influence of dislocation on sour corrosion of carbon steel in a low H2S sour environment, 2021

[117] Jacoby, M. It's time to get serious about recycling lithium-ion batteries, 2019, https://cen-acs-org.tudelft.idm.oclc.org/materials/energy-storage/time-serious-recycling-lithium/97/i28

[118] "tem5psu", Pourbaix diagram for water, including equilibrium regions for water, oxygen and hydrogen, 2017, https://commons.wikimedia.org/wiki/File:H2OPourbaix.png

[119] L. R. Bhagavathi, G.P. Chaudhari , S.K. Nath, Mechanical and corrosion behavior of plain low carbon dual-phase steels, Materials and Design, 2010

[120] A. Schreiber, J. W. Schultze, M. M. Lohrengel, F. Kármán, and E. Kálmán, Grain dependent electrochemical investigations on pure iron in acetate buffer pH 6.0, Electrochimica Acta 51, 2625 (2006).

[121] K. Fushimi, K. Yanagisawa, T. Nakanishi, Y. Hasegawa, T. Kawano, and M. Kimura, Microelectrochemistry of dual-phase steel corroding in 0.1 M sulphuric acid, Electrochimica Acta 114, 83 (2013).

[122] Y. Kayali and B. Anaturk, Investigation of electrochemical corrosion behavior in a 3.5wt.% NaCl solution of boronized dual-phase steel, Materials and Design 46, 776 (2013).

[123] R. Nadlene, H. Esah, S. Norliana, and M. A. Mohd Irwan, Study on the effect of volume fraction of dual phase steel to corrosion behaviour and hardness, World Academy of Science, Engineering and Technology 50, 564 (2011).

[124] D.P. Field, P.B. Trivedi and S.I. Wright (2005) "Analysis of local orientation gradients in deformed single crystals" Ultramicroscopy 103: 33-39.

[125] McCafferty, Introduction to corrosion science, springer, 2010

[126] I. Stojanovic,, V. Šimunovic, V. Alar and F. Kapor 2 Experimental Evaluation of Polyester and Epoxy– Polyester Powder Coatings in Aggressive Media, 2018

[127] H., Courtney, Thomas (2005). Mechanical behavior of materials. Waveland Press. ISBN 978-1577664253. OCLC 894800884.

[128] Nye, J.F (March 1953). "Some geometrical relations in dislocated crystals". Acta Metallurgica. 1 (2): 153–162. doi:10.1016/0001-6160(53)90054-6. ISSN 0001-6160.

[129] Xin Xue, António B. Pereira ,José Amorim 2 andJuan Liao , Effects of Pulsed Nd:YAG Laser Welding Parameters on Penetration and Microstructure Characterization of a DP1000 Steel Butt Joint, 2017

[130] A. Kennedy; Manufacturing Division, University of Nottingham, Nottingham, UK; Porous Metals and Metal Foams Made from Powders, 2012

[131] https://www.dorsetware.com/how-is-tin-plating-used-and-what-are-the-benefits/#:~:text=In%20tin%20electroplating%2C%20the%20object,a%20thin%20coating%20of%20tin.

[132] X. Chang , J. Wang, H. Shao, J. Wang , X. Zeng , J. Zhang, C. Cao; Corrosion and Anodic Behaviors of Pure Aluminum in a Novel Alkaline Electrolyte (2008)

[133] J. Wang, H. Shao, J. Wang , X. Zeng , J. Zhang, C. Cao; The effects of surface treatment and stannate as an electrolyte additive on the corrosion and electrochemical performances of pure aluminum in an alkaline methanol–water solution

[134] Ralston, K. D., & Birbilis, N. (2010). Effect of Grain Size on Corrosion: A Review. CORROSION, 66(7), 075005–075005–13. doi:10.5006/1.3462912

[135] K.D. Ralston, N. Birbilis, C.H.J. Davies, Revealing the relationship between grain size and corrosion rate of metals, Scripta Materialia 63 (2010) 1201-1204

[136] M. Soleimani et al 2019 Effect of grain size on the corrosion resistance of low carbon steel Mater. Res. Express in press https://doi.org/10.1088/2053-1591/ab62fa

[137] A Practical Beginner's Guide to Cyclic Voltammetry; Noémie Elgrishi, Kelley J. Rountree, Brian D. McCarthy, Eric S. Rountree, Thomas T. Eisenhart, and Jillian L. Dempsey* Department of Chemistry, University of North Carolina

[138] Cyclic Voltammetry Applications and Uses, Dr. Chris Bracher, Software Engineer, Harry Robson, PhD Student Collaborator

[139] The Iron Oxides; Structure, Properties, Reactions, Occurences and Uses; R.M. Cornell, U. Schwertmann, Second, Completely Revised and Extended Edition

[140] Electrochemical Methods, Fundamentals and Applications. Allen J. Bard, Larry R. Faulkner. Department of Chemistry and Biochemistry, University of Texas at Austin.

[141] N. M. Markovića, S. T. Sarraf, H. A. Gasteiger, and P. N. Ross, *Hydrogen electrochemistry on platinum low-index single-crystal surfaces in alkaline solution,* J. Chem. Soc., Faraday Trans. **92**, 3719 (1996).

[142] J. Perez, E. R. Gonzalez, and H. M. Villullas, *Hydrogen evolution reaction on gold single-crystal electrodes in acid solutions,* The Journal of Physical Chemistry B **102**, 10931 (1998).

[143] A. R. Zeradjanin, J.-P. Grote, G. Polymeros, and K. J. J. Mayrhofer, *A critical reviewon hydrogen evolution electrocatalysis: Re-exploring the volcano-relationship,*Electroanalysis **28**, 2256 (2016).

[144] K-M. Park, K-S Min, Y-S. Roh; Design Optimization of Lattice Structures under Compression: Study of Unit Cell Types and Cell Arrangements, 2022

A. ImageJ

ImageJ is an image processing program which can (among other things) distinguish optical differences in colour intensities. This feature makes it ideal to perform analysis of certain results acquired. In the current report, the software is applied to determine the phase fractions of martensite and ferrite of the DP1000 steel and identify the crystallographic orientation differences for the hot-rolled and cold-rolled samples.

For the EBSD images, the obtained IPF Figure is opened in ImageJ. Then, the option split channels is chosen to separate red, green and blue colours from the IPF. Three channels are now made for these colours and provided in black and white shades. White having a high colour code of “255” while (completely) black is signified by “0”.

Next the threshold of 250-255 is selected to obtain the fraction of a particular orientation in the IPF Figure. In Figure 64 below, the crystallographic orientation corresponding to <111> // ND (blue in the IPF) is marked red. The total area coverage fraction is given in the panel on the right. The same threshold range is applied each time.

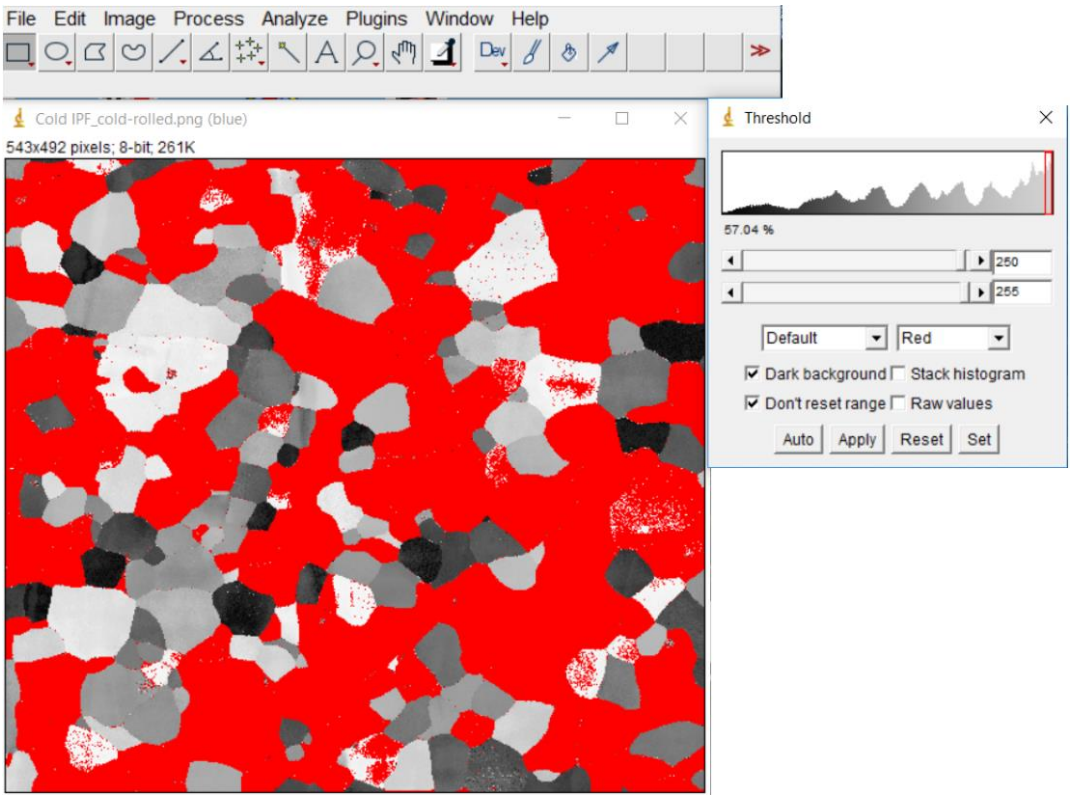

Fig. 64 ImageJ screenshot of the relative area fraction of crystal orientations.

The dual phase steel is identified in a similar manner. Given the already grey shades of the SEM image, simply a threshold is applied to distinguish light grey from dark grey and black regions. In Figure 65 below the more dark regions are marked by the colour red, which indicates ferrite phase.

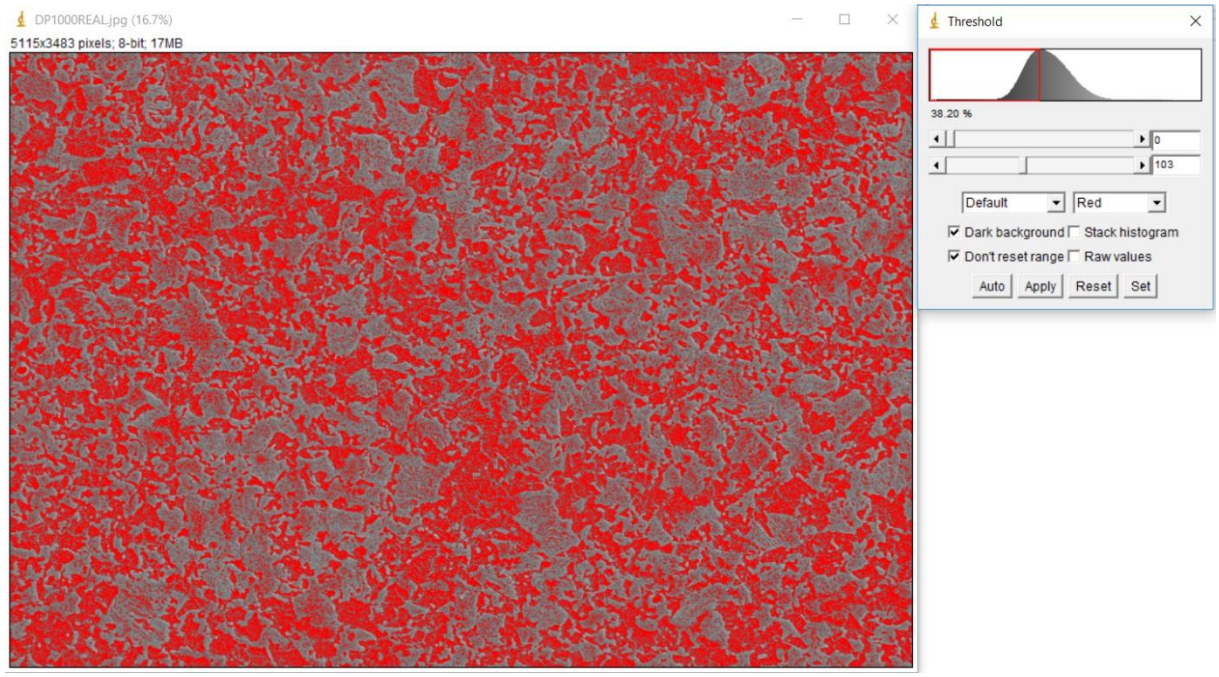

Fig. 65 ImageJ screenshot of the phase fraction determination of DP1000.